TECHNISCHE UNIVERSITÄT MÜNCHEN
Lehrstuhl für Steuerungs- und Regelungstechnik

A Universal MR-Compatible Haptic Interface for Motor Neuroscience

Markus Kühne

Vollständiger Abdruck der von der Fakultät für Elektrotechnik und Informationstechnik der Technischen Universität München zur Erlangung des akademischen Grades eines

Doktor-Ingenieurs (Dr.-Ing.)

genehmigten Dissertation.

Vorsitzender: Prof. Dr.-Ing. Klaus Diepold

Prüfer der Dissertation:

1. Prof. Dr.-Ing. Angelika Peer
   University of the West of England, Bristol, UK
2. Prof. Dr. Jörg Conradt

Die Dissertation wurde am 04.09.2017 bei der Technischen Universität München eingereicht und durch die Fakultät für Elektrotechnik und Informationstechnik am 30.04.2018 angenommen.

Foreword

This thesis summarizes three and a half years of research at the Technische Universität München (TUM). It started at the Chair of Automatic Control Engineering (LSR) and was completed at the Biomimetic Robotics and Machine Learning Laboratory (BRML) together with the University of the West of England (UWE). The work was supported by the German Research Foundation (DFG) within the project “VR system for visuo-haptic stimulation in the context of fMRI analyses".

First of all, I would like to express my sincere gratitude to my advisor Prof. Angelika Peer. Throughout the project, she supported this work via in-depth discussions, swift and detail-oriented feedback, and by giving me the freedom to explore scientific ideas. Moreover, the project underwent a series of administrative changes and together we were able to find solutions to even the most difficult challenges.

Moreover, I would like to thank Prof. Patrick van der Smagt. Over the course of the project, I also became a member of his research group, the Biomimetic Robotics and Machine Learning Labortatory. I am very grateful for the enriching and versatile environment, as well as the input and feedback I received.

The project involved many experiments at the site of our project partner, the Max-Planck Institute for Biological Cybernetics in Tübingen. The experiments were usually very labor-intensive and I would like to thank Ali Aghaeifar and Martin Eschelbach for their support and for making the stays so enjoyable. Moreover, I would like to thank Dr. Axel Thielscher, Dr. Marc Himmelbach, and Prof. Klaus Scheffler, who helped preparing and evaluating the studies we carried out.

A great thanks goes to all my colleagues at TUM at the Chair for Automatic Control Engineering (LSR) and the Chair for Robotics and Embedded Systems (I6), with whom I had many interesting discussions and who made the three and a half years of research so exciting.

The work presented here involved realizing many prototypes and I would like to thank Mr. Jaschik, Mr. Lowitz, Mr. Weilbach, and most of all Mr. Stoeber from the LSR for their help and advice. Moreover, I would like to thank Theodor Steffen from the Max-Planck Institute for Biological Cybernectics for the enjoyable joint work on the final prototype. Without the experience and knowledge of all these people, the hardware would have not been realized at the quality and pace as it did.

I also had the pleasure of supervising and working with many students. I especially would like to thank Roberto García-Rochín, Johannes Potzy, Wolfgang Wiedmeyer, and Lisa von Pflugk for their contributions.

Last and most of all, I would like to thank my family and friends for their support throughout the years.

Munich, August 2017 Markus Kühne

This is robot science.

Abstract

Functional magnetic resonance imaging is a powerful tool in neuroscience. It allows visualizing active areas in the human brain and thus, gives researchers insight into cerebral mechanisms. This advances brain research and the understanding of neural disorders such as stroke. Especially, using this method to investigate human motor control mechanisms is an active, yet challenging field of research. In order to analyze these mechanisms, subjects have to perform movements under standardized experimental conditions inside a magnetic resonance scanner. These conditions can be generated with a haptic interface, i.e. a robotic system that creates a sense of touch by applying haptic feedback to a human operator.

But until now, haptic interfaces for functional magnetic resonance imaging have been mostly built around specific research questions. Almost no general device exists that allows us to target a series of these research questions by just reprogramming rather than redesigning. One reason is that the magnetic field poses a variety of challenges to the construction of robotic systems that must be placed in magnetic resonance environments: Ferromagnetic components and floating actuators lead to safety issues and create image artifacts. Hence, the motion capabilities or degrees of freedom of existing haptic interfaces that are compatible with the magnetic field are limited.

In this thesis, a universal magnetic resonance-compatible haptic interface for human motor control studies is presented. The device comprises of a novel kinematics, is based on a novel control method for its actuators, and offers seven degrees of freedom. Thus, subjects can perform translational movements in all Cartesian directions, as well as rotations around three axes, combined with two-finger pinch grasps. Within this work, the device is validated in terms of magnetic resonance-compatibility, ergonomics, and safety. Moreover, a benchmark study for versatile haptic interfaces is proposed and carried out with the device.

The presented haptic interface allows shifting the paradigm from redesigning new devices to reprogramming a single device, when moving on to a new research question. This will relieve neuroscientists from the need of constantly building new devices and should accelerate research on human motor control. Moreover, complex tasks involving natural, unconstrained pick-and-place motions can finally be targeted for investigation. This extends the types of questions in the field of visuomotor control that can be asked by neuroimaging.

Zusammenfassung

Die funktionelle Magnetresonanztomographie ist ein leistungsfähiges Werkzeug der Neurowissenschaften. Sie ermöglicht die Visualisierung aktiver Bereiche im menschlichen Gehirn und gibt Forschern so Einblick in zerebrale Mechanismen. Dies treibt die Hirnforschung voran und fördert das Verständnis von neuronalen Störungen wie dem Schlaganfall. Insbesondere die Untersuchung der menschlichen Bewegungskontrolle ist ein aktives aber auch herausforderndes Forschungsgebiet, welches diese Methode einsetzt. Um diese Mechanismen zu erforschen, müssen Probanden Bewegungen unter standardisierten experimentellen Bedingungen innerhalb eines Magnetresonanztomografen durchführen. Diese Bedingungen können mittels eines haptischen Eingabegerätes erzeugt werden. Dies ist ein Robotersystem, das ein Gefühl der Berührung schafft, indem es ein haptisches Feedback für den menschlichen Bediener erzeugt. In Verbindung mit einer virtuellen Umgebung können so standardisierte Aufgabenszenarien erzeugt werden.

Jedoch wurden haptische Eingabegeräte für die funktionelle Magnetresonanztomographie bisher meistens um spezifische Forschungsfragen herum gebaut. Es gibt fast kein allgemeines Gerät, das es uns erlaubt, eine Reihe dieser Forschungsfragen anzugehen, indem es einfach nur neu programmiert und nicht neu gestaltet wird. Ein Grund dafür ist, dass das Magnetfeld eine Reihe von Herausforderungen für den Bau von Robotersystemen darstellt, die in Magnetresonanz-Umgebungen platziert werden müssen: Ferromagnetische Bauteile und sich im Raum bewegende Aktuatoren führen zu Sicherheitsproblemen und erzeugen Bildartefakte. Daher sind die Bewegungsfähigkeiten oder auch -freiheitsgrade der vorhandenen haptischen Eingabegeräte, welche kompatibel mit dem magnetischen Feld sind, begrenzt.

In dieser Arbeit wird ein universelles magnetresonanz-kompatibles haptisches Eingabegerät für Studien der menschlichen Bewegungskontrolle vorgestellt. Das Gerät verfügt über eine neuartige Kinematik, basiert auf einer neuen Regelungsmethode für seine Aktuatoren und besitzt sieben Bewegungsfreiheitsgrade. So können Probanden translatorische Bewegungen in allen kartesischen Richtungen durchführen, sowie Rotationen um drei Achsen kombiniert mit Zwei-Finger-Präzisionsgriffen. In dieser Arbeit werden die Kompatibilität des Gerätes mit dem magnetischen Feld, seine Ergonomie als auch seine Sicherheit evaluiert. Darüber hinaus wird eine Vergleichs-Studie für vielseitige haptische Interfaces entworfen und mit dem Gerät durchgeführt.

Das vorgestellte haptische Eingabegerät ermöglicht eine Verschiebung des Paradigmas, weg vom Design immer neuer Geräte hin zur Neuprogrammierung eines einzelnen Gerätes, wenn eine neue Forschungsfrage beantwortet werden soll. Dies wird Neurowissenschaftler von der Notwendigkeit befreien, immer neue Geräte zu bauen und soll so die Forschung im Bereich der menschlichen Bewegungsplanung beschleunigen. Darüber hinaus können endlich komplexe Aufgaben, die natürliche, uneingeschränkte Pick-and-Place-Bewegungen beinhalten, erforscht werden. Dies erweitert die Arten von Fragen, welche, im Bereich der visuell-motorischen Bewegungskontrolle, durch bildgebende Verfahren gestellt werden können.

Contents

1 Introduction 1
1.1 Motivation and state of the art . . . 1
1.2 Problem statement and challenges . . . 5
1.3 Thesis outline and contributions . . . 7

2 Modeling and two-input Sliding Mode Control of Ultrasonic Motors 9
2.1 Problem statement and approach . . . 9
2.2 Dynamic model . . . 11
  2.2.1 Simplification of the dynamic model by Canudas-de-Wit . . . 12
  2.2.2 Extension of the dynamic model by Canudas-de-Wit . . . 12
2.3 Two-input sliding mode controller . . . 13
  2.3.1 Control laws . . . 14
  2.3.2 First order sliding mode . . . 15
2.4 Stability analysis . . . 15
  2.4.1 Reachability condition . . . 15
  2.4.2 Equilibrium set and steady state error . . . 16
  2.4.3 Smooth switching of the variable structure system . . . 17
2.5 Experimental identification of the dynamic model . . . 18
  2.5.1 Experimental procedures . . . 18
  2.5.2 Methods for model parameter identification . . . 19
  2.5.3 Model identification results . . . 20
2.6 Controller validation in simulation and experiments . . . 21
2.7 Conclusion . . . 27

3 Design and Evaluation of an Octopod Kinematics 29
3.1 Problem statement and approach . . . 29
3.2 Design criteria and procedure, and performance indices . . . 30
  3.2.1 Design criteria . . . 30
  3.2.2 Adopted procedure for kinematic selection and design optimization . . . 31
  3.2.3 Performance indices . . . 32
3.3 Kinematics selection and design optimization . . . 37
  3.3.1 Step 1: Selection of fully-parallel kinematics with rotary actuators . . . 37
  3.3.2 Step 2: Determination of an optimal kinematics . . . 37
  3.3.3 Step 3: Redundant extension of the optimal kinematics . . . 43
  3.3.4 Step 4: Hardware realization of the Octo kinematics . . . 45
3.4 Discussion . . . 49

3.5 Conclusion 49

4 An MR-compatible Haptic Interface with Seven Degrees of Freedom for fMRI Studies 51
4.1 Problem statement and approach 51
4.2 Design requirements 52
4.3 Design of an MR-compatible haptic interface 53
4.3.1 Octopod 53
4.3.2 Haptic gripper 55
4.3.3 Support frame 55
4.4 Visual and haptic rendering 56
4.4.1 Hardware and software setup 56
4.4.2 Virtual environment 57
4.4.3 Control of the haptic interface 57
4.5 Human factors analysis 59
4.5.1 Methods for human factors analysis 59
4.5.2 Results 59
4.6 Experimental validation 63
4.6.1 Performance indices 63
4.6.2 Results 64
4.7 MR-compatibility validation 66
4.7.1 Validation methods 66
4.7.2 Results 67
4.8 Discussion 69
4.9 Conclusion 70

5 Towards a Benchmark fMRI Study for Versatile Haptic Interfaces 71
5.1 Introduction 71
5.2 Study hypotheses 73
5.3 Experimental Setup 73
5.3.1 Benchmark grasp and lift scenario 74
5.3.2 Haptic interface MR-Octo 75
5.4 Study design and experimental procedure 77
5.5 Results 78
5.5.1 MRI preprocessing and analysis 78
5.5.2 Behavioral data 79
5.5.3 fMRI analysis 81
5.6 Discussion 82
5.7 Conclusion 83

6 Conclusions and Future Directions 87
6.1 Concluding remarks 87
6.2 Outlook 88

Notations

Abbreviations

BOLD	blood-oxygen-level dependent
CAD	computer aided design
CMA	cingulate motor areas
DC	direct current
DoF	degrees of freedom
EPI	echo-planar image
FDA	food and drug administration
FG	frontal gyrus
FK	forward kinematics
FOV	field of view
fMRI	functional magnetic resonance imaging
GII	global isotropy index
G&L	grasp-and-lift
GLM	general linear model
GRE	gradient echo
GUAS	global uniform asymptotic stability
LCA	linear complex approximation
HFE	human factors engineering
ICA	independent component analysis
IPC	inferior parietal cortex
IPS	intraparietal sulcus
IK	inverse kinematics
M1	primary motor cortex
MNI	Montreal Neurological Institute
PC	polycarbonate
MR	magnetic resonance
PMd	dorsal premotor cortex
PMv	ventral premotor cortex
PVC	polyvinyl chloride
RF	radio frequency
RMS	root mean square
S1	primary somatosensory cortex
S2	primary somatosensory cortex
SMA	supplementary motor area
SMC	sliding mode control
SPM	statistical parametric mapping

TE	time of echo
TR	time of repetition
UE	usability engineering
USM	ultrasonic motor

Conventions

Scalars, Vectors, and Matrices

Scalars are denoted by lower case letters in italic type. *Vectors* are denoted by bold lower case letters in italic type, as the vector $\mathbf{x}$ is composed of elements x_i. *Matrices* are denoted by bold upper case letters, as the matrix $\mathbf{K}$ is composed of elements k_{ij} (i^{th} row, j^{th} column).

x or X	scalar
$\mathbf{x}$	vector
$\mathbf{X}$	matrix
$\mathbf{X}^T$	transposed of X
$\mathbf{X}^{-1}$	inverse of X
$f(\cdot)$	scalar function
$\mathbf{f}(\cdot)$	vector function
$\dot{x}, \ddot{x}, \ldots$	first, second, … time derivative of x

Kinematic chains

Kinematic chains are described as a series of joint-types in one leg, starting from the base. A leg can consist of rotary (R), universal (U), spherical (S), and prismatic (P) joints. An actuated joint is underlined. An initial digit indicates the number of legs that are part of a parallel kinematics. Example: 6-$\underline{\text{R}}$US describes a parallel kinematics with six legs and the first rotary joint of each leg is actuated.

R	rotary joint
U	universal joint
S	spherical joint
P	prismatic joint

Symbols

General

t	time
$\mathbf{F}$	measured end effector wrench
$\mathbf{F}_{vr}$	virtual reaction force and torque
L	number of legs
d	number of DoF
i	actuator index
j	DoF index
m_{OC}	mass of the end effector
$I_{x,y,z}$	inertia around the main axes of the end effector
$\mathbf{J}_q$	Jacobian matrix
$\mathbf{J}_x$	Jacobian matrix
$\mathbf{J}$	Jacobian matrix
$\mathbf{J}^{\#}$	pseudo-inverse of the Jacobian matrix
$\hat{\mathbf{J}}$	generalized Jacobian matrix
$\hat{\mathbf{J}}_{trans}$	translational subcomponent of the generalized Jacobian matrix
$\hat{\mathbf{J}}_{rot}$	rotational subcomponent of the generalized Jacobian matrix
$\hat{\mathbf{j}}_i$	ith column of the Jacobian $\hat{\mathbf{J}}$
$\mathbf{q}$	actuator positions
$\mathbf{q}_d$	desired actuator positions
σ	singular value
$\mathbf{M}_q(\mathbf{q})$	mass matrix in joint space
$\hat{\mathbf{M}}$	mass matrix in Cartesian space
l_0	base radius
l_1	length of first link in each leg of the kinematics
l_2	length of second link in each leg of the kinematics
l_3	length of third link in each leg of the kinematics
l_p	end effector radius
l_d	distance between two neighboring actuators on the base platform
β	orientation of first link
γ	orientation of third link
$\tau_{i,max,n}$	maximum nominal motor torque
$\tau_{i,max,s}$	maximum stall motor torque
$v_{i,max}$	maximum nominal velocity
B_0	static magnetic field of the MR scanner

Chapter 1-specific

V_0	voltage actuating the piezo-ceramics
F_{ax}	axial force
F_C	Coulomb friction
F_S	Stribeck friction
τ_{dr}	driving torque

τ_{op}	opposing torque
τ_m	motor torque
τ_b	brake torque
J_r	rotor inertia
C_r	friction coefficient
r_0	mean radius of rotor/stator contact area
ξ	friction state
$\sigma_{0,1}$	micro-damping friction coefficients
θ_r	rotor position
ω_{st}	stator velocity
ω_0	Stribeck velocity
ω_n	resonant frequency of the piezoelectric material
ω_i	ideal stator velocity
f	frequency of the traveling wave
α	phase difference
$R(f, \omega_n)$	non-linear dependence on f and ω_n
$g(\omega_{st} - \dot{\theta}_r)$	non-linear function summarizing Coulomb and Stribeck friction effects
$\mathrm{sgn}(\cdot)$	signum function
$\alpha_{dz}(\tau_{op})$	dead zone width depending on opposing torque
$\delta(f, \alpha, \tau_{op})$	non-linear disturbance
μ	control parameter determining the control domain
S	ideal sliding surface
$\tilde{S}$	sliding surface under disturbance
m	slope of a linear sliding surface
$z(\tau_{op})$	velocity drop due to opposing torque
r_{ref}	reference position
$p(\dot{\theta}_r, \tau_{op}, t)$	perturbation
M_l	perturbation upper bound
Ω	equilibrium set
$\mathbf{n}(\mathbf{x})$	normal vector
$\dot{x}_1$	velocity error
$\dot{x}_2$	acceleration error
Δx	steady state position error
$\mathbf{f}(\mathbf{x})$	state vector

Chapter 2-specific

K_P	proportional controller gain
K_I	integral controller gain
K_D	differential controller gain
$\mathbf{p}$	vector of actuator output capabilities
$\overline{p}_i$	maximum actuator output capability
$\mathbf{u}$	end effector output capability
$\mathscr{S}$	generalized set
$\mathrm{Conv}(\mathscr{S})$	convex hull

α_j	scaling factor
$\mathbf{c}$	point on the convex hull
$\mathbf{x}$	end effector pose
$\mathbf{x}_d$	desired end effector pose
$\mathbf{f}$	end effector wrench
$\mathbf{x}_0$	origin of the coordinate system
f_{min}	minimum force
$\dot{x}_{min}$	minimum velocity
$\ddot{x}_{min}$	minimum acceleration
$\mathbf{x}$	end effector pose
$\mathbf{x}_d$	desired end effector pose

Chapter 3-specific

F_{safety}	safety margin
F_{grip}	grip force
$F_{gripper}$	gripper force
m_{glass}	weight of CAD glass model
I_{glass}	maximum inertia of CAD glass model
a_{trans}	maximum translational acceleration
a_{rot}	maximum angular acceleration
F_{max}	maximum force
τ_{max}	maximum torque
μ_{glass}	friction coefficient between human hand and glass
s	grip force slope
χ_v	magnetic volume susceptibility
$V_{i,freq}$	voltage that determines the frequency of the traveling wave at the actuator
$V_{i,phase}$	voltage that determines the phase difference of the traveling wave at the actuator
$\mathbf{M}$	mass matrix for rendered admittance
m_j	mass component for rendered admittance
$\mathbf{D}$	damper matrix for rendered admittance
d_j	damper component for rendered admittance
$K(\cdot)$	function of gripper stiffness
$\mathbf{x}$	end effector pose
$\mathbf{x}_d$	desired end effector pose

List of Figures

1.1 Virtual reality (left) and haptic interface (right). 1
1.2 State of the art of MR-compatible haptic interfaces ordered by the realizable DoF: Devices with **one DoF** [11] IEEE 2015, [6] IEEE 2015, [22] IEEE 2007, [5] IEEE 2005; **two DoF** [14] IEEE 2006, [12] (Reproduced with permission from the Society for Neuroscience), [18] IEEE 2015; **three DoF** [19], [20]; and **five DoF** [21] [IEEE 2017]. 3
1.3 Schematic velocity behavior of a USM: The velocity $\dot{x}$ depends on the control input u and low velocities cannot be realized. Moreover, dead zones are generated and their width w grows with increasing load. 5
1.4 Example of a parallel kinematics with six legs in a direct kinematic singularity, where an uncontrollable DoF is gained around the dashed black axis is gained. 6

2.1 Free body diagram of a USM, in this case a Shinsei USR60. 11
2.2 Dead zone caused by an opposing torque in the phase difference domain. . . . 13
2.3 Control scheme of the two-input SMC. 15
2.4 Scheme of the signal flow between workstation and testbed. 19
2.5 Photograph of the testbed with (1) Encoder, (2) USM, (3) torque sensor, and (4) magnetic brake. 19
2.6 Photograph of the original (left) and modified (right) motor driver. 20
2.7 USM velocity depending on phase difference and frequency at minimum load. 21
2.8 Interpolated USM velocity, depending on phase difference, frequency and torque. 22
2.9 Modeled velocity depending on phase difference and frequency at minimum load. 23
2.10 Modeled USM velocity, depending on phase difference, frequency, and torque of the model. 24
2.11 Phase portrait of controlled systems in experiment and in simulation after a 1 rad position step input. 24
2.12 Velocity error x_2 over time on the proposed velocity source model after a 1 rad position step input. The phase difference control domains in case of minimum and maximum opposing torque τ_{op} start at different time instants. The domains are shown as shaded orange and blue area, respectively. 25
2.13 Phase portrait of controllers on the proposed velocity source model after a 1 rad position step input. 26

3.1 The four steps a)-d) of the ‘polytope algorithm’ with an example in three DoF. 35
3.2 General description of an RSS Hexapod, generalized as an RRRS Hexapod. . . 38

3.3 Results of CuikSuite calculations for Ergin's device, the HEXA, and the Hunt-type kinematics. The dexterous workspace with only translational displacements at zero rotations is depicted in blue and singularities are depicted in green. 39
3.4 Direct kinematic singularities that are present in the workspace of an RSS Hexapod: Hunt's singularity occurs when two terminal links are coplanar with the end effector and an uncontrollable DoF around the LCA is present. In Fichter's singularity, the end effector describes an uncontrollable screw motion along the z_p axis that aligns with the LCA. 40
3.5 Dexterous workspace, depicted with only translational displacements of the Octopod kinematics in blue and desired workspace volume, where ±20° rotations around all axes are achievable, in red. 42
3.6 Worst-case output capabilities of the Octopod kinematics at $z = 0.30\ m$ with rotations of ±30° around all axes. 43
3.7 Plot of a force polytope that was computed for the evaluation of the Octopod kinematics. The continuous force is represented by a grey sphere that is tangential to one of the surfaces of the polytope. 44
3.8 Photograph of the realized Octo. 46
3.9 Hardware setup and signal flow between the Octo and the workstation. 48

4.1 Octopod kinematics providing six DoF (left) and Octopod kinematics augmented with schematic haptic gripper, driven by Bowden cables (right). 54
4.2 MR-Octo (1) for right-handed operation with haptic gripper (2), mounted on a support frame (3) that also carries an MRI pillow (4), supporting the subject's legs. 55
4.3 Signal flow between the mobile control station on wheels in the control room (left) and the scanning room (right). All signals are filtered as they pass from one room to the other. 56
4.4 Chai3D example: Three cubes can be manipulated. 57
4.5 Admittance control scheme that determines the interaction of haptic interface (H) with virtual environment and human operator. Forward kinematics (FK) and inverse kinematics (IK) transform between Cartesian and joint space. A low-level position controller sets desired actuator positions. 58
4.6 Gripper principle, where approximated Bowden cable stiffness K, USM position q_9, and gripper orientation x_7 generate a grasp force $F_{gripper}$. Grasping an object also leads to a virtual reaction force $F_{vr,7}$, which is not depicted. 58
4.7 Main user interfaces of the MR-Octo for scientists (left) and subjects (right). . 61
4.8 Protection that separates user legs from robot legs (left) and secure clamping of cables (right). 61
4.9 Guided training of the subject (left) and adjustment of the position of the haptic interface to reach an ergonomic position (right). 63
4.10 Photographs of the MR-Octo from front (left) and back (right). The backside can be closed entirely by the chassis, which is not depicted. 64

4.11 Reachable workspace with only translational displacements of the Octopod kinematics, depicted in blue and dexterous workspace volumes, where ±30° and ±20° rotations around all axes are achievable shown in green and magenta, respectively. 65
4.12 Setup for MR-compatibility test of force/torque sensor. 67
4.13 Setup for MR-compatibility test of the MR-Octo. 68
4.14 The results of the GLM analysis for the device switched off (top) and switched on as well as moving (bottom). The absence of false positives in the background is due to an automatic masking procedure during the analysis. 69

5.1 Experimental setup, shown in a sliced MR scanner: (1) screen that illuminates the scanner bore in red or green, (2) head coil with mounted mirror, (3) subject lying in supine position, (4) benchmark object. 74
5.2 CAD rendering of the benchmark object with (1) force sensor at the top and (2) exchangeable weights that can be pulled off. 74
5.3 Experimental setup, shown in a sliced MR scanner: (1) screen with projected virtual reality, (2) head coil with mounted mirror, (3) subject lying in supine position, (4) haptic interface MR-Octo. 75
5.4 Virtual Environment showing (1) finger tip representations, (2) virtual object, (3) grasp force level bars, (4) rest positions, and (5) weight level indicated by the number of octagonal plates. 76
5.5 Sequence of the grip-and-lift experiment. 77
5.6 Mean of the grip forces with the benchmark object over time for all objects and one subject. 79
5.7 Mean of the grip forces with the haptic interface over time for all objects and one subject. 84
5.8 Mean of the lift forces with the haptic interface over time for all objects and one subject. 84
5.9 Activations related to virtual G&L (red), activations related benchmark G&L (blue), and the overlap of both cases (magenta). 85
5.10 Differences between virtual and real G&L for two cases: Activations of virtual G&L are stronger than of benchmark G&L (red). Activations of virtual G&L are weaker than of benchmark G&L (blue). 85
5.11 Linear modulation of activation with the grip force during virtual G&L: Regions with a higher activation in the case of higher grip force are shown in red, regions with a weaker activation in the case of increasing grip force are shown in blue. 86

List of Tables

1.1 MR-compatible actuation principles, partially adopted from [19]. 4

2.1 Controls laws in the frequency and the phase difference domain. 14
2.2 Characteristic figures of the experimental setup. 18
2.3 Identified model parameters and functions. 21
2.4 Time until a steady state position with $x_2 < 0.01$ rad/s is reached. 27
2.5 Control efforts expressed by the integral of $|\mu|$. 27

3.1 Parameter ranges of l_2, β, γ, and l_d for GII optimization. 39
3.2 Cuboid workspace for GII optimization centered at $z_0 = 0.30$ m. 40
3.3 Minimum and maximum of the worst-case output capabilities as well as maximum sensitivities in the workspace listed in Table 3.2 with rotations of ±20° around all axes. The Octopod kinematics and the realized Octo have additionally been evaluated in the same workspace with rotations up to ±30° around all axes, while maintaining steps of 5°. 41
3.4 GII optimization results. 43
3.5 Experimental and simulative results of minimum worst-case output capabilities of the Octo. 46
3.6 Comparison of the device capabilities to commercial haptic devices. 47

4.1 Parameters of a typical pick-and-place experiment for our device, lifting a light object such as a glass of water. Forces and torques can be derived using Newton's second law of motion, $F = m \cdot a$. 52
4.2 Overview of components, their materials and their magnetic volume susceptibility in SI-units. 54
4.3 Worst-case output capabilities of the MR-Octo in its dexterous workspace. . . . 65
4.4 Worst-case output capabilities of the gripper. 65

1 Introduction

1.1 Motivation and state of the art

Functional Magnetic Resonance Imaging (fMRI) is a powerful tool for fundamental research in neuroscience. It allows visualizing active areas in the human brain and thus, neural mechanisms can be investigated. Moreover, it is applied to improve the understanding of neural disorders, such as stroke [1]. fMRI exploits the possibility that changes in blood flow can be detected via blood-oxygen-level dependent (BOLD) contrast imaging in an MR scanner. Since neural activations and changes in blood flow are coupled, conclusions can be drawn about the location and the kind of information that is being processed. This has made fMRI a popular method to investigate different areas of the human brain. The visual cortex has e.g. been analyzed by showing images or patterns to subjects and observing the correlated activations in the brain [2]. The investigation of other regions, especially related to human motor control, is more involved [3], because subjects need to carry out motor control tasks, such as reaching for an object, inside the MR scanner. These tasks have to be standardized and repeatable in order to render the results comparable across all trials and subjects. Multiple repetitions and subjects are necessary in order to generate statistically significant data. A haptic interface creates the opportunity to introduce these standardized experimental conditions for human motor control studies.

Haptic interfaces are robotic systems that create a sense of touch by applying haptic feedback to a human operator. They provide the ability to not only see but also 'feel' remote or virtual environments. Moreover, the systems allow recording variables such as velocities and forces that are generated by the user. Figure 1.1 depicts a commercial example from Force Dimension[1] that renders forces in three directions. Hence, standardized task scenarios can be generated using these devices.

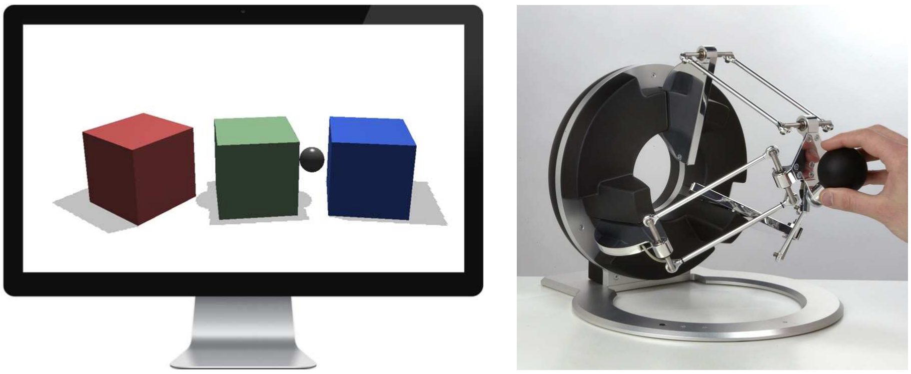

Figure 1.1: Virtual reality (left) and haptic interface (right).

---

[1] forcedimension.com

However, the MR environment poses a series of challenges to actuated devices. The MR scanner constantly generates a static magnetic field and during the imaging process, switching gradients as well as radio frequency (RF) pulses are added, which can disturb sensor and control signals. Moreover, ferromagnetic components and actuators can lead to safety issues and create image artifacts. Thus, any robotic system used during fMRI needs to be bi-directionally MR-compatible[2]. This means that neither the robot is affected by the magnetic field of the scanner nor the imaging process is disturbed. Hence, standard commercial devices, as depicted in Figure 1.1, cannot be employed. Up to now, MR-compatible devices have mostly been built around specific research questions. Consequently, the motion capabilities or Degrees of Freedom (DoF) of existing MR-compatible haptic interfaces are limited. The number of DoF specifies the motions that can be carried out independently from each other. Previous work spans from one up to five actuated DoF and selected developments are depicted in Figure 1.2.

Devices with **one DoF** allow wrist rotations [5, 6], grasp motions with the whole hand [7–9], or simple reaching motions along one axis [10]. Recently, a haptic interface for pinch grasps has been presented [11]. The actuation of the systems is realized via ultrasonic motors (USMs) [5,9], coils [7] or electro-rheological fluids [8] that employ the magnetic field of the MR scanner for actuation. Other possibilities are pneumatic and hydraulic actuators [10] or cable transmissions from a remotely-located direct current (DC) motor [6, 11].

Devices with **two DoF** allow reaching with the whole arm [12–14] or a single finger [15]. Additionally, an MR-compatible joystick with two DoF has been developed [16, 17]. Moreover, an MR-compatible rehabilitation device with three DoF for wrist rotations, called the soft-wrist [18], has been presented. These systems are actuated using pneumatic pistons [12], potential energy [13], hydrostatic transmission [14], USMs [15, 18], or electrostatic motors [16, 17].

The number of haptic interfaces with **three DoF** is smaller and there are only two devices: (a) reaching with one finger can be realized using a device developed in a previous work of our group [19], (b) reaching with the whole arm can be performed by employing a device from the HFI series [20]. The actuation is either based on USMs [19] or remotely-located DC motors that transmit their torques via rods [20].

During the course of this thesis, a device with **five DoF**, called the HFI-5 [21], was developed by Stanford University. It is a combination of two HFI-3.5 haptic interfaces such that rotations around two axes can be performed, in addition to the translational movements.

In summary, there is a broad variety of actuation principles for MR-compatible haptic interfaces. In a previous work of our group [19], the advantages and disadvantages of different options were already discussed and Table 1.1, partly adopted from [19], summarizes the pros and cons of the actuation principles. Early work [10, 12, 14] employed intrinsically MR-compatible actuation technologies such as pneumatic, hydrostatic or hydraulic transmissions. Actuators can be placed outside the scanning room and motion is transmitted to the actuated device via non-magnetic fluids or compressed air. However, pneumatically actuated devices are often hard to control and hydraulic or hydrostatic devices take a long setup time, since all tubes have to be filled with fluids prior to every experiment. More experimental actuation principles include electrostatic motors [16, 17], electroactive polymers, electro-

---

[2] For an exact definition and use of the term *MR-compatible* in this work, the interested reader may refer to [4].

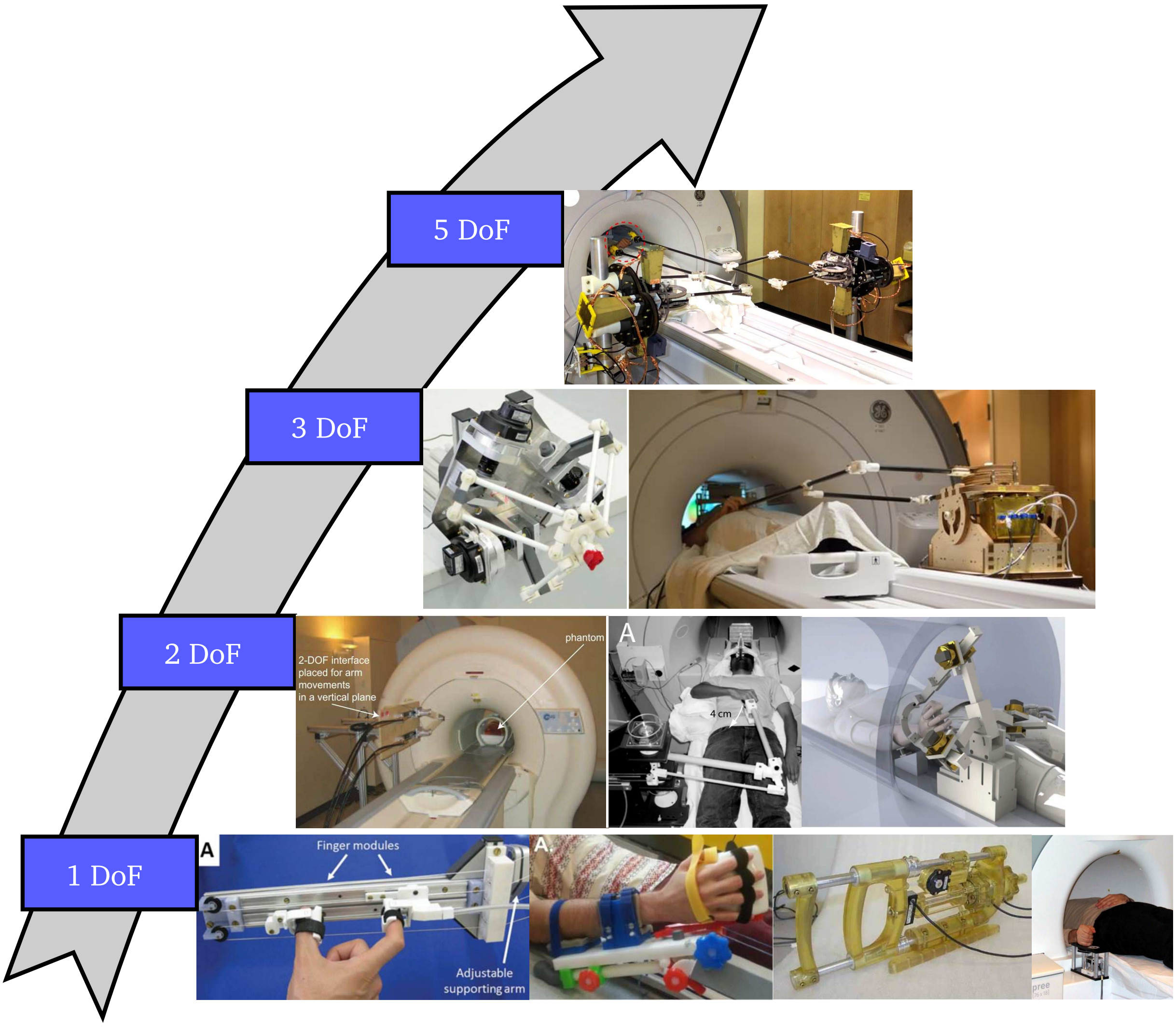
5 DoF
3 DoF
2 DoF
2-DOF interface placed for arm movements in a vertical plane
phantom
A
4 cm
1 DoF
A
Finger modules
Adjustable supporting arm
A

Figure 1.2: State of the art of MR-compatible haptic interfaces ordered by the realizable DoF: Devices with **one DoF** [11] IEEE 2015, [6] IEEE 2015, [22] IEEE 2007, [5] IEEE 2005; **two DoF** [14] IEEE 2006, [12] (Reproduced with permission from the Society for Neuroscience), [18] IEEE 2015; **three DoF** [19], [20]; and **five DoF** [21] [IEEE 2017].

rheological fluids [8], coils [7], and potential energy [13]. They have advantages for some applications but are outperformed in many ways by the currently most popular actuation technologies for MR-compatible haptic devices: USMs [5,9,18,19] and remotely-located DC motors [6,11,20]. Remotely-located DC motors possess a very mature, industrially prevalent technology combined with good controllability. However, they have to be shielded against the MR field. Moreover, motion is transmitted via rods [20] or tendons [6], which decreases stiffness and leads to bulky mechanisms. USMs are MR-compatible and can be placed close to the scanner bore, which results in smaller devices. Furthermore, they provide a high torque, are compact, and have a fast response. Some commercial products[3] are readily available, which is an advantage over experimental technologies. Thus, USMs combine a host of promising features due to which they were chosen by our group for a previous device [19] as well as a preliminary concept for a haptic device with six DoF [23]. However, known disadvantages are difficulties in realizing low speeds, velocity dead zones under load, non-linear dynamics, and a short lifetime. These issues need to be addressed when employing USMs.

---

[3] shinsei-motor.com, physikinstrumente.com, mmech.com

Tabular 1.1: MR-compatible actuation principles, partially adopted from [19].

Principle	**Pros**	**Cons**
Pneumatic transmission	clean	low frequencies, hard to control
Hydrostatic, hydraulic transmission	high forces	leaking, amount of work for setup
Electrostatic motor		high voltage
Electroactive polymers	compact	slow, high voltage
Electro-rheological fluids		no precise motion
Coils	compact	limited range of motion
Potential energy	no electronics	limited motion capabilities
Piezoelectric actuator	high forces, highly stable, precise action, compact	high voltage, short expansions
Ultrasonic motor	high torque at low speed, compact, high response, good speed controllability	no low speeds, non-linear dynamics, velocity dead zones, short lifetime
Remotely-located DC motor	mature technology	shielding necessary, transmission over long distances

The presented devices illustrate that most MR-compatible haptic interfaces rely on a parallel kinematics, i.e. a robotic structure, where the base and the end effector are connected via multiple legs. This is in contrast to a serial kinematics, where a single kinematic chain connects the end effector to the base and an actuator can be found in every joint. Devices located close to the subject in the MR scanner [12,14,15,19,23] avoid floating actuators and moving electronics that can lead to image artifacts. Devices in a distant position, e.g. behind the 400 Gauss static-field line [20], increase stiffness which is impaired due to the distance.

In conclusion, the best actuation principle within strong magnetic fields, like those generated by an MR scanner, is not established yet. Moreover, parallel kinematics are a quasi-standard for MR-compatible haptic interfaces. Finally, all existing MR-compatible haptic interfaces are specialized for a subset of possible motions with the human hand or arm. This requires building additional devices for new research questions, which is both costly and time intensive. There is a lack of a versatile MR-compatible haptic interface that allows conducting a broader range of human motor control studies combined with fMRI. Such a device would allow shifting the paradigm to reprogramming rather than redesigning when moving on to a new research question. It should alleviate neuroscientists from engineering tasks and speed up research in this field. Moreover, complex tasks involving natural, unconstrained pick-and-place motions could finally be targeted for investigation. For the first time, this would allow the characterization of brain processes that underlie natural reach-to-grasp movements, extending the types of questions in the field of visuomotor control that can be asked by neuroimaging [3].

1.2 Problem statement and challenges

The primary challenge of this thesis is to develop a universal haptic interface that provides *seven DoF* along with *bi-directional MR-compatibility*. Along these lines, the haptic interface also needs to be inherently *safe* for the operator: there should be no components that accelerate or heat up under the influence of the static magnetic field and the RF pulses of the MR scanner. Secondary challenges concern generating *sufficient output capabilities* [24], accessing the *restrained workspace* in the MR scanner as well as designing a system that is *ergonomic*. In order to address these challenges, a three-fold paradigm is followed in this thesis: it consists of the use of USMs as actuators, parallel kinematics as robot structure, and only MR-compatible components. This paradigm itself leads to further challenges detailed in the following sections.

Ultrasonic motors

Based on previous work of our group [19, 23], USMs are employed as actuators. Despite their benefits, they usually generate *purely high speeds* and *velocity dead zones* occur under load which is schematically depicted in Figure 1.3.

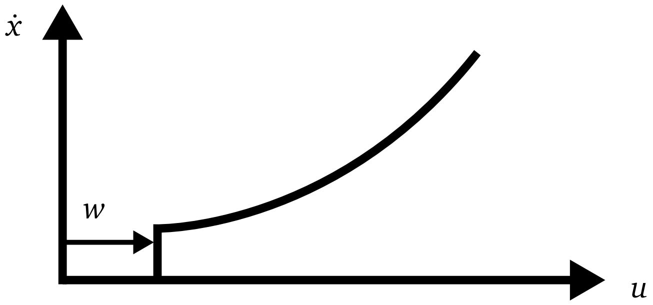

Figure 1.3: Schematic velocity behavior of a USM: The velocity $\dot{x}$ depends on the control input u and low velocities cannot be realized. Moreover, dead zones are generated and their width w grows with increasing load.

These properties are unfavorable for a haptic interface where low velocities occur frequently. Moreover, a haptic interface has to render forces as well as torques to the operator and a varying load will necessarily be applied to the motors.

Parallel kinematics

Like the presented haptic interfaces [12, 14, 15, 19, 23] the robot should avoid floating actuators and therefore, rely on a parallel kinematics. But the workspace of a parallel kinematics is limited and most of all, *direct kinematic singularities* can occur [25–27]. These singularities appear in specific configurations and lead to uncontrollable DoF at the end effector. Parallel kinematics with two DoF like a five-bar linkage [20], or three DoF like the Delta kinematics [19], do not face this problem. Both are mostly free of direct kinematics singularities by design. When targeting higher DoF, such as six or seven, these singularities become a serious issue, since the operator of a haptic interface can drive the device into a singular configuration. An example of a direct kinematic singularity is depicted in Figure 1.4. When at least two terminal links of the legs are coplanar with the end effector, an additional, uncontrollable DoF is gained. In the example, a free motion around the dashed black axis is possible. Hence, a solution to the problem of direct kinematic singularities in parallel kinematics with more than three DoF has to be found. Moreover, we have to address guaranteeing *minimum output capabilities*, allowing the kinematics to *access the restrained workspace* of the MR scanner as well as an *ergonomic usage*.

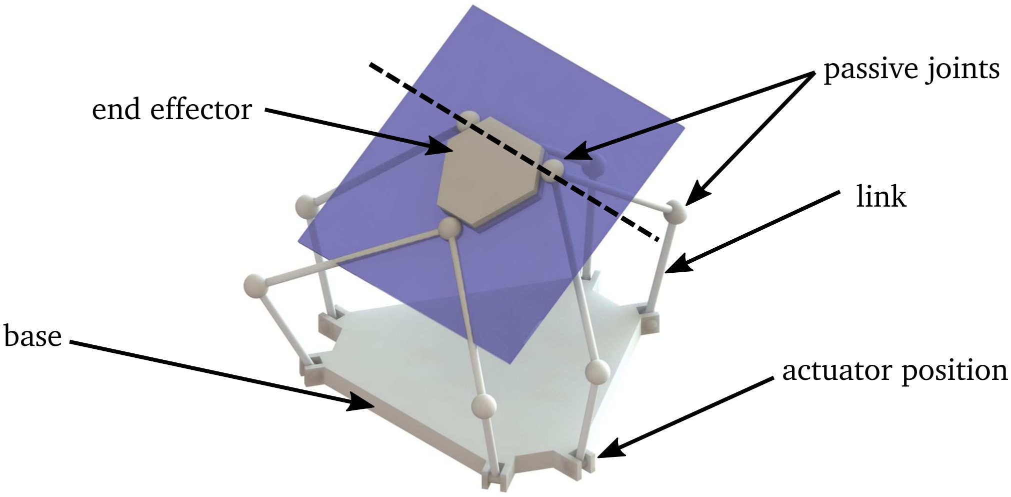

Figure 1.4: Example of a parallel kinematics with six legs in a direct kinematic singularity, where an uncontrollable DoF is gained around the dashed black axis is gained.

MR-compatible components

The use of MR-compatible components seems quite obvious. It helps avoiding image artifacts as well as safety issues and supports an unimpaired operation of the haptic interface in the magnetic field. However, it requires *iterative testing and evaluation*, since MR-compatibility cannot be guaranteed otherwise in most cases [28]. Using MR-compatible components is also in contrast to placing ferromagnetic parts of the system remote from the MR scanner and transmitting motion via rods, Bowden-cables, compressed air, or other. Hence, all parts need to be validated in terms of MR-compatibility, including actuators, bearings, and sensors.

It must also be taken into account that all hardware components have a primary function in the haptic interface. This can be e.g. providing rotational guidance with little friction in case of bearings. However, a trade-off has to be made since ideal materials for the primary function, like steel for bearings, may not be MR-compatible. Hence, achieving MR-compatibility has to be balanced with other functions of the haptic interface which makes it an *engineering challenge*.

Moreover, sensor and actuator signals are distorted by the magnetic field. Filtering or readjusting these signals can lead to control issues due to delays or lost information. Consequently, MR-compatibility also becomes a *control challenge*.

1.3 Thesis outline and contributions

This thesis is structured as follows: Chapter 2 focuses on modeling and control of USMs. In Chapter 3, a kinematics with six DoF is presented and a non-MR-compatible prototype is evaluated. The two results, controller and kinematics, are combined in Chapter 4, where a haptic interface with seven DoF is presented, and its MR-compatibility is validated. In Chapter 5, a preliminary fMRI study is carried out. Finally, conclusions are drawn in Chapter 6. The contributions of this thesis are presented in the following sections.

Modeling and two-input Sliding Mode Control of Ultrasonic Motors

In Chapter 2, a novel model for rotary traveling wave USMs along with a novel hybrid sliding mode position controller are presented. The controller does not require an explicit digital implementation of a signum function and thus, avoids chattering phenomena that are typical for sliding mode controllers. Two control inputs are used in order to realize two domains of low and high velocity. The transition from one domain to the other is shown to be smooth such that it cannot be felt by the operator of a haptic interface. Moreover, the controller copes with load-dependent dead zones.

Design and evaluation of an Octopod kinematics

The main contribution in Chapter 3 is a novel parallel kinematics with eight legs and six DoF. This actuation-redundant kinematics, which is also known as an Octopod kinematics, is systematically derived from existing kinematics with six legs and evaluated based on quantitative performance criteria. These criteria include singularity occurrence, isotropy, sensitivity as well as worst-case output capabilities. To this end, a comprehensive algorithm to determine maximum sensitivity and worst-case output capabilities of actuation-redundant parallel kinematics is introduced. Finally, the kinematics is realized as a non-MR-compatible prototype.

An MR-compatible haptic interface with seven Degrees of Freedom

In Chapter 4, an MR-compatible haptic interface is presented, employing by the controller from Chapter 2 and the kinematics from Chapter 3. The main contribution of this Chapter is an MR-compatible system with seven DoF for fMRI studies. This includes a thorough validation of the MR-compatibility and a human-factors analysis in order to ensure that the system is ergonomic and safe.

A benchmark fMRI study for versatile haptic interfaces

In Chapter 5, a benchmark fMRI study is designed and carried out. The study is intended as a means of comparison for versatile MR-compatible haptic interfaces that allow at least grasping and lifting motions. In this work, the study is employed to validate the applicability of the novel haptic interface for fMRI studies.

2 Modeling and two-input Sliding Mode Control of Ultrasonic Motors

Summary. *Ultrasonic motors (USMs) are compact actuators that generate high torques and that can be produced from non-magnetic materials. These properties make them favorable for an application inside magnetic resonance environments. However, USMs have highly non-linear dynamics, do not allow low velocities by default and dead zones appear under load. In this chapter, we aim to develop a control method that copes with these challenges. To do so, a second-order model of the motor is developed in the first step. Then and in a second step, a hybrid sliding mode position controller is designed, tested on a hardware test bench, and compared to existing state-of-the-art controllers. The controller does not require an explicit digital implementation of a signum function and thus, avoids chattering phenomena that are typical for sliding mode controllers. Moreover, the controller copes with dead zones as well as non-linearities and allows low velocities.*

2.1 Problem statement and approach

USMs are actuators based on high frequency vibration of a stator that is pressed against a rotor. The stator is a deformable body, carrying piezoelectric ceramics that create a traveling wave. The traveling wave is composed of two standing waves with frequency f and phase difference α. Force is transmitted to the rotor via a friction interface. USMs combine compactness with a high stalling torque. They also feature a fast response, silent operation, and can be exposed to strong magnetic fields such as in a magnetic resonance (MR) scanner. Hence, they have been employed in robotic, aerospace, and medical applications as well as in camera lenses [29]. Moreover, new structures are being developed [30, 31] that exploit the virtues of this type of actuator and push the possible applications to new limits. Like other researchers [32, 33] we are interested in applying this type of motor in MR environments. However, a series of disadvantages prohibit their application in many cases: USMs have highly non-linear dynamics, low speeds are difficult to control, dead zones appear when load is added to the rotor, their performance deteriorates at high temperatures [34], and their lifetime is short compared to DC motors.

Due to the benefits and despite these disadvantages, we aim to employ USMs in an MR-compatible haptic interface. This means that both low and high speeds have to be realized, since the operator should be able to perform both slow and fast movements. Moreover, a varying load is added to the rotor that simulates an opposing torque, resulting from a varying human impedance or virtual environment. We approach these challenges by means of a model-based controller. Dead zones and non-linearities are compensated for by a controller that does not require a torque measurement. Torque sensors increase the footprint in the MR environment and the likeliness of image artifacts. Low and high speeds are realized by using the phase difference and frequency as control inputs.

A range of dynamic models of USMs has been proposed, taking into account rotor, stator and friction dynamics. However, the interactions between the components are often overly complex for control design [29, 35, 36].

Simpler USM models have been proposed for control purposes that abstract the stator dynamics as a torque source and mostly neglect friction as well as dead zone dynamics [34,37–41]. Moreover, Canudas-de-Wit [42] published a model based on work by Hagood and McFarland [35] that attempts to close the gap between model complexity and control development, resulting in a velocity source model. García-Rochín et al. [43] proposed a modification to this model, including a dynamic description of the dead zone and modeling the friction interface via viscous friction, abstracting the stator as a torque source.

Based on the published USM models, a variety of controllers have been developed. Those cover PI-control [44], H∞ control [45], backstepping control [46], sliding mode control (SMC) [37, 42, 47], control by neural networks [48], and fuzzy logic [49]. The controllers use phase difference, frequency, voltage of the piezo-ceramics, or a mixture of these as control variables. Most of the controllers rely on models that neglect the dead zone dynamics and that consider the stator as a torque source [37, 45–47]. This simplifies the friction dynamics to a large extent. Hence, the design of the controllers lacks completeness, especially for applications with a varying opposing torque. Canudas-de-Wit [42] proposed a velocity controller based on his velocity source model, where the control variable is mainly the frequency of the traveling wave, while the sign of the phase difference is used to set the direction of rotation. However, only high velocities can be realized with frequency control. Controllers with multiple control inputs as proposed in [37,47] on the other hand lack a stability analysis of the resulting hybrid system. Moreover, practical issues like velocity-discontinuities arise for these approaches when the control variable is switched, as will be shown in this chapter.

In this work, we introduce a novel second-order model for traveling wave ultrasonic motors that reproduces dead zone effects and includes a dry friction driving principle. Moreover, a two-input sliding mode controller is developed that allows the control of both phase difference and frequency of the traveling wave. It does not require an explicit digital implementation of a signum function, since this function is already part of the motor model. Thus, the controller avoids chattering phenomena that are typical for SMCs. The controller extends the work by Canudas-de-Wit [42] to the position control case and allows fine-grained phase difference control. Moreover and unlike previous work, the controller does not introduce velocity jumps when the control domains of phase difference and frequency are switched. The latter is especially desirable for haptic interfaces, where the operator should not feel transitions. Finally, the model is identified with a Shinsei[1] USR60 and the controller is evaluated experimentally.

The remainder of this chapter is organized as follows: In Section 2.2, USM dynamics is derived. The two-input sliding mode controller is introduced in Section 2.3 and a stability analysis is carried out in Section 2.4. The experimental setup, the parameter identification, and the controller validation are presented in Section 2.5 and 2.6. Finally, a conclusion is drawn in Section 2.7.

---

[1] http://www.shinsei-motor.com

2.2 Dynamic model

USMs consist of three major components: Stator, rotor, and friction interface. A free body diagram of the components is depicted in Figure 2.1. Here, the stator is subject to a high frequency voltage V_0 actuating the piezoelectric ceramics and generating a traveling wave. The rotor is pressed on the stator by an axial force F_{ax}. The tangential force that is transmitted to the rotor results in a driving torque τ_{dr}. An opposing torque τ_{op} is created when load is added to the rotor.

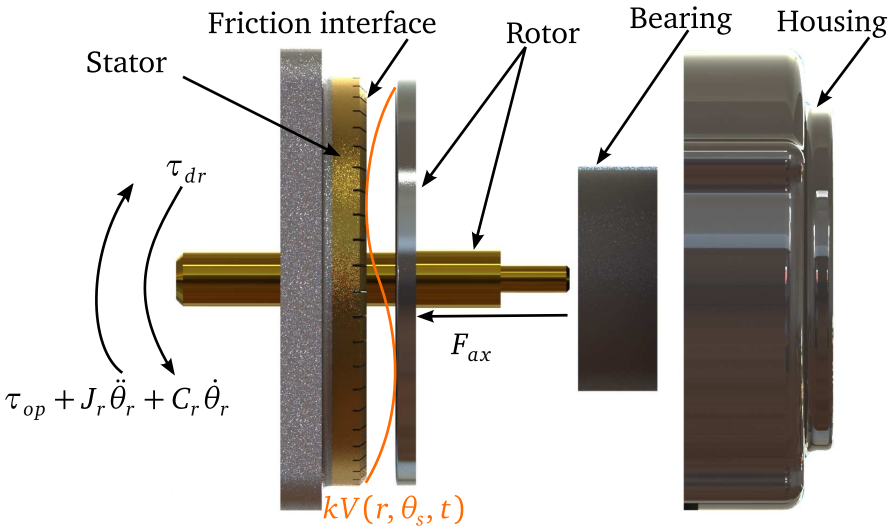

Figure 2.1: Free body diagram of a USM, in this case a Shinsei USR60.

Canudas-de-Wit [42] described the USM by

$$J_r\ddot{\theta}_r + C_r\dot{\theta}_r = r_0(\sigma_0\xi + \sigma_1\dot{\xi}) = \tau_{dr}(\xi, \dot{\xi}), \tag{2.1}$$

$$\dot{\xi} = \omega_{st} - \dot{\theta}_r - \sigma_0 \frac{|\omega_{st} - \dot{\theta}_r|}{g(\omega_{st} - \dot{\theta}_r)}\xi, \tag{2.2}$$

$$g(\omega_{st} - \dot{\theta}_r) = F_C + (F_S - F_C)e^{\frac{-(\omega_{st}-\dot{\theta}_r)^2}{\omega_0^2}}, \tag{2.3}$$

$$\omega_{st} = V_0 R(f, \omega_n)\,\mathrm{sgn}(\alpha). \tag{2.4}$$

In this model, (2.1) describes the rotor dynamics, (2.2), (2.3) represent the friction dynamics, and (2.4) is the stator velocity. The moment of inertia of the rotor J_r, the friction coefficient C_r, and the mean radius r_0 of inner and outer radius of the rotor area of contact are parameters of the rotor dynamics. The friction state ξ constitutes, together with r_0 as well as the spring-like micro-damping friction coefficients σ_0 and σ_1, the driving friction torque τ_{dr}. The LuGre friction model abstracts the friction interface as a contact between bristles and the mean deflection of the bristles is characterized by the friction state ξ. The model relies on several variables and parameters: The rotor velocity $\dot{\theta}_r$, the stator velocity ω_{st}, the Stribeck velocity ω_0, the Coulomb friction F_C, and the Stribeck friction F_S. The stator is modeled as a velocity source and its dynamics is simplified. Hence, the stator velocity ω_{st} is a function of the voltage applied to the piezoelectric material V_0, as well as the frequency of the traveling wave f, and the resonant frequency of the piezoelectric material ω_n. It also depends on the sign of the phase difference α. The non-linear dependence on the frequency of the traveling wave and the resonant frequency of the piezoelectric material is described by $R(f, \omega_n)$. This model allows controlling the motor using the frequency of the traveling wave, the voltage applied on the piezoelectric material, and the sign of the phase difference. It does not include load or the possibility to control the phase difference in the whole range of $[-\frac{\pi}{2}; \frac{\pi}{2}]$ rad. More details on the model by Canudas-de-Wit [42] can be found in Appendix A. In this work, this model is first simplified to adjust the complexity for control design. Then, it is extended to include the effects of load and a varying phase difference.

2.2.1 Simplification of the dynamic model by Canudas-de-Wit

The LuGre friction model [50] characterizes a series of known friction properties, like Stribeck effect, stick-slip motion, and produces an approximated hysteresis curve. However, it comes with an elevation of the system's order and makes control design difficult. In this work, we aim at establishing a model using a simpler friction dynamics that still reproduces the major features of a USM and that can be used for control design. According to [42] the friction dynamics is much faster than the rotor dynamics. Hence, it can be assumed that

$$\dot{\xi} = 0, \tag{2.5}$$

$$\xi = \frac{1}{\sigma_0} g(\omega_{st} - \dot{\theta}_r)\,\mathrm{sgn}(\omega_{st} - \dot{\theta}_r), \tag{2.6}$$

$$\mathrm{sgn}(x) = \begin{cases} 1 & , x > 0 \\ [-1, 1] & , x = 0 \\ -1 & , x < 0, \end{cases} \tag{2.7}$$

using Orlov's [51] definition of the signum function. With these assumptions (2.1) is reduced to

$$J_r \ddot{\theta}_r + C_r \dot{\theta}_r = r_0 g(\omega_{st} - \dot{\theta}_r)\,\mathrm{sgn}(\omega_{st} - \dot{\theta}_r). \tag{2.8}$$

Further assuming that $F_C = F_S$ and substituting $\tau_m = r_0 F_C$, the simplified model can be written as

$$J_r \ddot{\theta}_r + C_r \dot{\theta}_r = -\tau_m\,\mathrm{sgn}(\dot{\theta}_r - \omega_{st}) = \tau_{dr}. \tag{2.9}$$

This model describes the friction dynamics as pure dry friction and its solutions are understood in the Filippov sense [52].

2.2.2 Extension of the dynamic model by Canudas-de-Wit

The original model by Canudas-de-Wit does not include a load torque that leads to dead zone effects. Since we would like to design a controller for a haptic interface, where variable opposing torques will be created by the human and the rendered virtual environment, it is necessary to include this effect in the model. Therefore, the rotor dynamics (2.9) is extended by an opposing torque τ_{op}. Thus, the extended rotor dynamics is expressed as

$$J_r \ddot{\theta}_r + C_r \dot{\theta}_r = -\tau_{op} + \tau_{dr} = -\tau_{op} - \tau_m\,\mathrm{sgn}(\dot{\theta}_r - \omega_{st}), \tag{2.10}$$

with ω_{st} as control input. The stator velocity can be modulated by phase difference changes in the whole range of $[-\frac{\pi}{2}; \frac{\pi}{2}]$ rad and it is assumed that the dependency can be modeled by a sinusoidal function [43,53]. The dependency on the frequency is further assumed to be exponential [43] with the two parameters a and b. Parameter a is the maximum frequency of the traveling wave, whereas parameter b describes how rapidly the stator velocity changes when the frequency is altered. Hence, the ideal stator velocity is described by

$$\omega_i = \sin(\alpha)e^{a-bf}. \tag{2.11}$$

However, dead zones caused by an opposing torque occur in the phase difference domain [43] of the stator velocity ω_{st} as depicted in Figure 2.2. Here, these dead zones are modeled analogously to [53,54]. The stator velocity is therefore expressed as

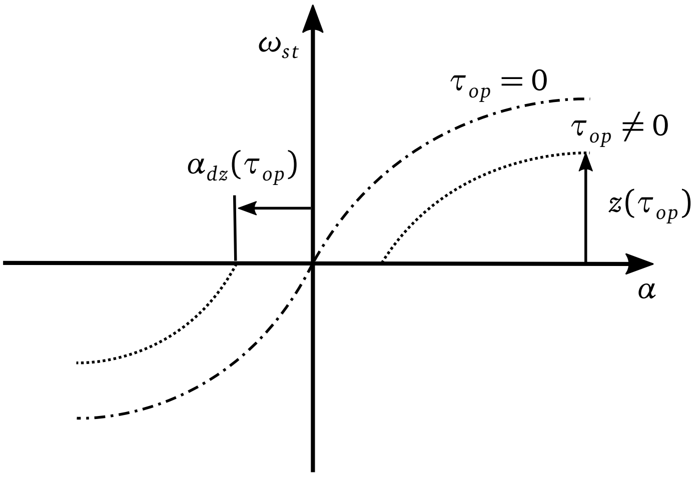

Figure 2.2: Dead zone caused by an opposing torque in the phase difference domain.

$$\omega_{st} = \begin{cases} z(\tau_{op})[\sin(\alpha) - \sin(\alpha_{dz}(\tau_{op}))]... & \\ ...[e^{a-bf} - |\sin(\alpha_{dz}(\tau_{op}))|] & ,|\alpha| > |\alpha_{dz}(\tau_{op})| \\ 0 & ,|\alpha| \leq |\alpha_{dz}(\tau_{op})|, \end{cases} \tag{2.12}$$

which describes the nonlinear impact of the opposing torque τ_{op} on the stator velocity ω_{st}. The opposing torque τ_{op} blocks the stator which results in a dead zone of width $\alpha_{dz}(\tau_{op})$. Moreover, the reduced maximum velocity under load is accounted for by $z(\tau_{op})$. For simplicity, (2.12) can be expressed as

$$\omega_{st} = \omega_i + \delta(f, \alpha, \tau_{op}). \tag{2.13}$$

2.3 Two-input sliding mode controller

Based on the second-order USM model (2.10)-(2.12), a two-input sliding mode controller has been designed. It controls both phase difference and frequency to achieve low and high velocities and does not require the implementation of a signum function. The controller extends the work by Canudas-de-Wit [42] to the position control case and allows fine-grained phase difference control. Moreover, we show its global uniform asymptotic stability (GUAS) for bounded disturbances and unlike other controllers it does not introduce velocity jumps when the control domains of phase difference and frequency are switched. The latter is especially desirable for haptic interfaces, where the operator should not feel transitions. In order to study the output tracking problem of the USM, (2.10)-(2.12) is expressed in its state space form

$$\dot{x}_1 = x_2, \tag{2.14}$$

$$\dot{x}_2 = -\frac{1}{J_r}(\tau_m \operatorname{sgn}(\dot{\theta}_r - \omega_{st}) + C_r \dot{\theta}_r) + p(\dot{\theta}_r, \tau_{op}, t), \tag{2.15}$$

$$y = x_1. \tag{2.16}$$

Here, ω_{st} is the control input, $x_1 = \theta_r - r_{ref}$ is the position error, x_2 the velocity error, and $p(\dot{\theta}_r, \tau_{op}, t) = -\frac{\tau_{op}}{J_r} - \ddot{r}_{ref}$ is a perturbation term.

2.3.1 Control laws

For a first-order sliding mode controller with sliding surface S, the control domains of phase difference and frequency control are separated by $\mu = \dot{\theta}_r - S$. The magnitude of μ determines the control domain, while the switching boundary is at $\mu = 1$. The control laws are obtained by inverting the exponential and the sinusoidal functions in (2.11) depending on frequency and phase difference, respectively and are summarized in Table 2.1. The control laws allow stabilizing (2.14), (2.15) and a smooth switching as will be shown later.

Tabular 2.1: Controls laws in the frequency and the phase difference domain.

Frequency domain ($\lvert\mu\rvert \geq 1$)	**Phase difference domain** ($\lvert\mu\rvert < 1$)
$f = \frac{1}{b}(a - \ln(\lvert\mu\rvert))$	$f = \frac{a}{b}$
$\alpha = \pm\frac{\pi}{2}$	$\alpha = \arcsin(\mu)$

Substituting the control laws into (2.14), (2.15) and with (2.13), the error dynamics in both the frequency and the phase difference domain becomes

$$\dot{x}_1 = x_2, \tag{2.17}$$

$$\dot{x}_2 = -\frac{1}{J_r}(\tau_m \operatorname{sgn}(\tilde{S}) + C_r \dot{\theta}_r) + p(\dot{\theta}_r, \tau_{op}, t) \tag{2.18}$$

and the system is forced to follow $\tilde{S}$. Here, $\tilde{S} = S - \delta(f(x_1, x_2), \alpha(x_1, x_2,), \tau_{op}) = S - \delta(x_1, x_2, \tau_{op})$ and the governing dynamics is determined by S. Thus, the control scheme can be depicted as in Figure 2.3. Beyond the domain of definition of arcsin and ln, only their real parts are used, leading to the control laws as shown in Table 2.1.

Remark: No signum function is implemented as is usually done for SMCs, since the model of the USM already includes this in its dry friction driving principle. Moreover, no explicit switching is necessary since the controller output μ naturally switches between the control domains.

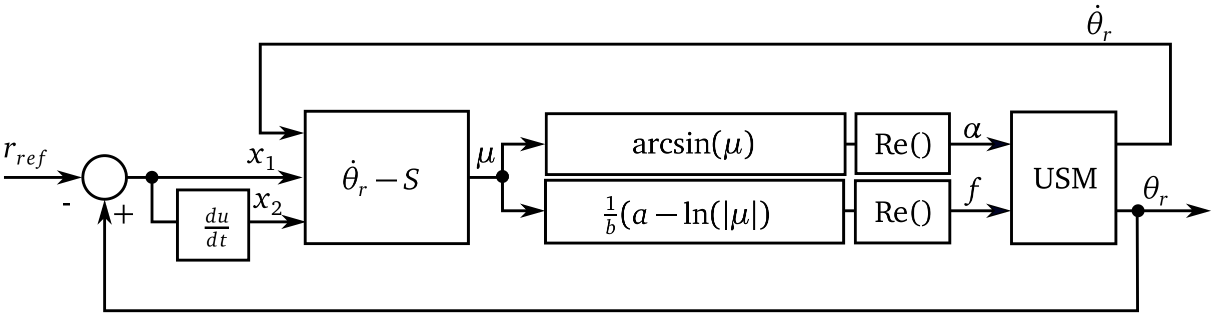

Figure 2.3: Control scheme of the two-input SMC.

2.3.2 First order sliding mode

The error dynamics (2.17), (2.18) describes a second order system with a first order sliding mode. An ideal linear sliding surface is induced by $S = x_2 + mx_1$, with $m > 0$. However, the controlled system will not follow this ideal sliding surface S, but deviate by a magnitude of $\delta(x_1, x_2, \tau_{op})$. Considering (2.12), this is expressed by a drop of the maximum reachable velocity caused by $z(\tau_{op})$ as well as a parallel shift of a the linear slope in both control domains, caused by $\sin(\alpha_{dz}(\tau_{op}))$. Ultimately, a steady state error remains, which will be quantified later. The sliding surface $\tilde{S}$ is an attractive region and we will show that (2.17), (2.18) will slide through its surface as a first order dynamical system. In order to prove this and thus, that the system is GUAS for bounded disturbances and reaches a set of equilibrium points, the common quadratic Lyapunov function

$$V(\mathbf{x}, t) = \frac{1}{2}\tilde{S}^2 \tag{2.19}$$

as in [55, 56] is chosen for both frequency and phase difference domain. Its derivative with respect to time is

$$\dot{V}(\mathbf{x}, t) = \tilde{S}\dot{\tilde{S}}. \tag{2.20}$$

Conditions $V(\mathbf{x}, t) > 0$ with $\dot{V}(\mathbf{x}, t) < 0$ have to be fulfilled to show attraction by the sliding surface and stability in the sense of Lyapunov. The first condition is always true since the Lyapunov function is quadratic. In the following subsections, it will be shown that the second condition $\dot{V}(\mathbf{x}, t) < 0$ can be fulfilled for a linear sliding surface.

2.4 Stability analysis

2.4.1 Reachability condition

With (2.17), (2.18), $S = x_2 + mx_1$, and $x_2 = \dot{\theta}_r - \dot{r}_{ref}$ the reachability condition (2.20) is then expressed as

$$\dot{V} \ = \ \tilde{S}(-\frac{\tau_m}{J_r}\operatorname{sgn}(\tilde{S}) + (m - \frac{C_r}{J_r})\dot{\theta}_r - m\dot{r}_{ref} + p(\dot{\theta}_r, \tau_{op}, t) - \dot{\delta}(x_1, x_2, \tau_{op})). \tag{2.21}$$

The perturbation $p(\dot{\theta}_r, \tau_{op}, t) - \dot{\delta}(x_1, x_2, \tau_{op}) + (m - \frac{C_r}{J_r})\dot{\theta}_r - m\dot{r}_{ref}$ has an upper bound $|p(\dot{\theta}_r, \tau_{op}, t) - \dot{\delta}(x_1, x_2, \tau_{op}) + (m - \frac{C_r}{J_r})\dot{\theta}_r - m\dot{r}_{ref}| < M_l$. For the special case of $m = \frac{C_r}{J_r}$ the state dependency vanishes and no estimate of the maximum achievable velocities $\dot{\theta}_r$ and the tracking error x_2 is necessary. In any case, the upper bound of the reachability condition is

$$\begin{aligned} \dot{V} &< \tilde{S}(-\frac{\tau_m}{J_r}\operatorname{sgn}(\tilde{S}) \pm M_l), \\ &= -|\tilde{S}|(\frac{\tau_m}{J_r} \mp M_l \operatorname{sgn}(\tilde{S})), \\ &< -|\tilde{S}|(\frac{\tau_m}{J_r} - M_l). \end{aligned} \tag{2.22}$$

In order to show $\dot{V}(\mathbf{x}, t) < 0$, the condition that must be satisfied is

$$\tau_m > J_r M_l \quad \forall \quad \tilde{S} \neq 0. \tag{2.23}$$

2.4.2 Equilibrium set and steady state error

From condition (2.23) an equilibrium set Ω can be identified for $mx_1 = \delta(x_1, x_2, \tau_{op})$ and $x_2 = 0$. It results from the definition of the stator velocity (2.12) and the resulting dead zone in the phase difference domain as shown in Figure 2.2. Thus, the opposing torque leads to a steady state position error Δx_1 for $x_2 = 0$. The precision of the controller can be estimated by solving (2.12) using the steady state condition $\omega_{st} = \dot{r}_{ref} = 0$. With the control laws in Table 2.1, the stator velocity in the phase difference domain is expressed as

$$\omega_{st} = z(\tau_{op})[\mu - \sin(\alpha_{dz}(\tau_{op}))][1 - \sin(\alpha_{dz}(\tau_{op}))]. \tag{2.24}$$

Since μ is defined as

$$\mu = \dot{\theta}_r - S,$$

it can be reformulated with $S = x_2 + mx_1$ to

$$\mu = \dot{\theta}_r - x_2 - mx_1.$$

Using $\dot{r}_{ref} = \dot{\theta}_r - x_2$, μ finally becomes

$$\mu = \dot{r}_{ref} - mx_1. \tag{2.25}$$

With this expression for μ we can reformulate (2.24) to

$$\omega_{st} = z(\tau_{op})[\dot{r}_{ref} - mx_1 - \sin(\alpha_{dz}(\tau_{op}))][1 - \sin(\alpha_{dz}(\tau_{op}))]. \tag{2.26}$$

In steady state $\omega_{st} = \dot{r}_{ref} = 0$ and under the condition that $\sin(\alpha_{dz}(\tau_{op})) < 1$, the steady state error can be estimated as

$$|\Delta x_1| = |\frac{1}{m}(\sin(\alpha_{dz}(\tau_{op}))|. \tag{2.27}$$

Thus, the equilibrium set is defined as

$$\Omega = \{\mathbf{x} \in \mathbb{R}^2 \quad | \quad |x_1| \leq |\frac{1}{m}(\sin(\alpha_{dz}(\tau_{op}))|, x_2 = 0\}. \tag{2.28}$$

2.4.3 Smooth switching of the variable structure system

Sliding modes and velocity jumps should not occur along the switching boundary. This can be ensured by guaranteeing a transversal intersection [57] at the switching boundary. The condition for a transversal intersection is

$$\mathbf{n}^T(\mathbf{x})\mathbf{f}_+(\mathbf{x}) \cdot \mathbf{n}^T(\mathbf{x})\mathbf{f}_-(\mathbf{x}) > 0, \tag{2.29}$$

where $\mathbf{n}^T(\mathbf{x})$ is the normal to the switching boundary and $\mathbf{f}_\pm$ is the state vector of the variable structure system on both sides of the switching boundary. From (2.25) it is known that the condition for switching μ is only a function of the reference velocity $\dot{r}_{ref}$ and the position error x_1. Thus, $\mathbf{n}^T(\mathbf{x}) = [0\ 1]^T$. Here, three situations in which the switching may occur have to be analyzed for smoothness in the states: This can be a switching during the reaching phase on either side of the phase portrait or a switching during the sliding phase on the sliding surface. Therefore (2.17) and (2.18) are written in state space form $\mathbf{f}_\pm$, when α approaches $\frac{\pi}{2}$ rad and f approaches $\frac{a}{b}$.

Case 1: Reaching phase, $\tilde{S} < 0$

In the first case, the system is in the reaching phase and $\tilde{S} < 0$. The dry friction term takes the form of $\text{sgn}(\tilde{S}) = -1$ and the state representation at the switching boundary is

$$\mathbf{f}_\pm = \begin{pmatrix} x_2 \\ -\frac{1}{J_r}(-\tau_m + p(\dot{\theta}_r, \tau_{op}, t)) \end{pmatrix}. \tag{2.30}$$

Case 2: Reaching phase, $\tilde{S} > 0$

In the second case, the system is in the reaching phase and $\tilde{S} > 0$. The dry friction term takes the form of $\text{sgn}(\tilde{S}) = 1$ and the state representation at the switching boundary is

$$\mathbf{f}_\pm = \begin{pmatrix} x_2 \\ -\frac{1}{J_r}(\tau_m + p(\dot{\theta}_r, \tau_{op}, t)) \end{pmatrix}. \tag{2.31}$$

Case 3: Sliding phase, $\tilde{S} = 0$

In the third case, the system is on the sliding surface and reduced to a first order dynamical system. The Filippov continuation method is applied and the simplified dynamics of the system is described by

$$S = x_2 + mx_1 = \delta(x_1, x_2, \tau_{op}) \tag{2.32}$$

and then the state representation of the original second order system takes the form of

$$\mathbf{f}_\pm = \begin{pmatrix} x_2 \\ \dot{\delta}(x_1, x_2, \tau_{op}) - mx_2 \end{pmatrix}. \tag{2.33}$$

In all three cases, the gradients of the two controlled systems align at the switching instant, which provides a smooth switching without velocity jumps.

2.5 Experimental identification of the dynamic model

In order to identify (2.10)-(2.12) and to validate the controller, a testbed has been set up as in [43]. It allows the simulation of opposing torques and to control both phase difference and frequency, while recording the velocity of the motor. On the testbed, a USM with attached encoder is connected to a torque sensor and a magnetic brake. The USM is a USR60-E3NT from Shinsei. It provides a rated speed of 100 rpm with a maximum of 150 rpm. The rated torque is 0.5 Nm, whereas the maximum torque is 1 Nm. The motor driver has been modified such that both frequency and phase difference of the traveling wave can be controlled: The phase difference can be set within the range of $[-\frac{\pi}{2};\ \frac{\pi}{2}]$ rad and the frequency within the range of $[41;\ 44]$ kHz. The attached encoder can measure 4000 pulses/round in quadrature. The torque sensor is a TS70 from ME-Messsysteme and has a rated torque of 2 Nm. The magnetic brake of type FAS 21 from LIEDTKE Antriebstechnik can generate a maximum torque of 2 Nm. The details of the testbed are summarized in Table 2.2. The workstation is equipped with a Mecovis I/O card that generates two voltage bands in the range of $[-10;\ 10]$ V. The motor driver converts these voltage bands to the phase difference and frequency of the traveling wave. The Mecovis I/O card also sets the opposing torque and reads the position signals from the encoder as well as the torque signal from the torque sensor. Matlab/Simulink is used for command generation and the compiled code is run with a Linux real-time kernel at a sampling rate of 1 kHz.

Tabular 2.2: Characteristic figures of the experimental setup.

Parameter	Value
USM model	**USR60-E3NT**
Rated (maximum) speed	100 rpm (150 rpm)
Rated (maximum) torque	0.5 Nm (1 Nm)
Driving frequency	[41; 44] kHz
Driving phase difference	$[-\frac{\pi}{2};\ \frac{\pi}{2}]$ rad
Torque sensor model	**TS70**
Rated sensed torque	2 Nm
Magnetic brake model	**FAS21**
Maximum brake torque	2 Nm

The signal flow between workstation and testbed is depicted in Figure 2.4.

The hardware setup of the testbed is depicted in Figure 2.5. It shows how motor, encoder, torque sensor, and magnetic brake are connected.

The original and modified motor driver are shown in Figure 2.6. An SMD board has been designed for this purpose and it is equipped with some of the original components, but also new ICs to realize fine-grained phase difference control in addition to frequency control.

2.5.1 Experimental procedures

During the data recording, the phase difference and frequency of the motor are controlled and an opposing torque is generated. A range of curves is recorded: The phase difference is

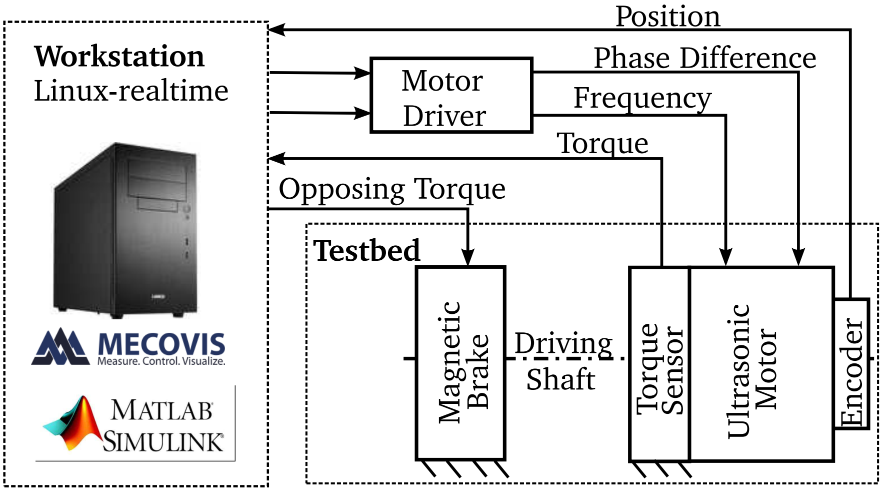
Workstation
Linux-realtime
MECOVIS
Measure. Control. Visualize.
MATLAB
SIMULINK
Motor Driver
Position
Phase Difference
Frequency
Torque
Opposing Torque
Testbed
Magnetic Brake
Driving Shaft
Torque Sensor
Ultrasonic Motor
Encoder

Figure 2.4: Scheme of the signal flow between workstation and testbed.

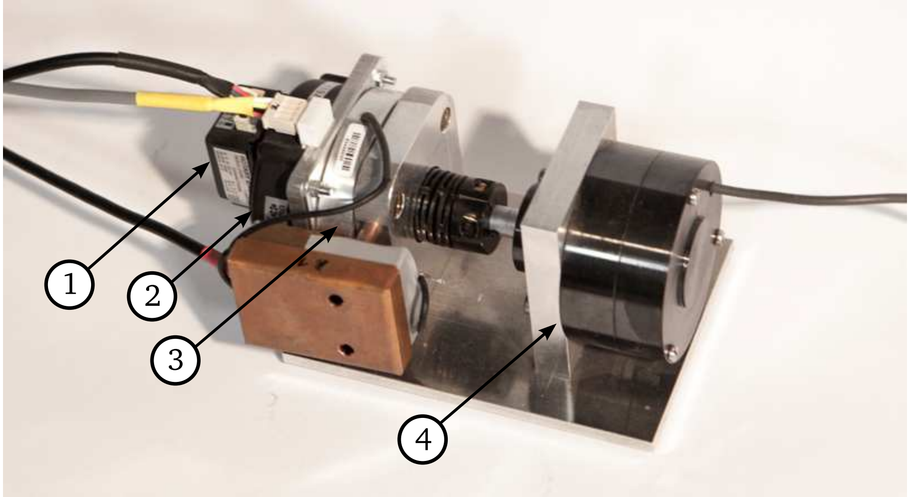

Figure 2.5: Photograph of the testbed with (1) Encoder, (2) USM, (3) torque sensor, and (4) magnetic brake.

controlled continuously in the range of $[-\frac{\pi}{2};\ \frac{\pi}{2}]$ rad and the frequency at steps of 0.5 kHz in the range of $[41;\ 44]$ kHz. The magnetic brake allows to set a load torque at eleven different levels. This procedure has been adopted from [43] to obtain comparable results and considers only opposing torques below the rated torque of 0.5 Nm, since excessive torques may shorten the motor's lifetime. The velocity of the motor at a minimum opposing torque and for varying phase difference and frequency is depicted in Figure 2.7. A complete interpolation of the data is depicted in Figure 2.8.

2.5.2 Methods for model parameter identification

In order to identify the USM model (2.10), (2.12), the brake simulates the opposing torque such that

$$\tau_{op} = \tau_b \operatorname{sgn}(\dot{\theta}_r), \tag{2.34}$$

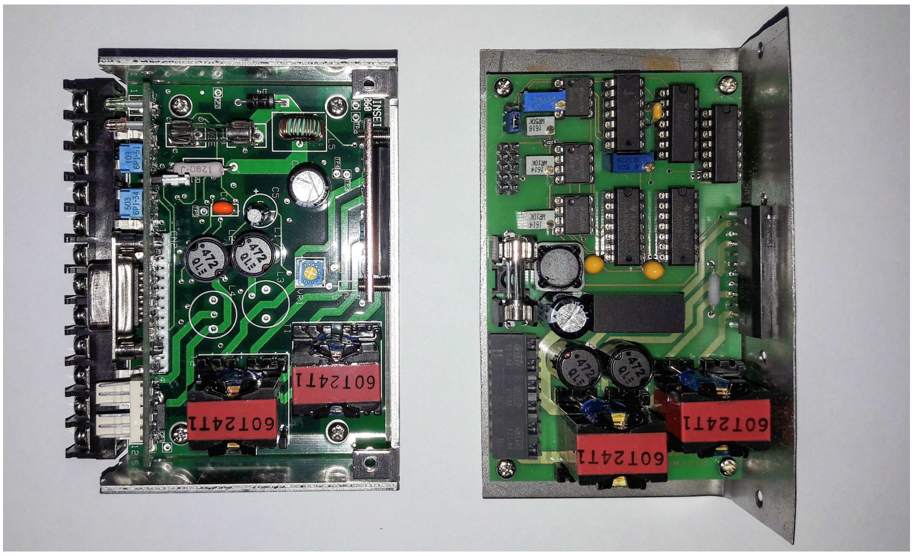

Figure 2.6: Photograph of the original (left) and modified (right) motor driver.

where τ_b is the brake torque. Thus, the parameters J_r, τ_m, C_r, and function $z(\tau_{op})$ remain to be identified.

First, the inertia J_r is the sum of the inertia of the motor and the magnetic brake, which can be found in the datasheets. The torque producible by the motor is equivalent to the rated torque, which can also be found in the datasheet of the motor. A method for identifying the viscous friction coefficient C_r of a similar model has been presented in our previous work [43]. The same approach that is based on a step response and the time constant of the USM can be used here. Finally, in order to quantify the impact of the load torque τ_{op} on the stator velocity ω_{st}, the function describing the dead zone width is identified. It is described by $\alpha_{dz}(\tau_{op})$ such that the motor stalls for all $|\alpha| < |\alpha_{dz}(\tau_{op})|$. We assume a linear function as in [43] and define it piece-wise

$$\alpha_{dz}(\tau_{op}) = \begin{cases} q_0 + q_1\tau_{op} & , \tau_{op} > 0 \\ [-q_0, q_0] & , \tau_{op} = 0 \\ -q_0 + q_1\tau_{op} & , \tau_{op} < 0. \end{cases} \tag{2.35}$$

2.5.3 Model identification results

All parameters have been identified from datasheets and recorded data from the testbed. The inertia of the USR60 is $J_m = 7.2 \cdot 10^{-6}$ kgm^2 and the magnetic brake has an inertia of $J_b = 10^{-5}$ kgm^2. Therefore, the inertia of the test setup is $J_r = 17.2 \cdot 10^{-6}$ kgm^2. The viscous friction can be identified as $C_r = 2.46 \cdot 10^{-4}$ Nms [43]. Also using the datasheet of the USM, the rated torque $\tau_m = 0.5$ Nm is identified. The relationship between the opposing torque τ_{op} and the width of the dead zone $\alpha_{dz}(\tau_{op})$ can be interpolated with the linear function such that $q_0 = 1.233$ rad/Nm and $q_1 = 0.027$ rad [43]. Finally, the individual terms defining the stator velocity ω_{st} can be identified. The parameters of the exponential function are identified as $a = 44$, $b = 1$ by interpolation. The correction term is then interpolated as $z(\tau_{op}) = 1 + 2\tau_{op}$. The identified parameters of (2.10)-(2.12) are summarized as in Table 2.3.

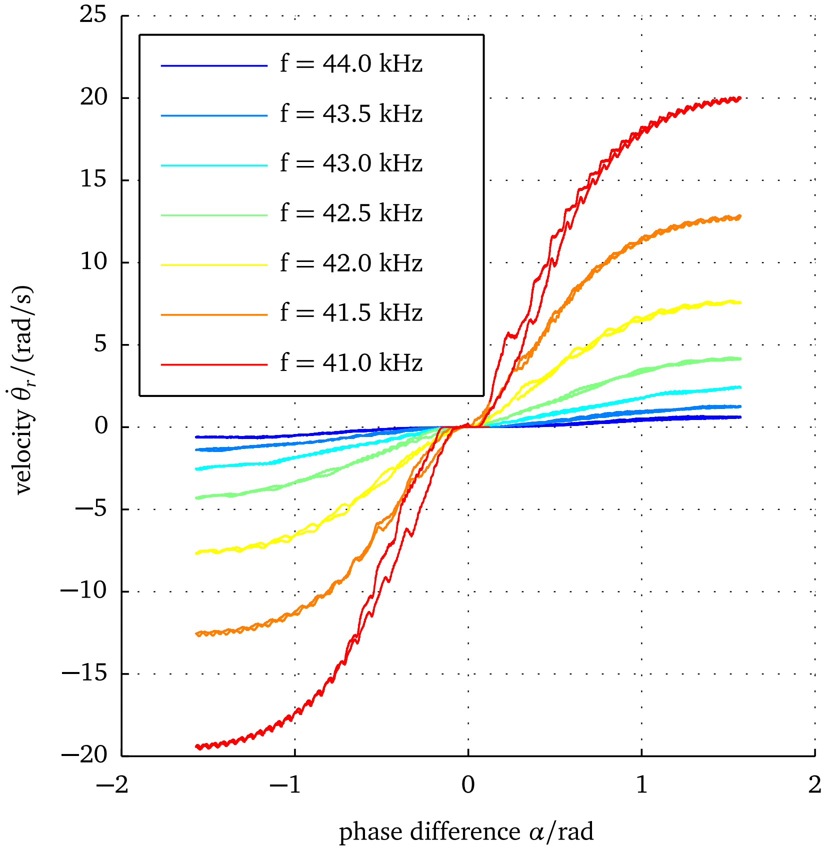

Figure 2.7: USM velocity depending on phase difference and frequency at minimum load.

Tabular 2.3: Identified model parameters and functions.

Parameter	**Value**
J_r	$17.2 \cdot 10^{-6}$ kgm^2
τ_m	0.5 Nm
C_r	$2.46 \cdot 10^{-4}$ Nms
$z(\tau_{op})$	$1 + 2\tau_{op}$
q_0	1.233 rad/Nm
q_1	0.027 rad

Plots of the dependency between phase difference, frequency, and velocity that were simulated with a time step of $1 \cdot 10^{-7}$ s are depicted in Figure 2.9. A superposition of all curves at different opposing torques is depicted in Figure 2.10. The model reproduces the sinusoidal shape of the phase difference dependency as well as the exponential shape of the frequency dependency. Dead zones are modeled, but hysteresis are not captured. The root mean square (RMS) error of the model at different frequencies and loads was computed: The maximum RMS error occurs for a minimum load at a minimum frequency and is 2.3 rad/s. For higher loads it does not exceed 2.0 rad/s for any frequency. For frequencies higher than 42 kHz the

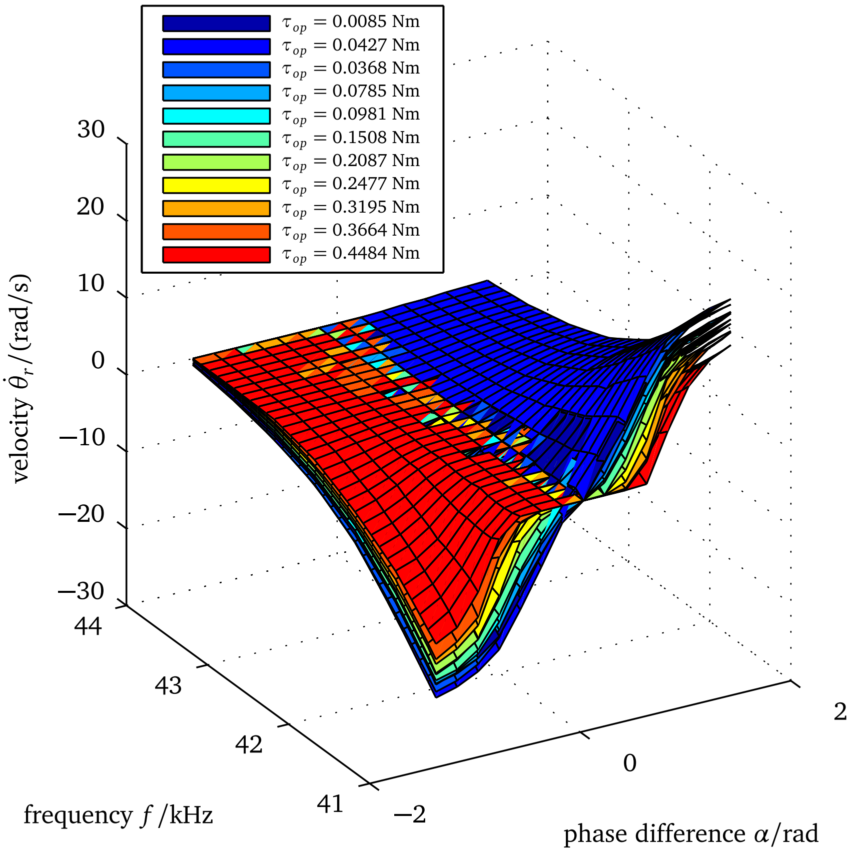

Figure 2.8: Interpolated USM velocity, depending on phase difference, frequency and torque.

error does not exceed 1.2 rad/s for every load used during the identification.

2.6 Controller validation in simulation and experiments

In order to validate both model and controller, the two-input controller was implemented on the testbed, using a sampling rate of 1 kHz, and simulated with the model, using a time step of $1 \cdot 10^{-8}$ s. The reference trajectory r_{ref} was a position step input of 1 rad at opposing torques of 0.0085 Nm and 0.4484 Nm. The controller gain was set to $m = \frac{C_r}{J_r} = 14.30$. Note, that this a design choice and covers the case where the state dependency vanishes in (2.23). With the identified parameters of the model, listed in Table 2.3, and using (2.27) the precision of the novel two-input controller can be estimated as $|\Delta x_1(0.0085\text{ Nm})| \leq 0.0026$ rad in the best case and $|\Delta x_1(0.4484\text{ Nm})| \leq 0.0383$ rad in the worst case. Higher controller gains m can further decrease the remaining steady state error as indicated in (2.27).

The corresponding phase portrait is depicted in Figure 2.11, where the region of phase difference control using the model is highlighted by a shaded area. The width of this area is determined by parameter a, since the maximum frequency of the traveling wave determines the minimum velocity in the frequency domain. In order to show the performance of the velocity source model, the controller was also simulated with the torque source model by

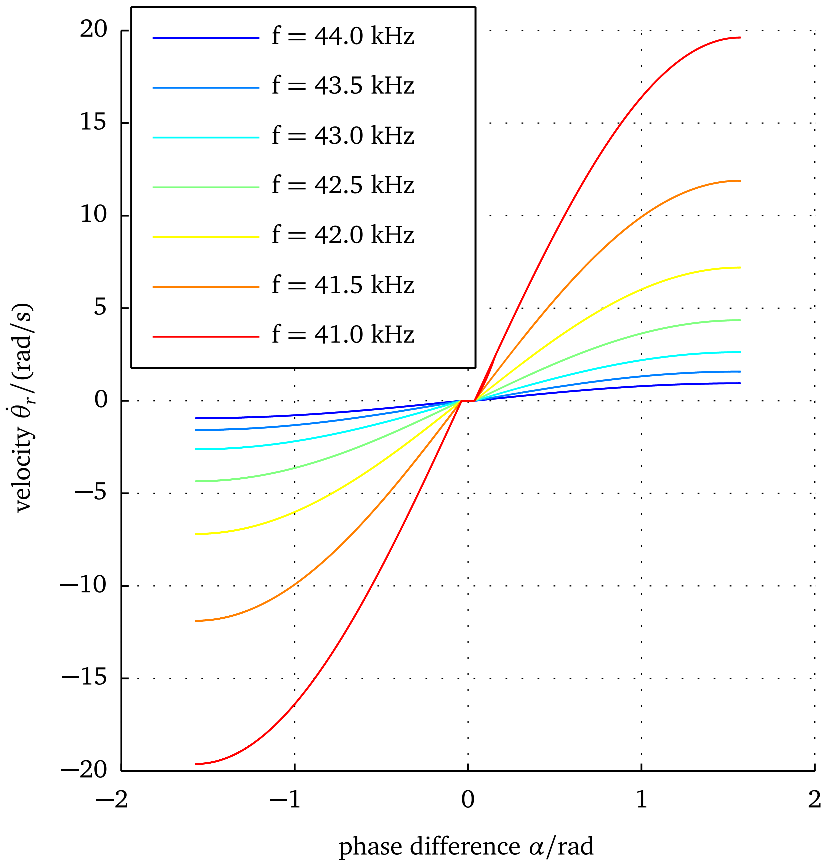

Figure 2.9: Modeled velocity depending on phase difference and frequency at minimum load.

García-Rochín et al. [43]. Note, that with the torque source model, a signum function has to be implemented in the controller to achieve a sliding mode.

The performance of the novel controller was further compared to other hybrid position controllers for USMs, using phase difference and frequency as control inputs: A dual SMC/P-controller with adaptive dead zone compensation [47] and a two-input H∞ controller [45].

Since the novel position controller is based on the work by Canudas-de-Wit [42], who developed a one-input velocity controller, it is also important to highlight the advancements. Canudas-de-Wit did not identify a USM to provide a control law $R(f, \omega_n)$ for the frequency domain [42] nor did he apply his controller to a real USM. Hence, it is difficult to compare our results in simulation or experiment. But to highlight the importance of the newly-introduced fine-grained phase difference control, our controller was also implemented as a one-input controller on the model.

The evaluation highlights, how the main issues of USMs are addressed by our novel controller. First of all and similar to standard SMCs [47], non-linear dynamics are dealt with by reducing the order of the controlled system to a first-order one. Secondly, as in [45, 47] low speeds are realized using the phase difference as a control input. This is in contrast to the work by Canudas-de-Wit [42], where low speeds are not realizable. Finally and unlike previous work [42, 45, 47], dead zones are reduced without creating chattering or overshoot effects. Moreover, the remaining steady state error can be estimated.

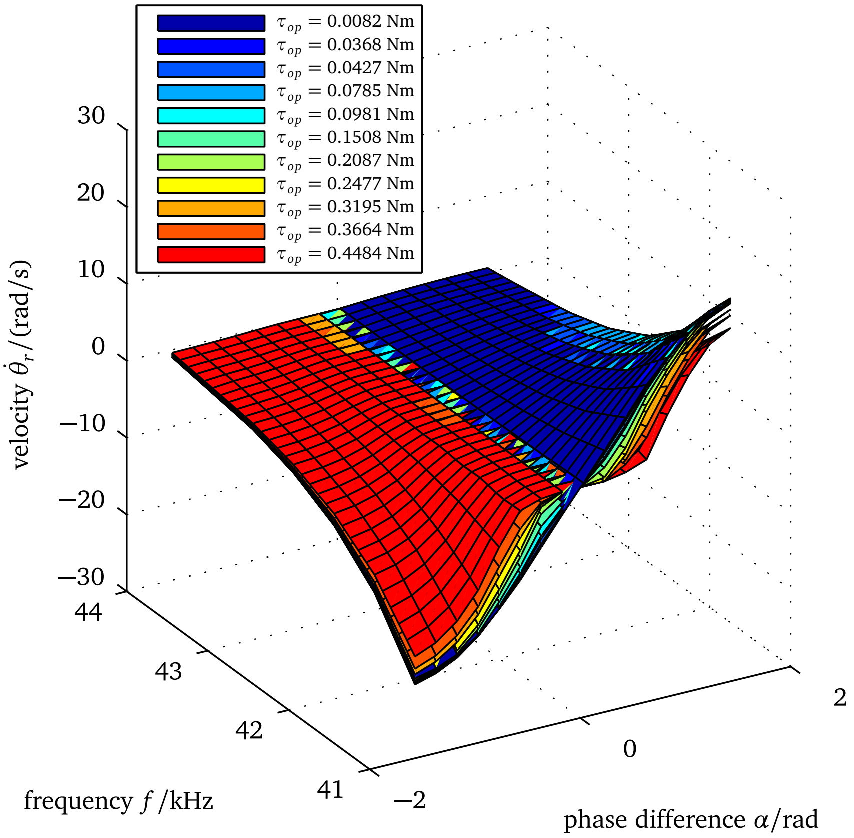

Figure 2.10: Modeled USM velocity, depending on phase difference, frequency, and torque of the model.

Comparison of simulation and experiment of the novel two-input controller: For the novel two-input controller, implemented on the model and that abstracts the stator as a velocity source, the step response in the phase portrait in Figure 2.11 shows a reaching and a sliding phase, with a slope of $m = 14.30$ for a minimum opposing torque τ_{op}. This is in accordance with the experimental results, where the same controller is used on the testbed. The position errors below a certain margin are only corrected by phase difference control, while the frequency is saturated. The frequency of oscillations increases close to the origin, as can be seen for the two-input SMC during the experimental validation, which should not be confused with chattering. This originates from the velocity quantization due to the resolution of the used encoder and sampling time. The model however, does not reproduce this effect, since it does not take into account the encoder precision. The remaining steady state position error of the two-input SMC has a magnitude of $|\Delta x_{1,exp}(0.0085\ \mathrm{Nm})| = 0.0088$ rad in the experiment and is marked with a magenta circle in the closeup. The simulation has an error of $|\Delta x_{1,sim}(0.0085\ \mathrm{Nm})| = 0.0026$ rad, as it has been estimated, and the endpoint is marked by a blue circle. Similar calculations can be done for the maximum load case. Note that the states come to a rest near the origin and do not oscillate infinitely. The discrepancy of the steady state error results most likely from neglected friction effects and the interpolation of the model parameters. Moreover, the velocity source model overestimates the drop of maximum

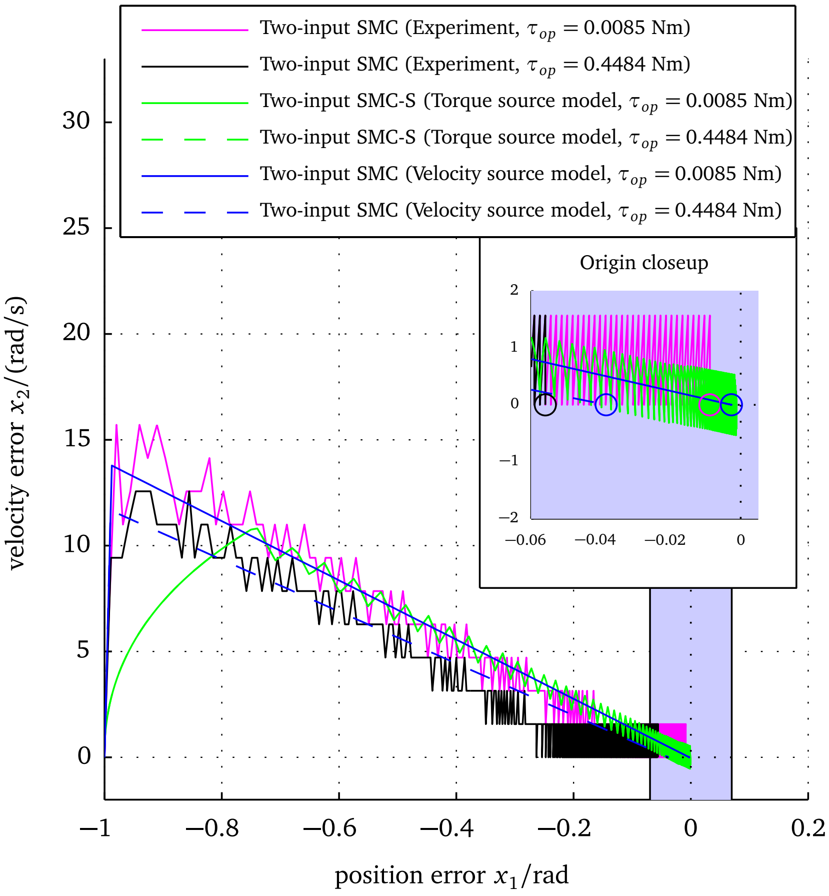

Figure 2.11: Phase portrait of controlled systems in experiment and in simulation after a 1 rad position step input.

velocity under higher loads. Thus, the simulated slopes depicted in blue in Figure 2.11 are not perfectly parallel.

Figure 2.12 shows the velocity performance of the controlled system over time. For visibility, only the simulated system is depicted and the phase difference control domains are shown as shaded areas to the right. The velocity decreases in an exponential manner and converges to zero. Moreover, the smooth switch between the control domains is clearly visible. The time instant of the switch depends on the opposing torque and increases with increasing torque.

Comparison of velocity and torque source model: A comparison with a sliding mode based on a torque source model as in [43] can only be realized by adding an additional signum function to the two-input SMC. The simulation result of such a two-input SMC with signum function (SMC-S) with a torque source model is depicted in green in Figure 2.11. In practice, the use of a signum function minimizes the steady state error, but leads to chattering as can be seen in Figure 2.11.

Comparison with other two-input controllers: The proposed velocity-source model is employed to compare the performance of the novel two-input controller to other hybrid

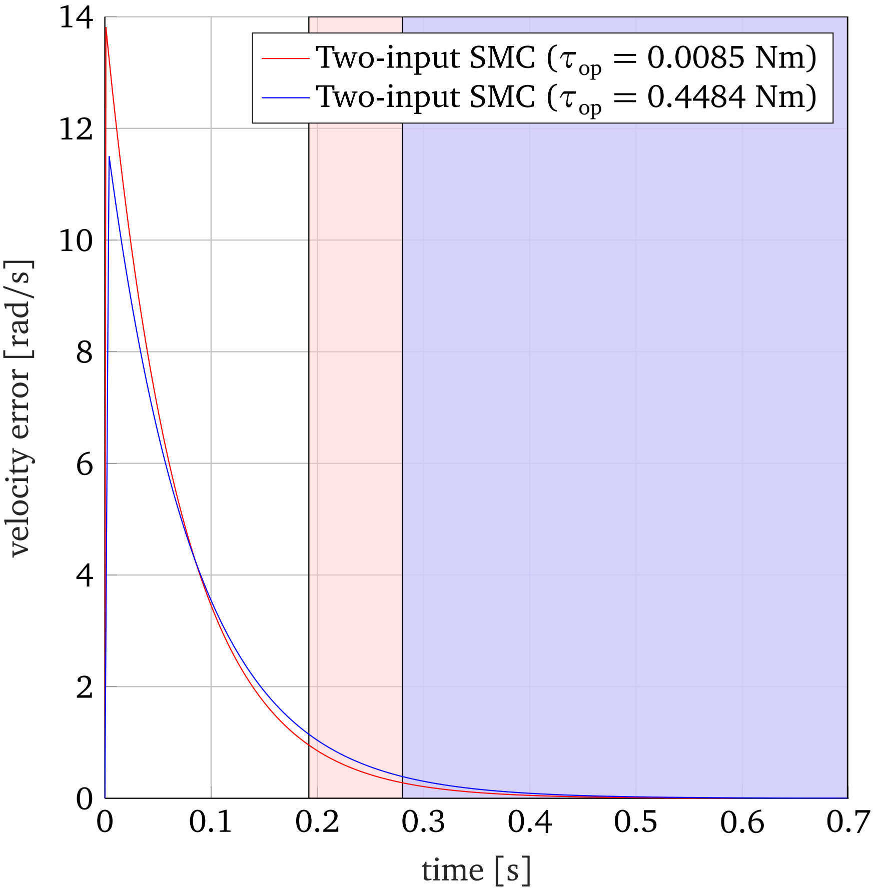

Figure 2.12: Velocity error x_2 over time on the proposed velocity source model after a 1 rad position step input. The phase difference control domains in case of minimum and maximum opposing torque τ_{op} start at different time instants. The domains are shown as shaded orange and blue area, respectively.

position controllers for USMs using phase difference and frequency as control inputs. Senjyu [47] introduced a dual SMC/P controller, where the phase difference is controlled via a SMC controller and the frequency via a proportional controller. The reaction to a 1 rad position step input is depicted in black in Figure 2.13. The control switch takes place when $\alpha = \frac{\pi}{2}$ rad and the frequency is controlled in the range of $[41;\ 41.5]$ kHz. Hence, the control switch takes place at higher velocities, compared to the two-input SMC. This results in two disadvantages: First, the motor is mainly controlled in the phase difference control domain, which has serious consequences for the motor's already short lifetime [58]. Second, the control switch introduces a discontinuity of the velocity, which is highlighted with an arrow in Figure 2.13. For haptic applications smoothness of the states is necessary. Finally, this controller foresees a digital implementation of a signum function for the SMC in the phase difference domain. This leads to chattering effects on a real USM and can be avoided, if the signum function is identified as a part of the USM.

Also a two-input H∞ controller [45] has been proposed to control USMs via phase difference and frequency. However, in the minimum load case it introduces a massive overshoot of the system, depicted in magenta in Figure 2.13.

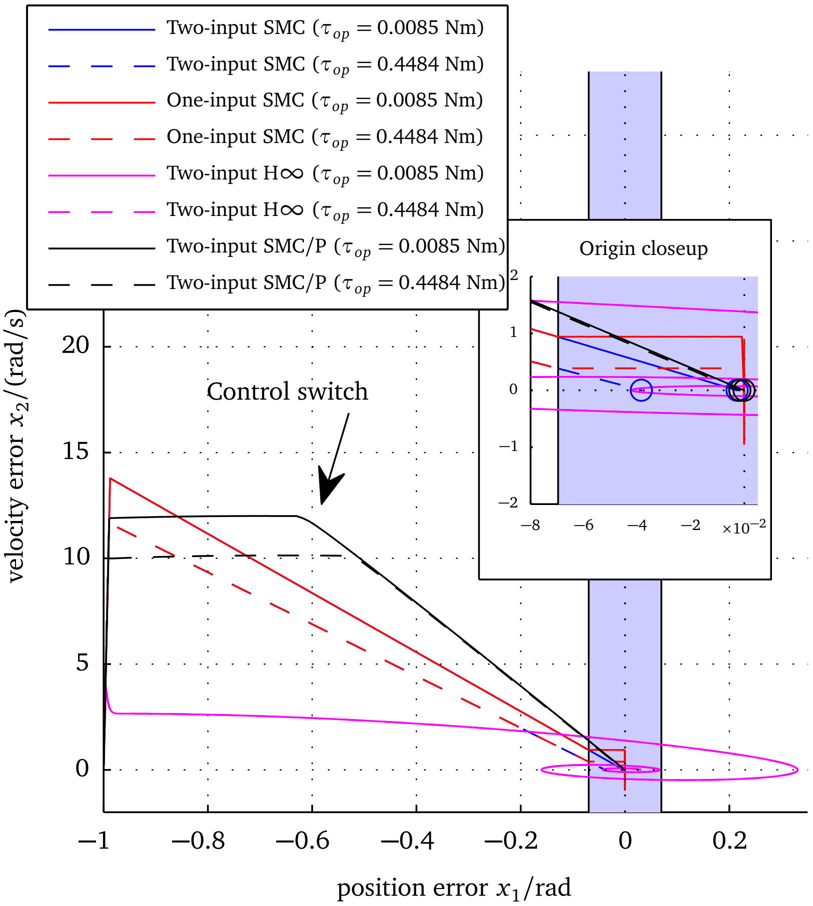

Figure 2.13: Phase portrait of controllers on the proposed velocity source model after a 1 rad position step input.

Finally, in order to compare our work to the original idea by Canudas-de-Wit [42], our controller has been implemented such that it only changes the sign of the phase difference. This is depicted in red in Figure 2.13. Since the frequency saturates at a non-zero velocity, a position can only be held while oscillating around it with positive and negative velocities. Thus, chattering around zero remains for this controller.

The controllers are additionally compared using two performance indices: The time to reach a steady state position and the control effort. The applied definition for a steady state is $x_2 < 0.01$ rad/s, whereas the control effort is expressed as the integral of $|\mu|$. Table 2.4 shows the time required for the different controllers and load cases to reach a steady state. The one-input SMC performs best in the minimum load case, the two-input SMC/P controller performs best in the maximum load case, and the H_∞ controller performs worst in both cases. The proposed two-input SMC reaches the steady state slower than the one-input SMC. The former reduces the velocity using phase differences in the whole range of $[-\frac{\pi}{2}; \frac{\pi}{2}]$ rad and thus, is slower but avoids chattering around zero velocity.

Control efforts are used as a further comparison of the controllers. In order to compare the controllers on a common basis, μ is calculated for every controller type from the phase difference as well as frequency commands and using the control laws listed in Table 2.1. The results of the integral of $|\mu|$ are listed in Table 2.5. Clearly, the proposed two-input SMC

Tabular 2.4: Time until a steady state position with $x_2 < 0.01$ rad/s is reached.

Controller	$\tau_{op} = 0.0085$ Nm	$\tau_{op} = 0.4484$ Nm
Two-input SMC	0.52 s	0.58 s
One-input SMC	0.27 s	0.46 s
Two-input H_∞	> 0.7 s	> 0.7 s
Two-input SMC/P	0.39 s	0.40 s

performs best, whereas the two-input SMC/P controller performs worst for both cases. The control effort expresses some of the advantages that can be observed in Figure 2.13: Chattering around zero velocity is avoided along with over-shooting, which add to an increased control effort.

Tabular 2.5: Control efforts expressed by the integral of $|\mu|$.

Controller	$\tau_{op} = 0.0085$ Nm	$\tau_{op} = 0.4484$ Nm
Two-input SMC	1.06	1.54
One-input SMC	1.47	1.69
Two-input H_∞	3.01	3.01
Two-input SMC/P	8.53	8.53

2.7 Conclusion

We have obtained a novel second-order model for rotary traveling wave USMs that abstracts the stator as a velocity source and includes a dynamic description of the dead zone. The dynamics of the stator is simplified and the model neglects the stator vibration velocity. We have shown that a two-input sliding mode controller, using frequency and phase difference as commands, is GUAS for bounded disturbances in both control domains. This two-input hybrid position controller extends the velocity controller by Canudas-de-Wit to the position control case and allows fine-grained phase difference control. The novel controller performs better than a hybrid SMC/P or dual H∞ controller that have been proposed in literature, since it switches the control domains without a discontinuity of the velocity, reduces the amount of phase difference control and does not produce overshoot.

Future work will need to address the validity of the model under temperature disturbance. But most importantly, the life time of the USMs using this controller needs to be quantified. The abrasion processes that act on the friction layer that determine the life expectancy, might be different in the two control domains. Moreover, procedures to either restore the friction layer or further control methods to protect it should be devised.

Despite these tasks for future work, the controller can be employed for an MR-compatible haptic interface. Hence, the actuation principle is defined and the next step is to determine the robot structure, i.e. its kinematics.

3 Design and Evaluation of an Octopod Kinematics

Summary. *Human motor control studies using functional magnetic resonance imaging give rise to many challenges. One of them is the design of haptic interfaces that are compatible with the magnetic field. To achieve this, the existing haptic interfaces mostly employ a parallel kinematics. However, they are limited in terms of Degrees of Freedom (DoF). When trying to offer more than three DoF without floating actuators, parallel kinematics often suffer from direct kinematic singularities and thus, strong mechanical anisotropy. In this chapter we determine an optimal six DoF kinematics that overcomes these limitations. To this end, we use performance indices such as singularity occurrence, worst-case output capabilities, sensitivity, and the global isotropy index. The resulting Octopod kinematics avoids a range of direct kinematic singularities by design. Finally, we present and evaluate a non-magnetic-resonance-compatible prototype of this novel type of kinematics.*

3.1 Problem statement and approach

Parallel kinematics have been employed as haptic interfaces to carry out human motor control studies using functional Magnetic Resonance Imaging (fMRI) [19, 20, 59]. Due to their non-floating actuators, they are less likely to cause image artifacts than serial kinematics. Moreover, they provide a high stiffness, a small inertia as well as a high force bandwidth. However, for more than three DoF, parallel kinematics are likely to be subject to both direct and inverse kinematic singularities. Direct kinematic singularities result in the gain of an uncontrollable DoF, while inverse kinematic singularities lead to the loss of one DoF [27]. If these singularities occur inside the desired workspace, they render the parallel kinematics unusable as haptic interfaces. In this chapter, we focus on designing a kinematics with six DoF.

In literature a range of kinematics have been proposed. Klare et al. [19] has adopted the well-known Delta kinematics for the design of an MR-compatible haptic interface. This type of kinematics provides three translational DoF and is not subject to direct kinematic singularities. However, the operator has restricted natural motions, since he cannot rotate the end effector. Pierrot [60] showed that the HEXA, which uses a fully-parallel kinematics, is a straight-forward extension to the Delta robot providing six DoF. Criteria for his design were maintaining non-floating rotational actuators, high dynamic capabilities with six DoF, and simplicity. The HEXA has six identical legs, each one actuated by a rotary actuator and composed of two spherical joints. These so called $\underline{R}$SS legs are arranged in pairs. When each pair moves simultaneously, the HEXA operates like the Delta only in three translational DoF. Due to the benefits of this type of kinematics with six DoF, a range of variants have been used as prototypical haptic interfaces in [61–63]. However, direct kinematic singularities occur and restrict the workspace.

Commercial haptic interfaces, on the other hand, increase the singularity-free workspace of kinematics with six DoF by employing hybrid parallel-serial architectures: For example the omega.6 or sigma.7 from Force Dimension are based on Delta kinematics with three translational DoF. Actuators at the end effector are in series with the Delta kinematics and add three rotational DoF. This comes at the cost of reduced output capabilities and increased inertia [64]. Moreover, MR-compatibility issues are likely to arise since floating actuators are employed.

In this work, we propose a parallel kinematics that provides six DoF, avoids singularities by design and does not employ floating actuators. The kinematics is driven by rotary actuators such that it can be built using MR-compatible USMs. Thus, the main contribution of this work is a novel Octopod kinematics that is systematically developed by comparing existing Hexapods based on quantitative performance criteria. These criteria include singularity occurrence, isotropy, sensitivity as well as worst-case output capabilities. To this end, also a comprehensive algorithm to determine maximum sensitivity and worst-case output capabilities of actuation-redundant parallel kinematics is introduced. Finally, the kinematics is realized as a non-MR-compatible prototype. This allows the study of the kinematics independently from position control issues of USMs.

The remainder of this chapter is structured as follows: Section 3.2 specifies the design criteria and presents the selection procedure for the haptic interface. The kinematics selection and design optimization are described in Section 3.3. The results are discussed in Section 3.4 and conclusions are stated in Section 3.5.

3.2 Design criteria and procedure, and performance indices

This section presents the design criteria that should be met by the kinematics. It also outlines the procedure to fulfill these criteria. Moreover, the performance indices that were applied within the procedure are introduced.

3.2.1 Design criteria

The goal of this work is to develop a haptic interface that fulfills the following design criteria:

- Six actuated DoF that enable the operator to perform natural, unconstrained movements: $d = 6$.

- Rotary, non-floating actuators directly at the joints that allow obtaining a parallel kinematics that can be built using USMs. Hence, only the first joint of each leg should be actuated and the number of legs L has to be at least as big as the number of DoF: $L \geq d$.

- The minimum output capabilities should be 1 m/s for the translational velocity and 9.81 $\mathrm{m/s^2}$ for the translational acceleration to provide a natural feeling as specified by Fisher et al. [24].

- The dexterous workspace should be free of singularities, have a minimum volume of 150 mm × 150 mm × 150 mm and provide ±30° of rotational DoF around all axes of the end effector [24]. This allows natural reaching motions including arm transport.
- The mechanical isotropy should be optimized to render a virtual environment with the same fidelity in the entire workspace.
- The maximum sensitivity of the device should be quantifiable in terms of force, torque, position, and orientation, in order to estimate worst-case error amplification.

3.2.2 Adopted procedure for kinematic selection and design optimization

In order to meet our design criteria, the kinematics is selected and optimized using the following four step procedure.

In the first step, existing fully-parallel kinematics with rotary actuators are selected. Then, a parametrized description of these kinematics is defined to be able to compare them systematically.

In the second step, we determine a kinematics among the existing configurations that is optimal regarding our design criteria quantified by means of performance indices. Several indices have been introduced to determine the kinematic and dynamic performance of parallel manipulators as well as haptic interfaces [61, 65–68]. Here, we focus on performance indices that allow meeting our design criteria: Worst-case output capabilities to guarantee required minimum output capabilities, singularity occurrence to avoid singularities within the dexterous workspace as well as the Global Isotropy Index (GII) [65] to provide mechanical isotropy. Moreover, the sensitivity is evaluated in order to quantify maximum error amplification. Finally, the size of the dexterous workspace is calculated such that it guarantees the minimum required volume.

In the third step, the optimal kinematics resulting from the selection is enhanced systematically. Kinematic or actuation redundancy can be employed to further reduce singularity occurrence [27]. This also enhances isotropy as well as output capabilities as will be shown in this chapter. Redundancy can also be employed to provide additional DoF, e.g. for grasping [69]. Kinematic redundancy means that at least one linkage is a motion generator of more DoF than necessary. Actuation redundancy means that the number of DoF is overconstrained by the number of actuators and is again split up in two classes: In-branch redundancy, where at least one leg has more actuated DoF than necessary; and branch redundancy, where the end effector is overconstrained by at least one kinematic chain. In-branch redundancy requires floating actuators or has to be realized via linkages from additional motors to the joints that should be actuated. This results in quasi-in-branch redundant kinematics [63], but requires complex kinematic chains. Here, we suggest a branch-redundant solution. It enlarges the singularity-free workspace and maintains the simplicity of the non-redundant kinematics. An additional pair of legs overconstrains the end effector of a Hexapod and results in an Octopod configuration.

In the fourth and final step, a mechatronic prototype of the kinematics is realized. To achieve the desired performance, also backlash, friction and mass have to be minimized, which is done during the mechanical design process of this work. The prototype is then employed to validate the kinematics.

3.2.3 Performance indices

The performance indices employed in this work and used for selection as well as optimization of the kinematics mostly rely on the Jacobian matrix. For parallel manipulators, the Jacobian is often decomposed and yields the relation between actuator velocities $\dot{\mathbf{q}}$ and output velocities $\dot{\mathbf{x}}$ as

$$\mathbf{J_q}\dot{\mathbf{q}} = \mathbf{J_x}\dot{\mathbf{x}}. \tag{3.1}$$

Here, $\mathbf{J_q}$ is a square $L \times L$ matrix and $\mathbf{J_x}$ is a $L \times d$ matrix, where d is the number of DoF of the device and L is the number of legs and actuators. $\mathbf{J_x}$ is square for non-redundant actuation. The Jacobian for parallel manipulators is then typically expressed as

$$\mathbf{J} = \mathbf{J}_q^{-1}\mathbf{J}_x \tag{3.2}$$

and the force/torque output capabilities are denoted by

$$\mathbf{f} = \mathbf{J}^T\boldsymbol{\tau}. \tag{3.3}$$

This establishes the relation between the actuator torques $\boldsymbol{\tau}$ and the end effector wrench $\mathbf{f}$. Note that this definition is different from serial manipulators. The Jacobian can be employed to measure closeness to singularities [70], isotropy [65] as well as output capabilities of the device such as forces, torques or velocities [71].

Kinematic singularities

The major problem of parallel kinematics with more than three DoF are kinematic singularities. In many applications singularity-free trajectories are computed for the end effector. But in case of a haptic interface, the operator can drive the kinematics into a singular configuration. Mathematically, inverse kinematic singularities occur when $\mathbf{J_q}$ drops rank, while direct kinematic singularities are present when $\mathbf{J_x}$ drops rank. Typical inverse kinematics singularities are found at the border of the workspace and thus, can be avoided by restricting the workspace. However, this does not guarantee avoiding all singularities of this type. Direct kinematic singularities result in the gain of an uncontrollable DoF and are often found within the workspace. In this paper, we use the word ‘singularity’ to refer exclusively to direct kinematic singularities.

Singularity occurrence can be explained geometrically using Grassman geometry [72]. The closeness to singularities can be measured by singular values of $\mathbf{J_x}$ or $\mathbf{J}$ respectively [70]. This is computationally easier than computing geometric configurations leading to a singularity. However, the workspace has to be sampled very precisely during the design phase to detect as many singular configurations as possible. Methods like the interval-based analysis [73] circumvent this issue by using branch-and-prune algorithms. In this study, we employ the CuikSuite toolbox [74] to detect singularities. The toolbox uses a branch-and-bound algorithm and is geared towards singularity detection in closed kinematic chains. Still, we would like to emphasize that this is not a formal proof since any numerical software tool has tolerances, which have to be taken into account.

Isotropy

The Jacobian can also be employed as a measure of isotropy or manipulability. Mechanical isotropy provides homogeneous output capabilities in the entire workspace. It facilitates actuator choices as well as controller design. Global isotropy makes it possible to render physical contacts with the same fidelity at every point in the workspace for every end effector pose. Manipulability or isotropy are determined locally by the condition number κ, which is given by

$$\kappa = \frac{\sigma_{min}}{\sigma_{max}}, \tag{3.4}$$

where σ_{min} and σ_{max} are the minimum and maximum singular values in a specific pose. This index is expanded to the entire workspace by applying the Global Isotropy Index (GII). The GII characterizes global mechanical isotropy of a kinematics and has been introduced by Stocco et al. [65]. It describes the ratio of minimum and maximum singular values of the Jacobian, σ_{min} and σ_{max}, in the entire workspace. This index is bounded between zero and one. A GII of one represents a kinematics that is perfectly isotropic with the same output capabilities in every pose. A GII close to zero stands for a kinematics that has at least one singular configuration within its workspace. Here, a GII optimization, using the culling algorithm [65], is applied to determine the kinematics with the best isotropy from a parametrized description of the known manipulators, as depicted in Figure 3.2. This allows the determination of the kinematics with best isotropy, given a certain parametrization, even if it is a hybrid solution of the known kinematics. To account for non-homogeneous physical units in the Jacobian, a scaling matrix as proposed by Stocco et al. [75] is employed.

Worst-case output capabilities

Hayward [68] suggests to identify, besides other criteria, the best and the worst-case output capabilities of haptic interfaces. They encompass force, torque, velocity, and acceleration. This allows us to determine if a kinematics can achieve the desired minimum velocity and acceleration capabilities. Ueberle [71] introduced an algorithm to evaluate the worst-case output capabilities of non-redundant manipulators. Here, we propose an extension to the case of actuation-redundant kinematics. This is required, when analyzing the proposed Octopod kinematics. First of all, the equations of the output capabilities of a parallel manipulator are given by

$$\dot{\mathbf{x}} = \mathbf{J}^{\#}\dot{\mathbf{q}}, \tag{3.5}$$

$$\mathbf{f} = \mathbf{J}^{T}\boldsymbol{\tau};\ \ \dot{\mathbf{q}} = \mathbf{0}, \tag{3.6}$$

$$\ddot{\mathbf{x}} = \mathbf{J}^{\#}\mathbf{M}_q(\mathbf{q})^{-1}\boldsymbol{\tau};\ \ \dot{\mathbf{q}}, \mathbf{f} = \mathbf{0}, \tag{3.7}$$

where $\mathbf{J}^{\#}$ is the generalized Moore-Penrose pseudoinverse, defined as $\mathbf{J}^{\#} = (\mathbf{J}^T\mathbf{J})^{-1}\mathbf{J}^T$. These equations relate actuator capabilities, such as velocities $\dot{\mathbf{q}}$ and torques $\boldsymbol{\tau}$, to end effector capabilities, namely its velocities $\dot{\mathbf{x}}$, its wrench $\mathbf{f}$, and its accelerations $\ddot{\mathbf{x}}$. The relations build on the Jacobian $\mathbf{J}$ and the mass matrix in joint space $\mathbf{M}_q(\mathbf{q})$. All relations can be generally written as

$$\begin{pmatrix} \mathbf{u}_{trans} \\ \mathbf{u}_{rot} \end{pmatrix} = \begin{pmatrix} \hat{\mathbf{J}}_{trans} \\ \hat{\mathbf{J}}_{rot} \end{pmatrix} \mathbf{p}, \tag{3.8}$$

where $\hat{\mathbf{J}}_{trans}$ and $\hat{\mathbf{J}}_{rot}$ are the submatrices denoting the translational and the rotational part of $\hat{\mathbf{J}}$. The actuator torques and velocities are expressed by $\mathbf{p}$ and the output capabilities by $\mathbf{u}_{trans}$ as well as $\mathbf{u}_{rot}$. The worst-case output capabilities are then formulated as the minimax optimization problem

$$\min_{\mathbf{d}} \max_{\alpha>0} ||\hat{\mathbf{J}}\alpha\mathbf{d}|| \text{ such that } \alpha\mathbf{d} \in [\mathbf{p}_{min}, \mathbf{p}_{max}], \tag{3.9}$$

where $||\cdot||$ denotes the L_2 norm and $\mathbf{p}_{min}$ and $\mathbf{p}_{max}$ are the minimum and maximum output capabilities of the actuators. Ueberle [71] shows that the problem can be converted into six linear least squares problems for the non-redundant case, $L = d$. This holds true in this situation since the minimum of the maximum achievable outputs of the end effector are found on hyperplanes, each one defined by at least one saturated actuator i, such that

$$\min_i \{\min_{\mathbf{p}_i} \mathbf{F}_i^T \mathbf{F}_i\}, \tag{3.10}$$

$$\mathbf{F}_i = \hat{\mathbf{J}}_i \mathbf{p}_i + \hat{\mathbf{j}}_i \overline{p}_i, \tag{3.11}$$

where $\hat{\mathbf{J}}_i$ is obtained by deleting the i-th column $\hat{\mathbf{j}}_i$ of $\hat{\mathbf{J}}$, and $\overline{p}_i$ is p_{min} or p_{max}. Additional constraints such as

$$\min_i \{\min_{\mathbf{p}_i} \mathbf{F}_i^T \mathbf{F}_i\} \text{ such that } \hat{\mathbf{J}}_{rot,i} \mathbf{p}_i + \hat{\mathbf{j}}_{rot,i} \overline{p}_i = 0 \tag{3.12}$$

can be included in a straight forward manner [71]. Here, $\hat{\mathbf{j}}_i$ is the i-th column of the Jacobian matrix and $\overline{p}_i$ is the maximum output of the i-th actuator in terms of torque or velocity. This allows evaluating the worst-case output capabilities, e.g. for pure force at zero torque output. However, in case of actuation-redundant kinematics, the minimax optimization problem (3.9) cannot be converted into a linear least squares problem. The additional actuators lead to infinite many solutions of (3.10), (3.11) with a minimum output capability of zero.

In this work, we present an algorithm that allows obtaining the worst-case output capabilities of actuation-redundant kinematics. In case of non-redundant kinematics, it yields the same results as (3.10), (3.11). To this end, we combine the work by Ueberle [71] with another approach by Krut et al. [76], who introduced an algorithm that computes a wrench polytope in task space, in order to find the 'maximum operational isotropic force'. The polytope in task space can be determined for both redundant and non-redundant kinematics, since each of its vertices is defined by all actuators saturating at their minimum or maximum output capability $\overline{p}_{min}$ or $\overline{p}_{max}$, respectively. Hence, all vertices and thus, all hyperplanes that constitute the polytope can be computed. The shortest distance form the origin to the surface of the polytope in task space then constitutes the worst-case output capabilities. Krut et al. [76] determined the worst-case wrench. In addition, we also compute worst-case velocities or accelerations by considering the equations used by Ueberle [71] (3.5)-(3.7). Also, additional constraints as in (3.12) such that pure translational or rotational outputs can be evaluated, are added to our computation. This yields an algorithm with four steps, which we call the ‘polytope algorithm’ here. The algorithm requires the generalized Jacobian $\hat{\mathbf{J}}$ as well as the maximum actuator output capabilities in terms of velocity, force, and resolution $\overline{p}_i$ as inputs. The output of the algorithm are minimum and maximum $||\mathbf{u}_{min,max}||$ achievable capabilities in terms of force, torque, velocity, acceleration, and sensitivity at the end effector. An example in three DoF is depicted in Figure 3.1.

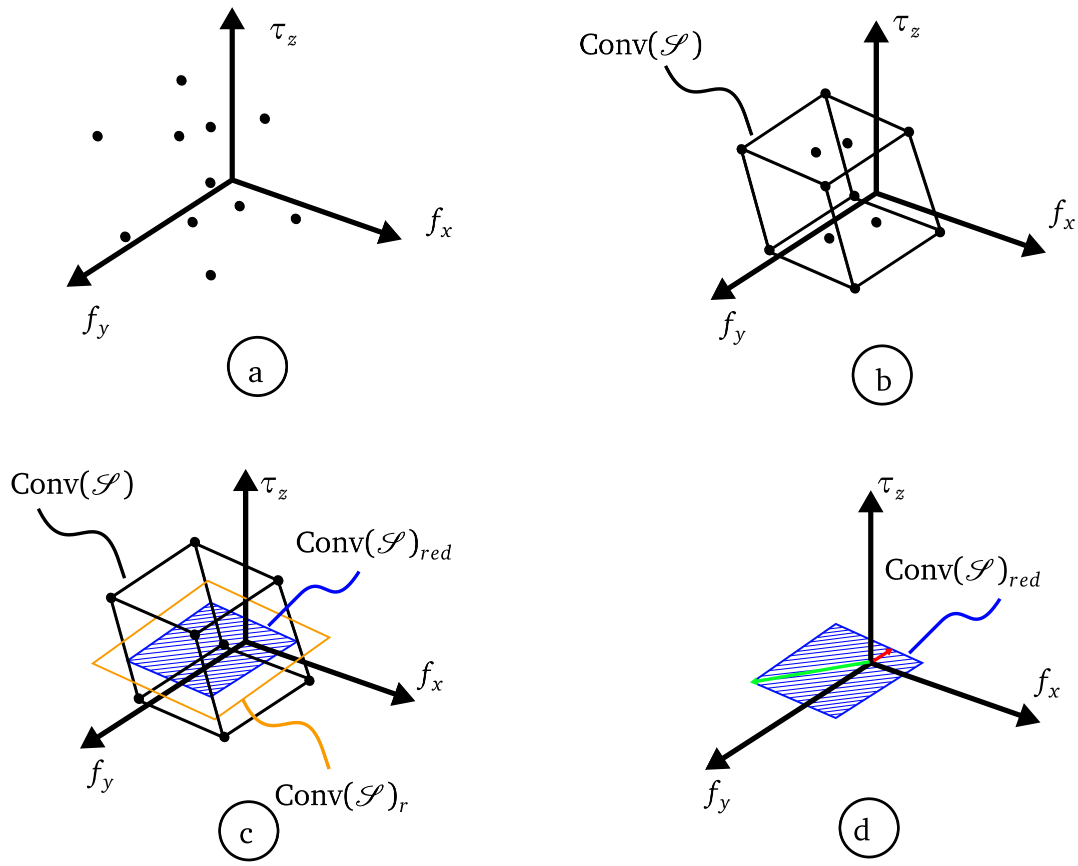

Figure 3.1: The four steps a)-d) of the ‘polytope algorithm’ with an example in three DoF.

The reduction to three DoF is carried out in order to visualize the results, but all steps also apply to kinematics with more DoF. The algorithm proceeds as follows:

Finding all vertices of the wrench, velocity, and acceleration polytope: First of all, the vertices of the wrench, velocity, and acceleration polytope are computed. To this end, (3.8) is evaluated with all 2^L binary combinations of the elements of $\mathbf{p} = [\overline{p}_1 \dots \overline{p}_i]^T$, where $\mathbf{p}$ is $L \times 1$ and $\overline{p}_i$ is p_{min} or p_{max}. The result is a set $\mathscr{S}$ containing the output capability vertices $\mathbf{u}_{vertex,j}$ with $j \in 1...2^L$. An example, with a two dimensional force and a one dimensional torque output, is depicted in Figure 3.1a).

Determining the convex hull of the polytope: The convex hull of the polytope in $\mathbb{R}^d$ is described as

$$\mathrm{Conv}(\mathscr{S}) = \left\{ \sum_{j=1}^{2^L} \alpha_j \mathbf{u}_{vertex,j} | (\forall j : \alpha_j \geq 0) \wedge \sum_{j=1}^{2^L} \alpha_j = 1 \right\}. \tag{3.13}$$

Readily available algorithms such as quickhull are embedded in the MATLAB environment, such that (3.13) can be solved. The result for our example with $d = 3$ is depicted in Figure 3.1b), yielding a cuboid hull.

Slicing the polytope along the dimensions that should be evaluated: If only output capabilities along r DoF of the end effector should be evaluated, e.g. only force at zero torque output, the polytope is sliced along the DoF of interest. The result is a reduced convex hull $\mathrm{Conv}(\mathscr{S})_{red}$ in $\mathbb{R}^r$, with $0 < r < d$ that is obtained via

$$\mathrm{Conv}(\mathscr{S})_{red} = \mathrm{Conv}(\mathscr{S}) \cap \mathrm{Conv}(\mathscr{S})_r, \tag{3.14}$$

where $\mathrm{Conv}(\mathscr{S})_r \in \mathbb{R}^r$ is infinitely large. In the example depicted in Figure 3.1c), the polytope is sliced along the xy plane, such that $r = 2$. The result is the shaded blue area, in order to evaluate pure force at zero torque output.

Computing the minimum distance from the origin to the surface of the polytope: In the final step, the minimum distance from the origin $\mathbf{x}_0$ to the surface of the reduced convex hull $\mathrm{Conv}(\mathscr{S})_{red}$ is computed. In Figure 3.1d) this is indicated by a red arrow. Using the minimum distance

$$||\mathbf{u}_{min}|| = \min_{\mathbf{c} \in \mathrm{Conv}(S)_{red}} ||\mathbf{c} - \mathbf{x}_0||, \tag{3.15}$$

worst-case output capabilities are quantified.

Maximum sensitivities

Maximum point-displacement and rotation sensitivity has been introduced by Cardou et al. [77] and can also be determined with the 'polytope algorithm'. This requires using (3.5) and considering $\dot{\mathbf{q}}$ as normalized actuator displacements, such that $||\dot{\mathbf{q}}||_\infty = ||\mathbf{J}\mathbf{x}||_\infty = 1$ rad. Force and torque sensitivities are determined analogously using (3.6) and $||\mathbf{f}||_\infty = ||\mathbf{J}^T\boldsymbol{\tau}||_\infty = 1$ Nm. This means the actuator output capabilities are normalized to $\overline{p}_i = \pm 1$ rad and $\overline{p}_i = \pm 1$ Nm. The algorithm is carried out similarly and in its last step, with the maximum distance

$$||\mathbf{u}_{max}|| = \max_{\mathbf{c} \in \mathrm{Conv}(S)_{red}} ||\mathbf{c} - \mathbf{x}_0||, \tag{3.16}$$

maximum sensitivities are quantified. In Figure 3.1d) this is indicated by a green arrow.

Dexterous workspace

Improved output capabilities can be achieved at the cost of a reduced dexterous workspace: The workspace could be reduced to a small entity with optimal output capabilities. Hence, the dexterous workspace should be taken into account as a performance index. It denotes the volume V in which the end effector can achieve orientations within a specified range [27] and minimum output capabilities can be provided such that

$$\forall \mathbf{x} \in V : |\dot{\mathbf{x}}(\mathbf{x})| \geq \dot{x}_{min}, |\ddot{\mathbf{x}}(\mathbf{x})| \geq \ddot{x}_{min}, |\mathbf{f}(\mathbf{x})| \geq f_{min}. \tag{3.17}$$

Here, $\dot{x}_{min}$, $\ddot{x}_{min}$, and f_{min} denote the minimum required output capabilities in terms of velocity, acceleration and wrench, respectively. This workspace is computed from the inverse kinematics, where an over-approximation of the workspace is sampled. Then, only configurations, where the joint angles are real and in a valid range are retained.

3.3 Kinematics selection and design optimization

In the following section, we apply the performance indices within our proposed four step procedure. This allows us to obtain an optimal kinematics that meets our design criteria.

3.3.1 Step 1: Selection of fully-parallel kinematics with rotary actuators

In the first step, kinematics are selected for comparison. A wide range of parallel kinematics exists but here we focus on fully-parallel kinematics [60] with non-floating rotational actuators. This allows the conception of an MR-compatible device actuated by USMs. The $\underline{\text{R}}$SS kinematics meets these criteria and has been introduced by Hunt [78] already in 1983. Since the kinematics is simple and provides high dynamic capabilities [60], various variants [60–63] have been employed as haptic interfaces. In most cases, the original $\underline{\text{R}}$SS chains are reduced to $\underline{\text{R}}$US chains, by replacing one spherical joint with a universal joint, without the loss of DoFs at the end effector. Pierrot [60] showed that his 6-$\underline{\text{R}}$US variant, the HEXA, is a straight-forward extension to the singularity-free Delta kinematics.

Further variants generalize the $\underline{\text{R}}$US chain to an $\underline{\text{R}}$RRS chain as done by Ergin et al. [62]. These simplifications allow the use of rotary joints only and increase the workspace [62]. A general description of a 6-$\underline{\text{R}}$SS manipulator is depicted in Figure 3.2. Three parameters make the difference between the Hunt-type kinematics, Ergin's device and the HEXA: angle β at the base, length l_2, and angle γ at the end effector. For the Hunt-type kinematics angles γ and β as well as l_2 are zero. In comparison, γ is non-zero for the HEXA. In case of Ergin's device both γ and β as well as l_2 are non-zero. Among the variants of the $\underline{\text{R}}$SS kinematics it remains unclear which one is an optimal haptic interface. Here, the HEXA [60], the iFeel6.0 [61] that implements the Hunt-type kinematics, and Ergin's device [62] were chosen for comparison.

3.3.2 Step 2: Determination of an optimal kinematics

In the second step, the selected kinematics were evaluated based on singularity occurrence, GII, worst-case output capabilities, maximum sensitivity, and dexterous workspace.

Singularities

The three selected kinematics were tested for singularity occurrence in the reachable workspace. Only translational displacements at zero rotational angles were considered for

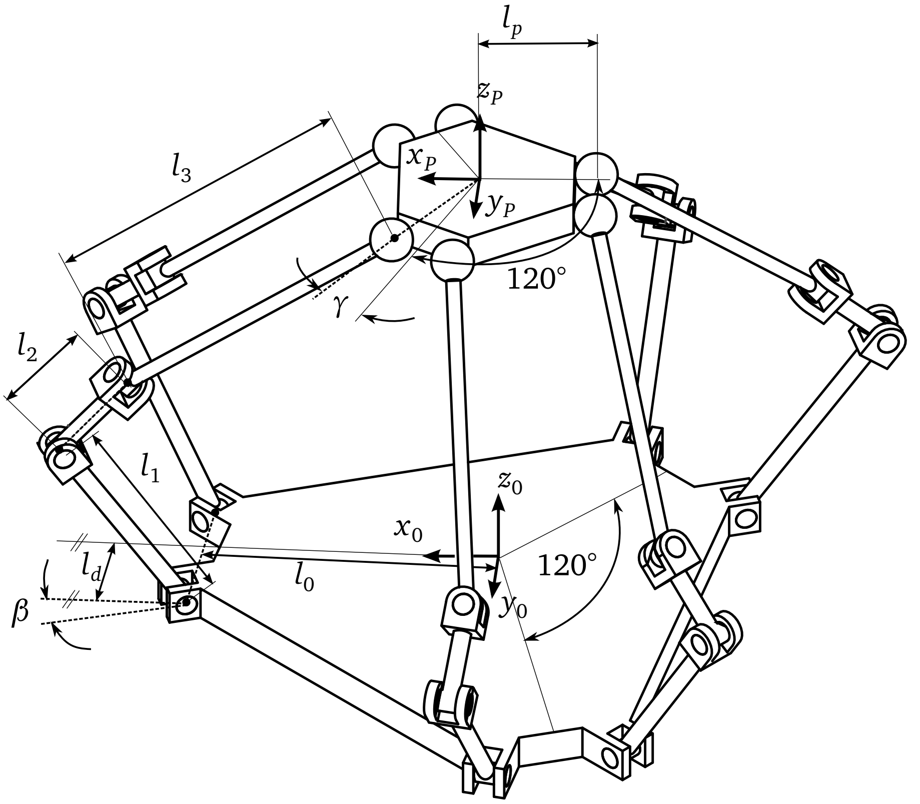

Figure 3.2: General description of an R̲SS Hexapod, generalized as an R̲RRS Hexapod.

illustration. Conditioning the end effector to zero rotations restricts the number of singularities that can be detected and has been done to maintain a reasonable computation time. Singularities were detected via the CuikSuite toolbox and the result is shown in Figure 3.3. The Hunt-type kinematics is free of singularities in the translational workspace, unlike Ergin's device or the HEXA. Ergin's device suffers from singularities within its entire workspace. Singularities of the HEXA occur in three distinct regions of the workspace.

Generally, singularities of Hexapods can be analyzed using Grassman geometry. Merlet has shown that singularities of parallel robots with at least six limbs occur when the lines along the limbs lie in one linear complex approximation (LCA) [72]. Two typical types of singularities of R̲SS Hexapods are depicted in Figure 3.4. Hunt's singularity occurs when the end effector is coplanar with two terminal links of the R̲SS legs [79]. All lines along the terminal links lie in one LCA around which an uncontrolled DoF occurs. In Fichter's singularity, the end effector describes an uncontrollable screw motion along the z_P axis that aligns with the LCA [79].

Isotropy

The isotropy of the known kinematics is compared via a GII optimization. Three parameters, as detailed earlier and depicted in Figure 3.2, determine the difference between Hunt-type kinematics, Ergin's device, and HEXA: Angle β at the base, length l_2, and angle γ at the end effector. Distance l_d was found to be another important parameter and was also considered

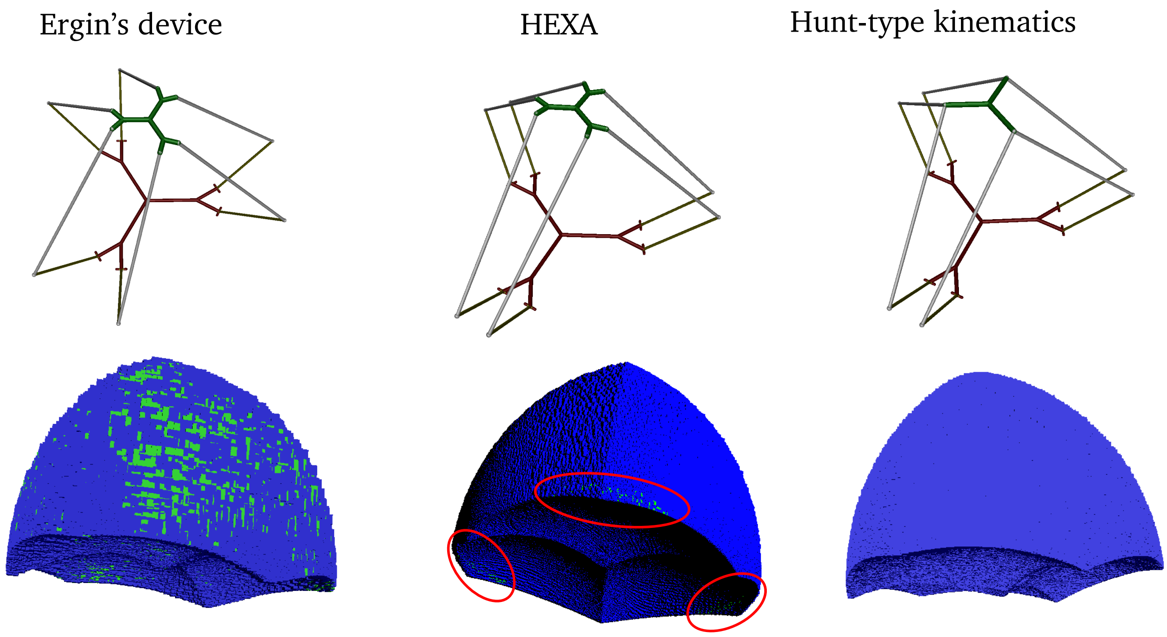

Figure 3.3: Results of CuikSuite calculations for Ergin's device, the HEXA, and the Hunt-type kinematics. The dexterous workspace with only translational displacements at zero rotations is depicted in blue and singularities are depicted in green.

during the optimization. The total length of each leg remains constant, which is ensured by keeping $l_2 + l_3$ constant. Baseline geometric characteristics were taken from Ergin's device [62]. The step sizes were chosen as 5 mm for l_2 and l_d, and as 10° for both β and γ. The resulting parameter space is summarized in Table 3.1. The step size was restricted such that it guarantees reasonable computation times. The optimization also allows hybrid solutions of the three kinematic structures. The parameters that remain constant are the length of the first link in each leg $l_1 = 157$ mm as well as the radius of the base $l_0 = 152$ mm and the end effector $l_p = 55$ mm. These parameters do not contribute to the structural difference between the three kinematics to be compared. The translational workspace is a cube of 150 mm edge length, sampled with a step size of 10 mm and an offset along the z_0 axis of 0.30 m, see Table 3.2. The rotations around each axis of the end effector are limited to ±20° with a step size of 5°. The maximum orientations of the end effector have been restricted to 20° for the optimization, since the kinematics fall into a perfect Hunt-type singularity for larger

Tabular 3.1: Parameter ranges of l_2, β, γ, and l_d for GII optimization.

Parameter	Min.	Max.	Step	Optimum
l_2	0 mm	30 mm	5 mm	0 mm
β	0°	30°	10°	0°
γ	0°	30°	10°	0°
l_d	20 mm	40 mm	5 mm	20 mm

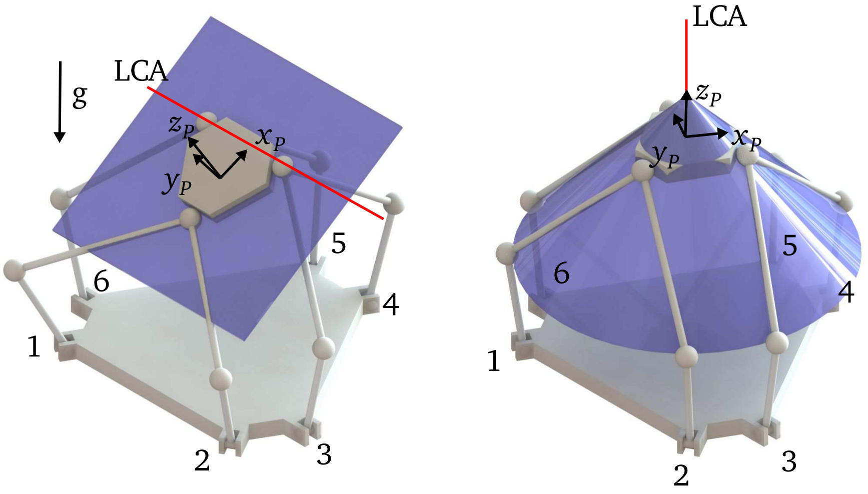

Hunt’s singularity Fichter’s singularity

Figure 3.4: Direct kinematic singularities that are present in the workspace of an $\underline{R}$SS Hexapod: Hunt’s singularity occurs when two terminal links are coplanar with the end effector and an uncontrollable DoF around the LCA is present. In Fichter’s singularity, the end effector describes an uncontrollable screw motion along the z_P axis that aligns with the LCA.

orientations within the desired dexterous workspace and hence, the minimum singular value σ_{min} depends only on the numerical precision and the GII is meaningless.

Tabular 3.2: Cuboid workspace for GII optimization centered at $z_0 = 0.30$ m.

Translational workspace			
Axis	Min.	Max.	Step
x	-75 mm	75 mm	10 mm
y	-75 mm	75 mm	10 mm
z	-75 mm	75 mm	10 mm
Rotational workspace			
Axis	Min.	Max.	Step
x	-20°	20°	5°
y	-20°	20°	5°
z	-20°	20°	5°

The optimization was computed using the culling algorithm [65]. The scaling matrix S_T [75] was set to $S_T = diag[15\text{N} \quad 15\text{N} \quad 15\text{N} \quad 1\text{Nm} \quad 1\text{Nm} \quad 1\text{Nm}]$ to account for non-homogeneous physical units in the Jacobian. The scaling matrix is also a design choice and contains the desired magnitude of the end effector wrench. The quantities were chosen as the originally intended output capabilities for Ergin’s device [62].

The optimum for the GII was found for $l_2 = 0$ mm, $\beta = 0°$, $\gamma = 0°$, and $d = 20$ mm. Here, the GII is 0.0006 with $\sigma_{min} = 0.0127$ and $\sigma_{max} = 20.0052$. Hence, regarding the GII in the

Tabular 3.3: Minimum and maximum of the worst-case output capabilities as well as maximum sensitivities in the workspace listed in Table 3.2 with rotations of ±20° around all axes. The Octopod kinematics and the realized Octo have additionally been evaluated in the same workspace with rotations up to ±30° around all axes, while maintaining steps of 5°.

Output capability	Kinematics and min. (max.) value				
	Ergin's device	HEXA	Hunt-type	Octopod (Rot. ±30°)	Octo (Rot. ±30°)
Continuous force/N	0.00 (12.72)	0.57 (26.25)	1.89 (40.16)	21.68 (63.19)	16.02 (44.11)
Continuous torque/Nm	0.00 (0.59)	0.03 (1.17)	0.05 (1.75)	0.86 (2.80)	0.75 (2.14)
Velocity/(m/s)	2.78 (7.85)	2.78 (8.01)	2.86 (7.98)	2.74 (10.06)	2.93 (10.18)
Angular velocity/(rad/s)	67.99 (182.63)	69.06 (175.17)	64.57 (150.46)	75.57 (214.71)	84.44 (225.28)
Acceleration/(m/s^2)	0.00 (1023.37)	45.78 (2112.64)	152.02 (3231.29)	1744.46 (5085.15)	1289.19 (3631.16)
Angular Acceleration/(10^{3}rad/s^2)	0.00 (26.79)	1.24 (53.51)	2.38 (79.65)	39.38 (125.63)	34.34 (100.65)
Max. translational sensitivity/(m/rad)	0.16 (0.31)	0.18 (0.38)	0.18 (0.34)	0.17 (0.32)	0.17 (0.34)
Max. rotational sensitivity/(rad/rad)	4.56 (14.83)	3.68 (9.22)	3.67 (6.13)	2.93 (6.35)	3.58 (8.18)
Max. force sensitivity/(N/Nm)	11.96 (38.15)	16.37 (35.37)	19.08 (32.64)	22.34 (43.83)	18.08 (43.88)
Max. torque sensitivity/(Nm/Nm)	0.36 (0.87)	0.62 (1.25)	1.12 (2.18)	1.04 (2.41)	0.77 (1.78)

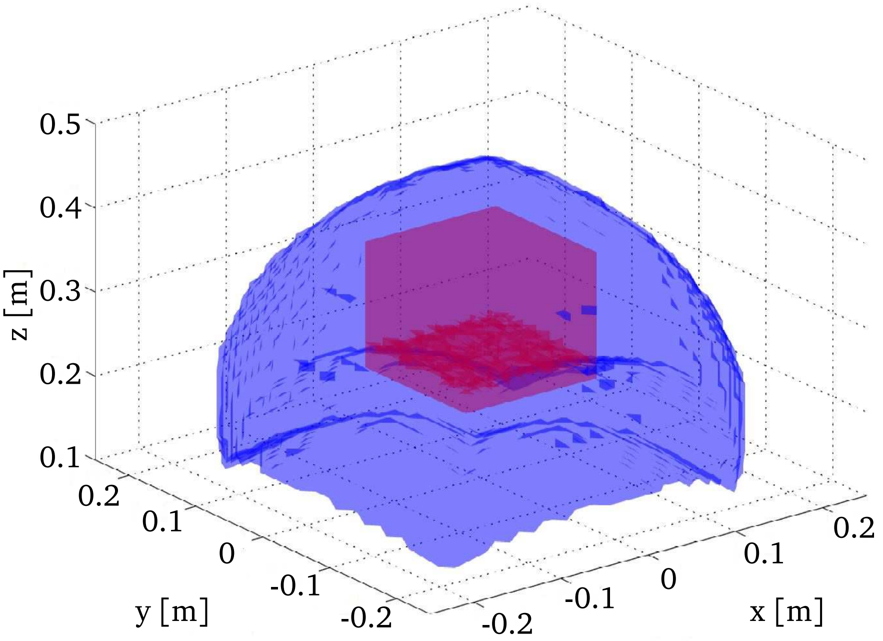

Figure 3.5: Dexterous workspace, depicted with only translational displacements of the Octopod kinematics in blue and desired workspace volume, where ±20° rotations around all axes are achievable, in red.

chosen parameter space and workspace, the Hunt-type kinematics, with a minimum distance l_d, was found to be the optimal configuration among the 6-$\underline{\text{R}}$SS kinematics that were studied.

Workspace, worst-case output capabilities, and sensitivities

Besides singularity avoidance, the criteria of output capabilities within the desired dexterous workspace have to be met. The workspace should have a volume of 150 mm × 150 mm × 150 mm, where rotations of ±30° around all axes are achievable. The volume of the workspace is depicted as a red cube in Figure 4.11. The worst-case output capabilities are analyzed for the selected kinematics. The kinematics are evaluated within the desired workspace volume with rotations restricted to ±20° around all axes to avoid Hunt-type singularities. To evaluate the output capabilities and sensitivities, the algorithm by Ueberle [71] and the 'polytope algorithm' in case of an actuation-redundant device are applied, respectively. The actuators, as used by Ergin et al. [62], produce a nominal torque of $\tau_{i,max,n} = \pm 2.5$ Nm, a stall torque of $\tau_{i,max,st} = \pm 34.2$ Nm, and a nominal velocity of $v_{i,max} = \pm 51$ rad/s after gearing. The Cartesian mass matrix is approximated as $\hat{\mathbf{M}} = diag[m \quad m \quad m \quad I_x \quad I_y \quad I_z]$ with $m = 0.17$ kg, $I_{x,y,z} = 3 \times 10^{-4}$ kgm^2, and the similarity transformation to joint coordinates $\mathbf{M}_q(q) = \mathbf{J}(\mathbf{q})^T \hat{\mathbf{M}} \mathbf{J}(\mathbf{q})$. The minima and maxima of the worst-case output capabilities as well as the maximum sensitivities of all kinematics within the desired workspace and under rotations around all axes, are listed in Table 3.3. Here, the Hunt-type kinematics shows the best maximum performance among the non-redundant kinematics in terms of worst-case output capabilities. Interestingly, it is not systematically better

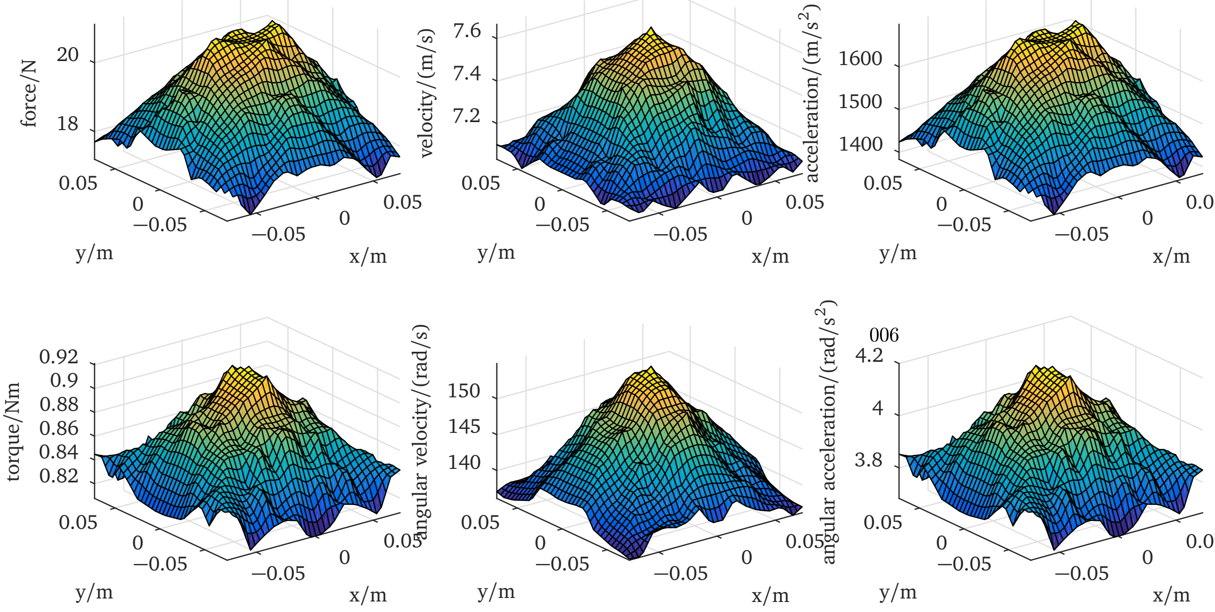

Figure 3.6: Worst-case output capabilities of the Octopod kinematics at $z = 0.30\ m$ with rotations of ±30° around all axes.

than the other kinematics regarding the maximum sensitivity that quantifies worst-case error amplification.

Tabular 3.4: GII optimization results.

Kinematics	GII	σ_{min}	σ_{max}
Hunt-type kinematics	0.0006	0.0127	20.0052
Octopod kinematics	0.0080	0.2230	27.8186
Octo kinematics	0.0072	0.1910	26.6404

3.3.3 Step 3: Redundant extension of the optimal kinematics

In the third step, we further enhance the best-performing kinematics, i.e. the Hunt-type kinematics. Of major concern are the rotations of the end effector that are restricted to ±20°. Even in this range, the minimum continuous torque is only 0.05 Nm, as presented in Table 3.3. Redundancy can be employed to improve upon this issue and further enhance all output capabilities. Here, we use branch redundancy, instead of in-branch redundancy or kinematics redundancy, in order to avoid floating actuators or high mechanical complexity due to complicated kinematic chains. Moreover, in order to keep the number of required actuators low, we add only one pair of legs. Finally, we would like the isotropy of the device to be unimpaired by this modification and thus, aim for a symmetric shape of the kinematics. Thus, we propose an extension of the Hunt-type kinematics to an Octopod kinematics with four symmetrical pairs of legs.

This should further decrease singularity occurrence, improve the GII as well as output capabilities. As shown in Table 3.4, the GII increases by a factor of 13 while the minimum singular value increases by a factor of 18. Hence, the Octopod will show more isotropic behavior than the Hunt-type kinematics and is less likely to be trapped in singular configurations. Note that redundant kinematics such as the Octopod cannot be analyzed using the CuikSuite toolbox.

The desired dexterous workspace can be covered by the Octopod kinematics and its entire translatory workspace is depicted in blue in Figure 4.11. The worst-case output capabilities of the redundant Octopod kinematics are evaluated using rotations of ±30° around all axes. They are computed by employing the proposed 'polytope algorithm'. The actuator performance and Cartesian mass matrix was adopted from Ergin's device [62]. The worst-case output capabilities of the Octopod kinematics in the plane of $z = 0.30$ m are depicted in Figure 3.6. This is the same plane that was used for the evaluation of Ergin's device [62].

A force polytope that results from the evaluation of the Octopod kinematics is depicted in Figure 3.7. The minimum force at zero torque is represented by a sphere inside the polytope that is tangential to the surface closest to the origin.

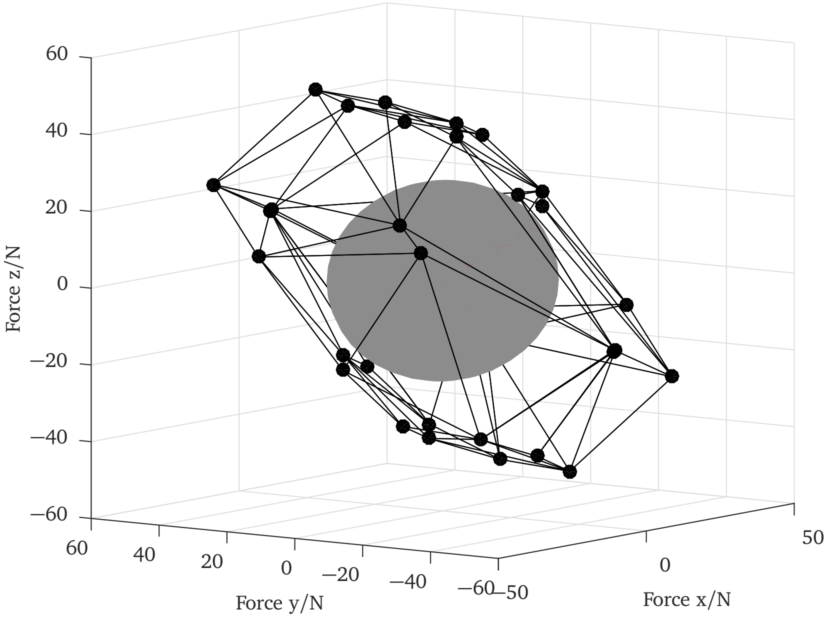

Figure 3.7: Plot of a force polytope that was computed for the evaluation of the Octopod kinematics. The continuous force is represented by a grey sphere that is tangential to one of the surfaces of the polytope.

The worst-case output capabilities of the Octopod kinematics within the desired workspace, are listed in Table 3.3. All non-redundant kinematics are outperformed by the Octopod kinematics in terms of minimum force, torque, and acceleration. The desired minima of acceleration and velocity can be achieved by the Octopod kinematics, also with rotations as high as ±30° around all axes. Moreover, the worst-case maximum sensitivities of the redundant kinematics are also listed in Table 3.3. The maximum force sensitivity increases, compared to the Hunt-type kinematics, whereas the other sensitivities show no significant change. The maximum torque sensitivity even decreases in the Octo kinematics.

Even though the performance of the Octopod kinematics improves in many respects, control challenges arise: First of all, the resolution of the pseudo-inverse is computationally intensive and restricts the maximum sampling time. Secondly, the redundancy generates internal tensions at the over-constrained end effector due to the geometric imperfections of a real system, measurement errors, or independent control of all actuators [80]. In order to address the issue of an over-constrained end effector, advanced control schemes have been proposed [80–82]. They augment standard PD or torque control in order to nullify internal forces [81], apply coordination motion control that takes into account parasitic forces due to tracking errors of neighboring kinematic chains [82], or propose a projection method for the elimination of contradicting decentralized control forces [80]. These advanced control methods were all evaluated using redundant parallel kinematics with two DoF. A thorough comparison of their performance with the MR-Octo offering six DoF is beyond the scope of this paper. However, we validated experimentally that the haptic interface can be controlled appropriately with a well-tuned PD controller. This means that internal forces exist, but they do not cause any vibration or other parasitic effects that impair the operation of the haptic interface. The implementation of this controller is presented in the following step.

3.3.4 Step 4: Hardware realization of the Octo kinematics

In the fourth and final step, a sub-optimal solution of the Octopod kinematics is implemented. It is based on Ergin's device [62] and depicted in Figure 4.10. Here, we refer to it as the 'Octo'. The Octo approximates the optimal parameter configuration in which angle γ and length l_2 have not been reduced to zero to facilitate manufacturing. The kinematic parameters were set to $l_2 = 25.6$ mm, $\beta = 0°$, $\gamma = 13.18°$, and $d = 20$ mm. To have sufficient space for the motors, the radius of the base has been increased to $l_0 = 160$ mm. The resulting worst-case output capabilities and GII are listed in Table 3.3 and Table 3.4, respectively.

Tabular 3.5: Experimental and simulative results of minimum worst-case output capabilities of the Octo.

Output capability	Experiment	Simulation
Continuous force/N	15.27	16.02
Continuous torque/Nm	0.68	0.75
Velocity/(m/s)	1.12	2.93
Angular velocity/(rad/s)	24.02	84.44
Acceleration/(m/s^2)	459.52	1289.19
Angular Acceleration/(rad/s^2)	7051.21	34341.13

The haptic interface is actuated by eight Maxon RE 40 DC motors. The motors are driven by Junus JSP-180-20 modules from Copley Controls, as depicted in Figure 4.3. The Capstan gears have a ratio of 1:13. The six DoF force/torque sensor at the end effector is a Mini27

Tabular 3.6: Comparison of the device capabilities to commercial haptic devices.

Output capability	Device (value)					
	Phantom Premium [83]	Maglev 200 [84]	Virtuose 6D [85]	Delta.6 [86]	Sigma.7 [87]	Octo
Continuous force/N	37.5	-	3	20	20	15.27
Continuous torque/Nm	0.17	-	0.2	0.15	0.4	0.68
Max. translations/m	0.381x0.267x0.191	Sphere 0.024	0.521x0.370x0.400	0.40x0.26	0.19x0.13	0.15x0.15x0.15
Max rotations/deg	297°x260°x335°	±8°	270°x120°x250°	±22°	235°x140°x200°	60°x60°x60°
Trans. stiffness/(N/mm)	3.5	0.002-50	≤1	-	-	1.6-7.9

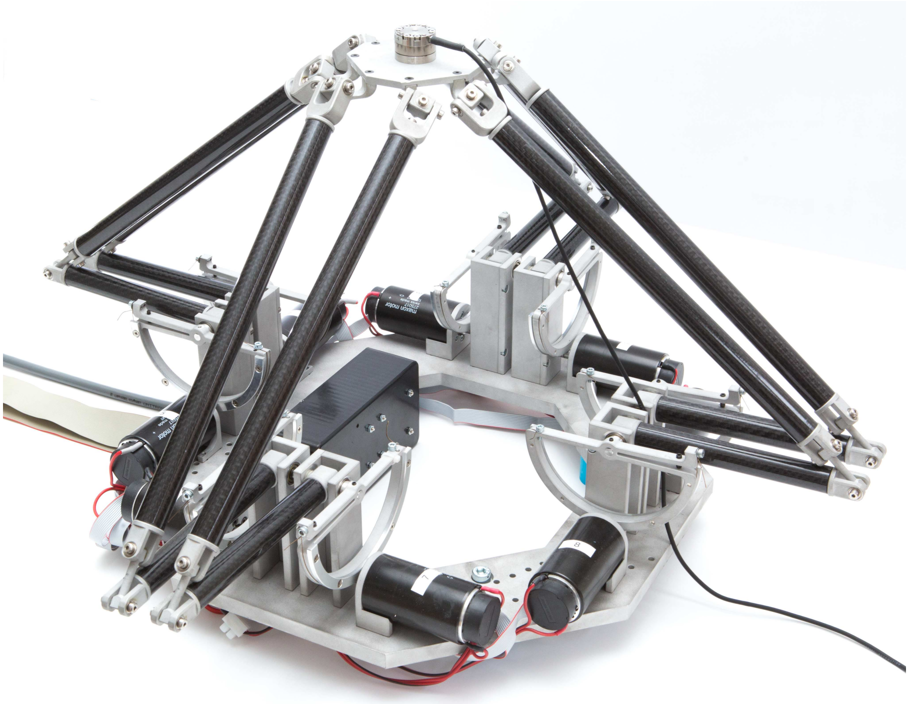

Figure 3.8: Photograph of the realized Octo.

Titanium from ATI IA. The commands for the motors are generated via MATLAB/Simulink and executed by a Linux real-time kernel at a sampling rate of 1 kHz. Initially, Matlab scripts and the Matlab/Simulink Simmechanics toolbox have been tested for the implementation of the forward and inverse kinematics, but finally we decided for MotionGenesis$^{\text{TM}}$ Kane to solve the inverse kinematics problem, since its routines and solver are optimized for real time applications. Inputs and outputs from the workstation to the haptic interface are managed via Mecovis I/O cards. The control of the haptic interface is governed by an admittance control scheme and the motors are controlled with a PD-controller at position level. This allows the control of the desired torque τ_{des} of the motors, based on their position $\mathbf{q}$ and the end effector wrench $\mathbf{F}$. For the experiments, the gains of the PID controller are set to $K_P = 110$, $K_I = 0$, and $K_D = 0.4$. The derivative of the error is additionally filtered with a low-pass filter using the forward Euler method with time constant 700 ms.

The prototype was employed to validate our design criteria. Firstly, the workspace was explored for singularity occurrence. Fichter's and Hunt's singularities are avoided within the dexterous workspace, as detailed in Table 3.2. Furthermore, the dexterous workspace of the Octo can be enlarged to cover orientations of up to 30° around all axes without the occurrence of singularities.

Secondly, the minima of the worst-case output capabilities were verified. The end effector was positioned in the poses of its worst-case output capabilities, as indicated by our theoretical analysis. Then, smoothed position step inputs were commanded in the respective directions. For each output capability five trials were executed and the mean was computed. Velocity and acceleration were not tested up to their maxima to avoid excessive wear on the structure. To validate worst-case forces and torques, the end effector was blocked. The recorded values are listed in Table 4.3 and they show that our design criteria are met.

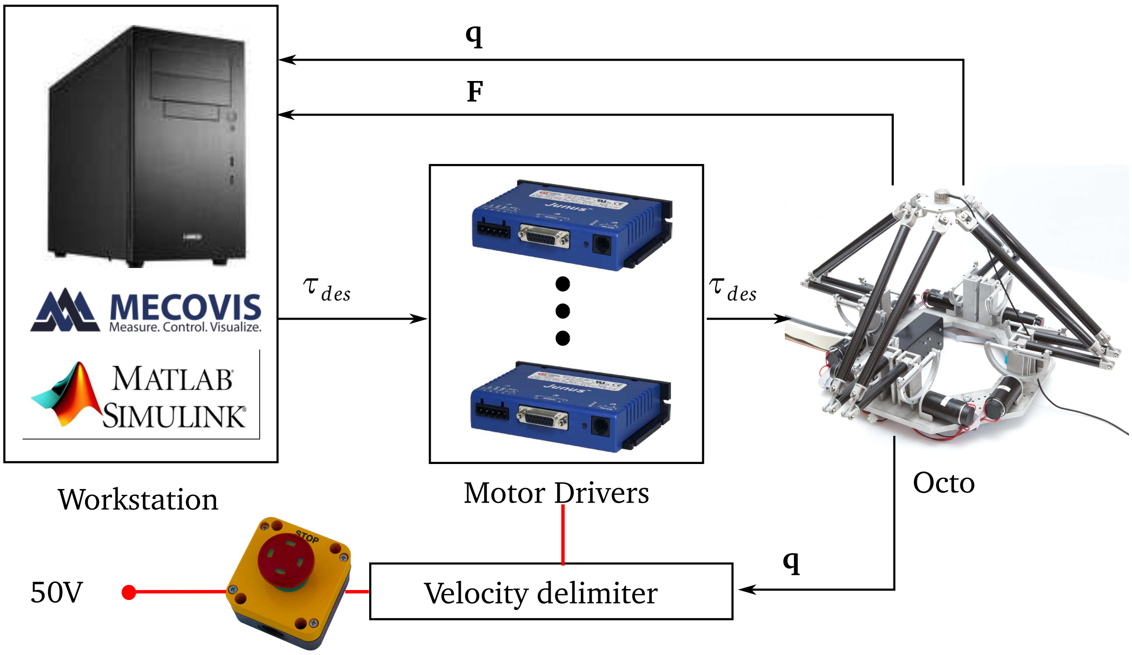

Figure 3.9: Hardware setup and signal flow between the Octo and the workstation.

Lastly, the stiffness of the prototype was determined. The end effector position was gauged with a dial indicator that measured displacements along the major axes. This experiment was performed in 27 positions at zero rotations in the dexterous workspace. The positions included the center, the corners, as well as the center of each facet and of each edge. The minimum, maximum, and mean stiffness were 1.6 N/mm along the x-axis, 7.9 N/mm along the z-axis, and 4.7 N/mm, respectively. The minima are found on the upper facet of the dexterous workspace at $z = 0.375$ m.

The experimental results are compared to commercial haptic interfaces in Table 3.6. It should be noted that the presented kinematics has been designed having its later application in an MR-compatible environment in mind. However, no MR-compatible haptic device that provides six DoF exists such that it could be taken as a reference. The kinematics chosen for comparison here cannot be rendered MR-compatible since either their main actuation principle cannot be changed to an MR-compatible one or they forsee actuators to be floating in space. Both would lead to motion artifacts in an MR scanner. Comparing the Octo to these devices, it is outperformed in terms of force capabilities by the Phantom Premium but its performance is comparable to the Delta.6 and Sigma.7. Moreover, the worst-case torque of the Octo lies above the torque of any other device considered for comparison. The workspace of the Octo is only larger than the one of the Maglev 200. The translational stiffness of the Octo is again comparable to the Phantom Premium and outperforms the other devices as far as their performance is known.

3.4 Discussion

In this study, we showed that the Hunt-type kinematics shows the best performance compared to the HEXA and Ergin's device, within the chosen workspace and in terms of singularity avoidance, achieving high isotropy as well as output capabilities. However, singularities remain when considering rotations among all axes. Thus, we suggested branch redundancy to reduce this problem. This also improved both output capabilities and isotropy. In order to calculate the worst-case output capabilities as well as maximum sensitivities, the 'polytope algorithm' has been applied. The computation of output capabilities was performed with a rotational resolution that guarantees reasonable computation times. This leads to a limited power to take conclusions on remaining singularities. Hence, the prototype has been employed to validate the absence of singularities and the worst-case output capabilities. An evaluation showed that it has a lower stiffness than commercial devices such as the omega.3 from Force Dimension, which features 14.5 N/mm. Apart from this, the results show a successful implementation of our design criteria. However, velocity and acceleration capabilities were calculated using a rigid body model that does not take into account practical limits resulting from the structural dynamics. Higher output capabilities could be achieved by a more rigid structure and a more advanced control scheme that reduces internal tensions in the over-constrained end effector.

3.5 Conclusion

In this study, we have introduced a novel Octopod kinematics. It has been derived from existing manipulators using a range of dynamic and kinematic performance criteria, such as GII, worst-case output capabilities, sensitivity, and singularity occurrence. Typical direct kinematic singularities of 6-$\underline{R}$SS manipulators are avoided with this type of kinematics. It outperforms known haptic interfaces with non-floating actuators and six DoF in terms of worst-case force, torque, and acceleration.

Future work needs to focus on performance improvement of this type of kinematics. A more advanced control scheme that reduces internal tensions in the over-constrained end effector will improve the practical output capabilities of the device. Moreover, an optimization that takes into account the worst-case output capabilities will most likely improve the performance. However, the computational demand for this kind of computation has to be taken into account.

In this work, we employ the Octopod kinematics as a basis for an MR-compatible haptic interface.

4 An MR-compatible Haptic Interface with Seven Degrees of Freedom for fMRI Studies

Summary. *In this chapter, a novel MR-compatible haptic interface with seven Degrees of Freedom (DoF) is presented. It allows both translations and rotations in three DoF each, as well as two finger precision grasps. The presented haptic interface is the first one with theses capabilities and is designed as a universal tool for human motor control studies involving fMRI. It allows switching the paradigm to reprogramming rather than redesigning when moving on to a new research question. Within this chapter, we present the entire system, assess its ergonomics and safety, and validate its compatibility with the magnetic field.*

4.1 Problem statement and approach

The primary challenge of this thesis is to develop a haptic interface that combines the capabilities of the existing MR-compatible haptic interfaces and thus, provides seven DoF along with bi-directional MR-compatibility. In Chapter 2 and Chapter 3 we laid the foundation for this novel device: First, we introduced a controller for USMs that should drive the haptic interface. This hybrid SMC copes with non-linearities, load-dependent dead zones and allows both high and low velocities. The ability to provide low velocities is essential, since those occur often in haptic applications. Second, we introduced a parallel kinematics with six DoF that avoids a range of direct kinematic singularities by design. Thus, all actuators remain stationary in order to avoid image artifacts.

In this chapter, we combine the findings from the previous chapters, namely control and kinematics, and augment the resulting system with a haptic gripper. This system is driven by nine USMs and allows haptic rendering in seven DoF, including translations, rotations and two finger pinch grasps. The components have been carefully selected and iteratively tested to ensure a low magnetic susceptibility. The haptic interface is extended with an MR-compatible support frame such that it is ergonomic, safe, and can be quickly deployed for fMRI studies. Moreover, a software interface to the open source haptic rendering software Chai3D allows the creation of a variety of task scenarios. In this chapter, we carry out experiments in order to validate the bi-directional MR-compatibility, such that neither image quality nor device performance is impaired by the magnetic field. Moreover, the safety and the ergonomics of the haptic interface are assessed, such that it can be applied for human motor control studies with subjects that are naive to the device.

The remainder of this chapter is structured as follows: Section 4.2 specifies the design requirements, whereas Sections 4.3 and 4.4 detail hardware design and haptic rendering of the realized prototype, respectively. Moroever, a human factors analysis that ensures a safe and ergonomic design is presented in Section 4.5. The applied performance indices to evaluate the design criteria and their experimental evaluation are presented in Section 4.6, whereas the MR-compatibility is validated in Section 4.7. Finally, the results are discussed and a conclusion is drawn in Sections 4.8 and 4.9, respectively.

4.2 Design requirements

The aim is to design a device for unconstrained pick-and-place tasks, allowing to characterize for the first time brain processes that underlie natural reach-to-grasp movements. This extends the types of questions in the field of visuomotor control that can be asked by neuroimaging [3]. To cover all possible Cartesian motions of the human hand, including the possibility of rotations and a two finger precision grasp, the device should feature seven DoF. With such a device, specialized subtasks like reaching or lifting objects can also be rendered.

Minimum output capabilities have to be met along all DoF and a broad range of these have been defined for haptic interfaces by Fischer et al. as early as 1990 [24]. They include minimum velocities, accelerations, available workspace, and other. As a complement to these requirements, a typical pick-and-place experiment provides the minimum required torques, as well as lift and grasp forces. Light objects, comparable to a glass of water, should be manipulated. Thus, we can approximate the order of magnitude of weight as well as inertia of the objects, and thus forces and torques, to be rendered. An empty glass of water has a weight of approximately $m_{glass} = 0.2$ kg and a maximum inertia of $I_{glass} = 1000$ kgmm^2, as reported in Table 4.1.

Tabular 4.1: Parameters of a typical pick-and-place experiment for our device, lifting a light object such as a glass of water. Forces and torques can be derived using Newton's second law of motion, $F = m \cdot a$.

mass, inertia ·	maximum acceleration =	maximum force, torque
0.2 kg	9.81 m/s^2	1.96 N
1000 kgmm^2	15,000 deg/s^2	0.52 Nm

Assuming a maximum acceleration of $a_{trans} = 9.81$ m/s^2 [24] and the peak angular acceleration of the human wrist of $a_{rot} = 15,000$ deg/s^2 [88], we obtain a maximum force $F_{max} = 1.96$ N and torque $\tau_{max} = 0.52$ Nm to be rendered. This allows deriving the grip force. It depends mainly on the object weight and the friction coefficient. From literature we know that the correlation of the static grip force with the object weight is approximately linear [89]. Also the correlation of the maximum grip force with the inverse coefficient of friction μ is approximately linear with a safety margin F_{safety} [90]. Hence, the grip force can be approximated by

$$F_{grip} = F_{max} \cdot 1/\mu \cdot s + F_{safety}. \tag{4.1}$$

With $F_{max} = 1.96$ N, a friction coefficient of glass in a human hand $\mu_{glass} = 1.1$ [91], a safety margin $F_{safety} = 3$ N, and a slope of $s \approx 3$ [90], we obtain a grip force of $F_{grip} = 8.3$ N.

Besides these required output capabilities, the device should be compact enough such that it fits into the entry of the MR scanner bore. Moreover, it should be MR-compatible, safe and ergonomic for long-lasting fMRI studies. Thus, the design requirements can be summarized as follows:

- Seven actuated DoF at the end effector to allow a versatile application as well as natural, unconstrained pick-and-place tasks, with rotations of ±30° around all axes and a volume of operation of at least 300 mm^3 [24].
- The minimum force, torque and grip force output capabilities should be 1.96 N, 0.52 Nm, and $F_{grip} = 8.3\ N$, respectively. In order to provide a realistic feeling, the minimum translational velocities and translational accelerations should be 1 m/s and 9.81 m/s^2, respectively [24].
- Compact design, such that the device fits into the entry of the MR scanner bore.
- Bi-directional MR-compatibility of the entire system should be provided: Neither image artifacts should occur, nor position control precision should be affected by the MR environment.
- Safe and ergonomic usage of the device should be provided, such that subjects can perform natural motions even in long-lasting fMRI studies.

4.3 Design of an MR-compatible haptic interface

The realized system, called MR-Octo, is based on an Octopod kinematics, extended with a haptic gripper.

4.3.1 Octopod

The Octopod kinematics has been designed particularly for an application in MR environments and is depicted in Figure 4.1. It employs eight $\underline{R}$RRS legs and provides six DoF. Each leg consists of three rotational joints and one spherical joint, whereas only the first rotational joint is actuated. All actuators are non-floating and thus, remain stationary during movement of the end effector. This avoids image artifacts and decreases the inertia of moving components. In contrast to Hexapod kinematics, the Octopod kinematics also avoids singularities by design and thus, has an increased dexterous workspace as shown in the previous chapter.

The kinematic parameters of the haptic interface are chosen consecutively and aim to meet our first three design criteria: First of all, distance l_d and angle γ are minimized, which improves isotropy and output capabilities of the device, as already presented in Chapter 3. Secondly, the overall compactness of the device is maximized, such that it fits into the entry of the MR scanner bore. The size of actuation units ultimately determines the minimum realizable base radius l_0. Finally, lengths l_1, l_3, and l_4 are chosen in an iterative process that guarantees both workspace and minimum output capabilities to be achieved. Typically, a compromise between force/torque and velocity capabilities has to be made given a certain

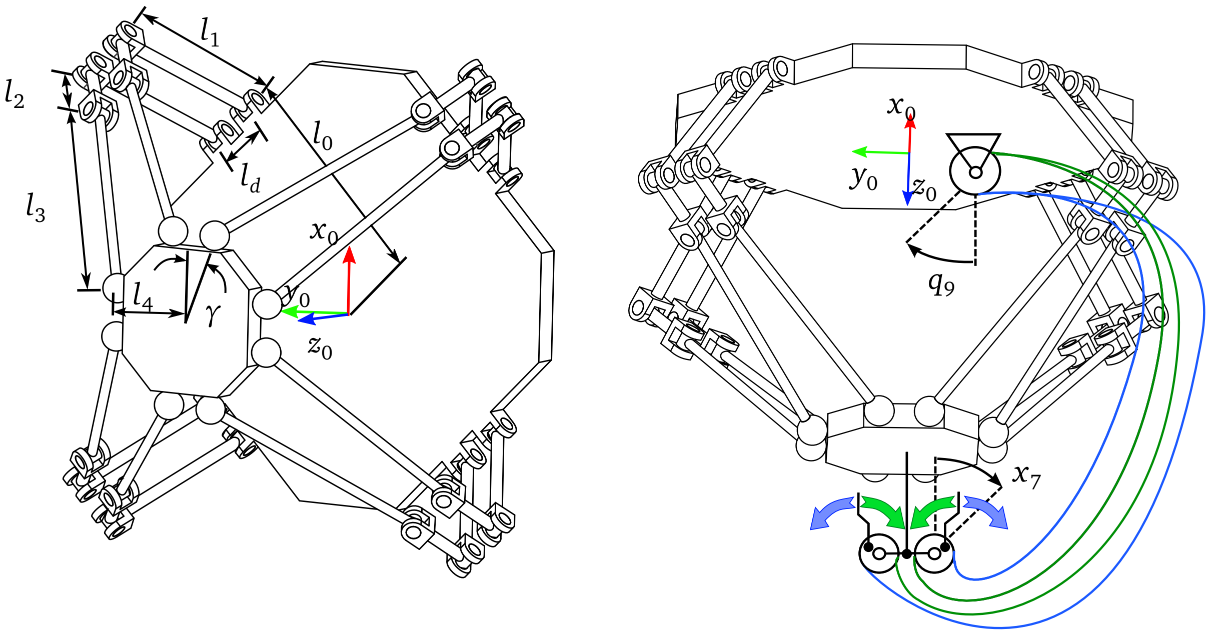

Figure 4.1: Octopod kinematics providing six DoF (left) and Octopod kinematics augmented with schematic haptic gripper, driven by Bowden cables (right).

set of actuators. For this first prototype, no formal optimization was carried out and lengths l_1, l_3, and l_4 were determined by the designer.

The resulting kinematic parameters of the MR-Octo are $l_0 = 0.17$ m, $l_1 = 0.08$ m, $l_2 = 0.03$ m, $l_4 = 0.06$ m, $l_d = 0.02$ m, and $\gamma = 18.34°$. Moreover, the kinematics is oriented such that gravity g acts along the negative x_0 axis. This distributes the weight of the kinematics equally among the eight actuators. The kinematics constitutes the basis of the MR-compatible haptic interface. A rendering of the complete CAD design is shown in Figure 4.2.

The system is actuated by nine USMs in total. Ten optical encoders measure their position as well as the gripper's orientation. A Mini27 Titanium six DoF force/torque sensor from ATI IA at the end effector measures interaction forces and torques.

Tabular 4.2: Overview of components, their materials and their magnetic volume susceptibility in SI-units.

Component	Material	χ_v
Structural components of Octopod and frame	PVC	$-10.71 \cdot 10^{-6}$
Haptic gripper housing	PC	$-9.56 \cdot 10^{-6}$
Haptic gripper screws	Brass	112
Ball bearings	ZrO_2	-0.64
USM housing and stand	Copper	$-9.63 \cdot 10^{-6}$
Six DoF Force/Torque Sensor and screws	Titanium	$1.81 \cdot 10^{-4}$

Most structural components of the device are made from polyvinyl chloride (PVC), poly-

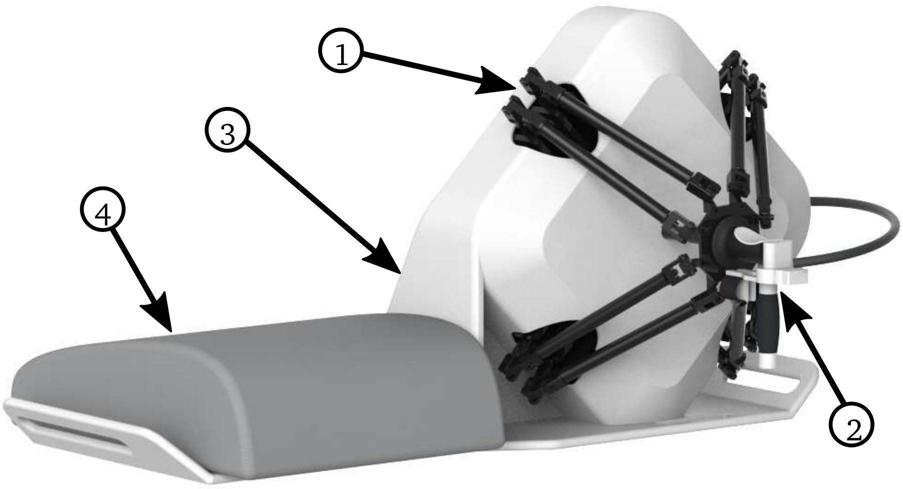

Figure 4.2: MR-Octo (1) for right-handed operation with haptic gripper (2), mounted on a support frame (3) that also carries an MRI pillow (4), supporting the subject's legs.

carbonate (PC), and copper. The latter has been selected due to its thermal conductivity as well as shielding capability. Since the USMs are driven via friction, the temperature rises during prolonged operation. Employing copper as motor stand and housing material allows cooling the USMs during operation. Further components are titanium screws as well as ceramic ball bearings. The employed components, their materials as well as their magnetic volume susceptibility are listed in Table 4.2. The magnetic volume susceptibility allows classifying the level of magnetizability of the components. Diamagnetic materials ($\chi_v < 0$) are repelled by the magnetic field, paramagnetic and ferromagnetic materials ($\chi_v > 0$) are attracted by the magnetic field. As a reference, iron has a magnetic volume susceptibility of $200,000$. The materials were chosen depending on the components primary function, but also in light of their potential MR-compatibility, which finally needs to be experimentally validated.

4.3.2 Haptic gripper

The gripper has been developed by Deakin University, Australia and is based on a concept by Zoran Najdovski [92]. In cooperation, an MR-compatible version has been realized and is employed in the haptic interface. The gripper uses Bowden-cable actuation and thus, can move in space in six DoF without being affected in its performance. Technically, two DoF can be actuated separately. For the presented prototype, both DoF are coupled such that both tips of the gripper move simultaneously, as depicted in Figure 4.1. The actuation unit, built by the authors of this paper, consists of a ninth USM and a simple pulley.

4.3.3 Support frame

The Octopod kinematics is mounted on a support frame as shown in Figure 4.2. The support frame has been designed in order to provide an ergonomic, safe as well as easy installation of the entire system. It is also made from MR-compatible materials, such as PVC and titanium. It allows right-handed operation of the haptic interface and can be adjusted in two DoF, lengthwise and laterally, to the proportions of each subject. On the left side of the support frame, an MRI pillow is placed that supports the subject's legs during long-lasting experiments.

4.4 Visual and haptic rendering

The haptic rendering runs on a workstation and is implemented in CHAI3D along with the visualization of the virtual environment. The haptic device is operated in admittance control mode.

4.4.1 Hardware and software setup

The haptic interface is connected to a workstation that executes control algorithms and performs visual and haptic rendering of a virtual environment. The signal flow between the MR-Octo and the workstation is depicted in Figure 4.3. Commands to the motor drivers are computed via Matlab/Simulink and are executed by a Linux real-time kernel at a sampling rate of 1 kHz. Forward and inverse kinematics are solved by MotionGenesis$^{\text{TM}}$ Kane.

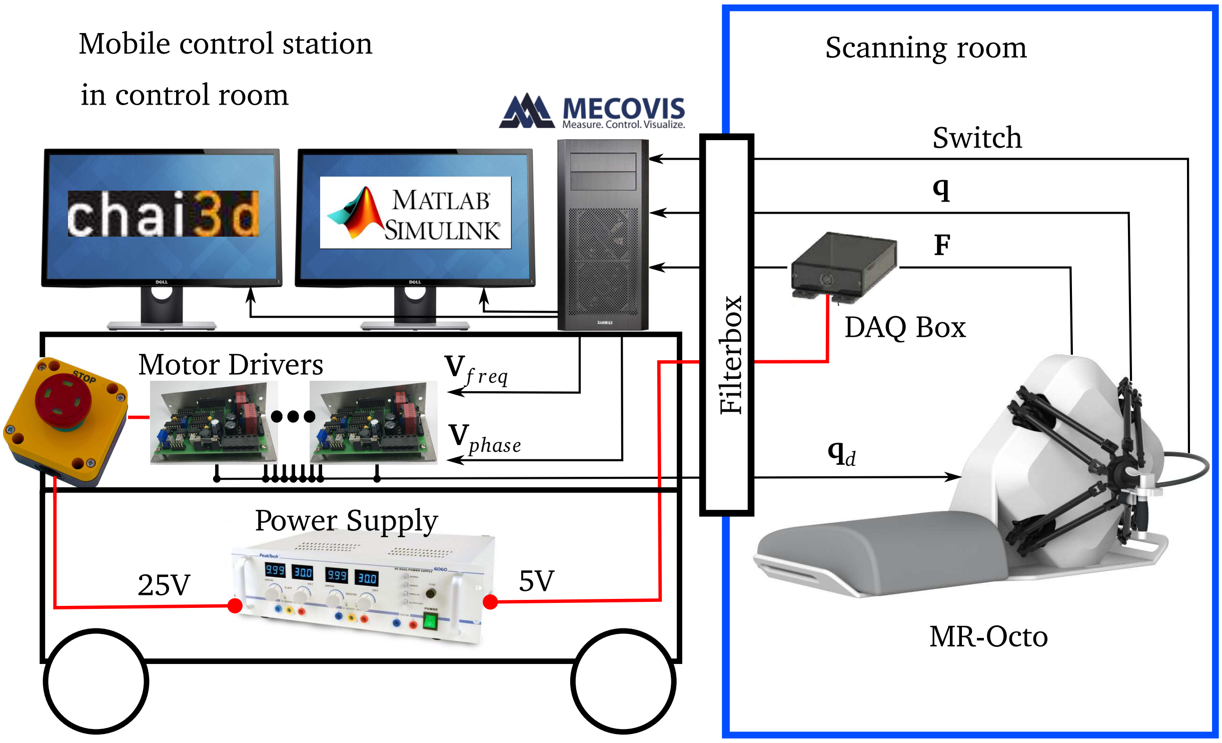
Mobile control station
in control room
MECOVIS
Measure. Control. Visualize.
chai3d
MATLAB SIMULINK
Motor Drivers
$\mathbf{V}_{freq}$
$\mathbf{V}_{phase}$
STOP
Power Supply
25V
5V
Filterbox
Scanning room
Switch
$\mathbf{q}$
$\mathbf{F}$
DAQ Box
$\mathbf{q}_d$
MR-Octo

Figure 4.3: Signal flow between the mobile control station on wheels in the control room (left) and the scanning room (right). All signals are filtered as they pass from one room to the other.

The communication with the hardware is managed via three Mecovis I/O cards. Those output two voltages, $V_{i,freq}$ and $V_{i,phase}$, in the range of $[-10;\ 10]$ V per motor i, in order to set the desired motor positions $\mathbf{q}_d$. The actual motor positions $\mathbf{q}$ as well as the measured forces and torques $\mathbf{F}$ are fed back to the workstation. The subject can also use a switch at the gripper to turn the haptic interface on or off.

4.4.2 Virtual environment

The visual and haptic rendering of the virtual environment is performed in Chai3D [93]. Matlab/Simulink sends the end effector position $\mathbf{x}$ to Chai3D via a shared library. Chai3D computes interaction forces $\mathbf{F}_{vr}$ and sends them back using the same shared library. An example of a virtual environment that can be rendered is depicted in Figure 4.4.

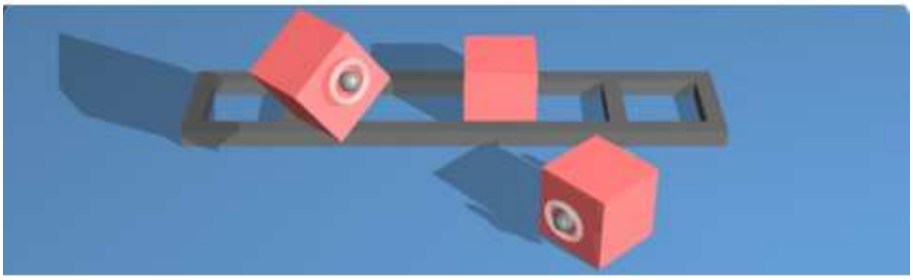

Figure 4.4: Chai3D example: Three cubes can be manipulated.

4.4.3 Control of the haptic interface

The haptic interface is controlled via an admittance control scheme that determines the interaction with the human operator and the virtual environment. An overview is depicted in Figure 4.5.

Admittance control

Haptic interfaces are usually controlled by one of the two complementary control paradigms, impedance or admittance control. For impedance control, positions are measured and forces are commanded to the actuators. Conversely, for admittance control, forces are measured, whereas positions of the actuators are set. Since USMs are non-backdriveable, admittance-type actuators, the admittance control paradigm has been adopted. Here, a minimal virtual mass $\mathbf{M}$ and damper $\mathbf{D}$ are rendered to keep the controller stable, and the resulting system can be written as

$$\mathbf{M}\ddot{\mathbf{x}}_d + \mathbf{D}\dot{\mathbf{x}}_d = \mathbf{F}_{vr} - \mathbf{F}. \tag{4.2}$$

Matrices $\mathbf{M}$ and $\mathbf{D}$ are diagonal 7×7 matrices with a virtual mass m_i and damping d_i for each DoF, respectively. Desired velocity $\dot{\mathbf{x}}_d$ and acceleration $\ddot{\mathbf{x}}_d$ of the end effector are 7×1 vectors, similar to the measured force $\mathbf{F}$ and the rendered force $\mathbf{F}_{vr}$. The force for all Cartesian DoF at the end effector is measured by the Mini27 Titanium force/torque sensor.

The haptic gripper requires force measurement for admittance control. The force applied at the gripper is a function of the gripper angle x_7 and the position of the ninth USM q_9, as

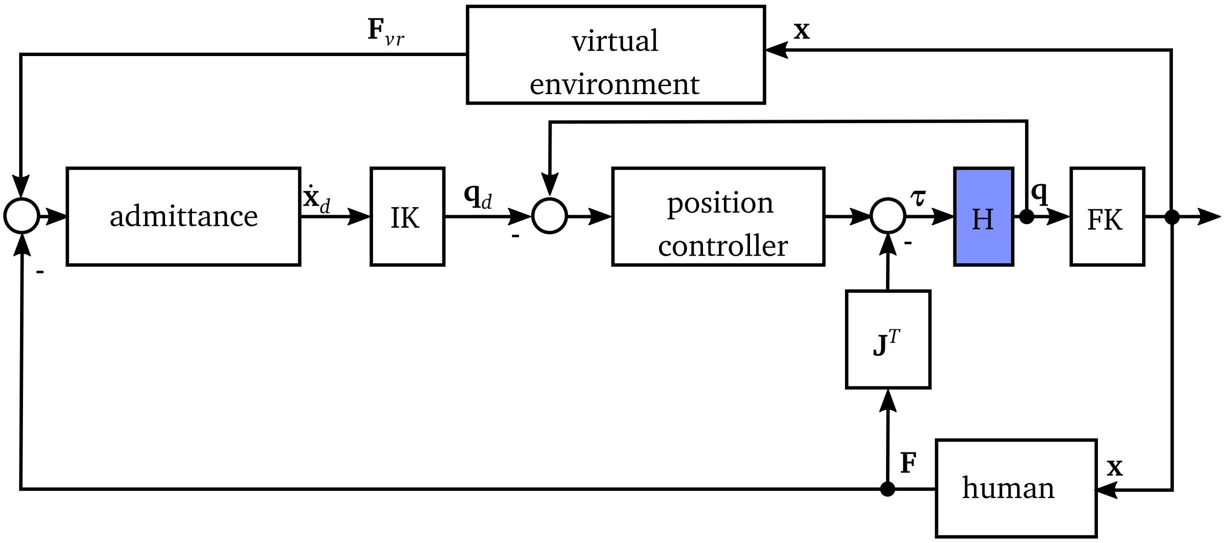
$\mathbf{F}_{vr}$
virtual environment
$\mathbf{x}$
admittance
$\dot{\mathbf{x}}_d$
IK
$\mathbf{q}_d$
position controller
τ
H
$\mathbf{q}$
FK
$\mathbf{J}^T$
F
human
$\mathbf{x}$
-

Figure 4.5: Admittance control scheme that determines the interaction of haptic interface (H) with virtual environment and human operator. Forward kinematics (FK) and inverse kinematics (IK) transform between Cartesian and joint space. A low-level position controller sets desired actuator positions.

depicted in Figure 4.1, and the spring stiffness of the Bowden cables. With an approximation of the spring stiffness K, the exerted force at the gripper yields

$$F_{gripper} = K(q_9 - x_7). \tag{4.3}$$

In order to render a stiff contact with the virtual environment, we use the gripper orientation x_7 as input to the virtually rendered impedance, instead of the actively controlled position q_9. Please note that q_9 is used for the low-level position control to avoid oscillations. These would result when using x_7, as it is a non-collocated variable with respect to its actuator USM 9. The principle is visualized in Figure 4.6.

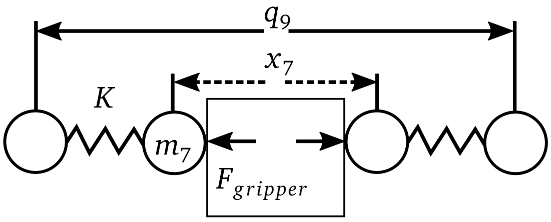
q_9
x_7
K
m_7
$F_{gripper}$

Figure 4.6: Gripper principle, where approximated Bowden cable stiffness K, USM position q_9, and gripper orientation x_7 generate a grasp force $F_{gripper}$. Grasping an object also leads to a virtual reaction force $F_{vr,7}$, which is not depicted.

Low-level position control

In order to realize the admittance control scheme, the employed USMs have to be foreseen with a low-level position control. However, commercial motor drivers do not allow low velocities, which typically occur when interacting with haptic interfaces. In Chapter 2, we have presented a hybrid sliding-mode control scheme that allows both high and low velocities and is based on a second-order model of the USM. This controller is employed as low-level position controller.

4.5 Human factors analysis

A safe and ergonomic design are essential for the MR-Octo, since it is a tool for human motor control studies. This requires an analysis of the hardware and software components of the entire system. In order to design the haptic interface such that it is ergonomic and safe, we followed the guidance by the Food and Drug Administration (FDA) 'Applying Human Factors and Usability Engineering to Medical Devices'.

4.5.1 Methods for human factors analysis

The guidance by the FDA contains recommendations in order to maximize the likelihood of obtaining a safe and effective medical device. The MR-Octo is not a medical device in the narrower sense, but is used in a clinical-like environment, i.e. an MR scanner. The proposed process contains several steps: (1) Define intended users, use environments, and user interfaces. (2) Identify use-related hazards. (3) Identify and categorize critical tasks, i.e. a task which, if performed incorrectly or not at all, leads to harm or damage. (4) Develop and implement risk mitigation/control measures. (5) Validate use safety and effectiveness. (6) If the use-related risks are unacceptable or new use-related risks are introduced, steps 4 and 5 are reiterated. Finally, in step (7) the Human Factors Engineering (HFE)/Usability Engineering (UE) process is documented.

The process was carried out iteratively, and the system was evaluated at multiple stages. First of all, the situation where both a subject and a haptic interface are in the MR scanner was modeled using a puppet scenario. In a second step, a dummy MR scanner and a dummy MR-Octo, both made from cardboard, were realized. Then, a first prototype of the MR-Octo and a preliminary support frame were tested in a real MR scanner. These three steps allowed identifying mainly ergonomic and mechanical issues. In parallel, interviews with expert MR scanner users and electric engineers were conducted, in order to identify critical tasks as well as electrical, thermal, and noise hazards. Thus, risk mitigation measures could be instantiated accordingly.

4.5.2 Results

The presented results focus on two key aspects of the iterative process from the FDA: A presentation of the triplet users, use environment, and user interfaces as well as remaining use-related hazards and critical tasks combined with the associated risk mitigation measures.

Description of intended device users, use environments, and user interfaces

The users, use environments, and user interfaces describe the setting in which the MR-Octo is employed. While the first two groups can only be influenced partially in the design process, a safe and ergonomic design can be realized via user interfaces.

Device users: Typically, there are two groups of users of the MR-Octo. First of all, there are subjects participating in a human motor control study. They are mostly naive to the use of haptic interfaces or robotic systems in general. The subjects receive an introduction to the MR scanner as well as to the MR-Octo, such that they are familiar with the systems and the user interfaces. Secondly, there are neuroscientists that design and carry out fMRI studies with the device. For a study at the MPI for Biological Cybernetics in Tübingen, at least two scientists have to be present. One has to be an advanced user of the MR scanner and the other one has to be at least a basic user. A basic user has knowledge about the potential risks related to the MR scanner as well as safety measures. The status of a basic user can be obtained via an MRI safety training. An advanced user is well experienced with the use of an MR scanner and the status can be obtained after sufficient working experience. Both scientists that are present for the fMRI study should be familiar with the MR-Octo and its capabilities. However, they are still not technical experts on every detail of the system.

Use environments: The MR-Octo is designed for use in MR scanners. Hence, strong magnetic fields are expected and moreover, the subjects as well as the system share a small workspace. Additionally, noise levels during fMRI analyses are high. Verbal communication with the subject and auditory fault detection are not possible during the scans.

Furthermore, scanning time at MR scanners is typically costly and limited. This means that the device has to be brought in and out of the scanning room several times for a study with multiple subjects. Moreover, the device is mostly not located in the scanning room, but in a preparation room next to the scanning room.

Device user interfaces: There are three main user interfaces for the scientists employing the MR-Octo: First of all there are two handles on the support frame, such that the system can be carried by two persons, as depicted on the left in Figure 4.7. The handles remain accessible to adjust the position of the system when a subject is lying on the scanner bed. Second, there are screws with knurling, in order to lock the position of the support frame on the scanner bed. Third, three cables are attached to the MR-Octo and the filter box in the control room: one cable for the motors, one cable for the encoders, and one cable for the six DoF force/torque sensor.

The subject has three points of interaction with the MR-Octo, as shown on the right in Figure 4.7. The right hand grasps the haptic gripper, the legs are placed on an MRI pillow, and a virtual environment is displayed on a screen visible through a mirror on the head coil. Within the virtual environment, the subject can see if the MR-Octo is activated or not. With a switch at the gripper and in manual mode, the subjects turns the haptic interface on or off. In automatic mode and during a study, the haptic interface is turned on and off depending on the rendered task. Since the actuators are non-backdriveable, the current position of the

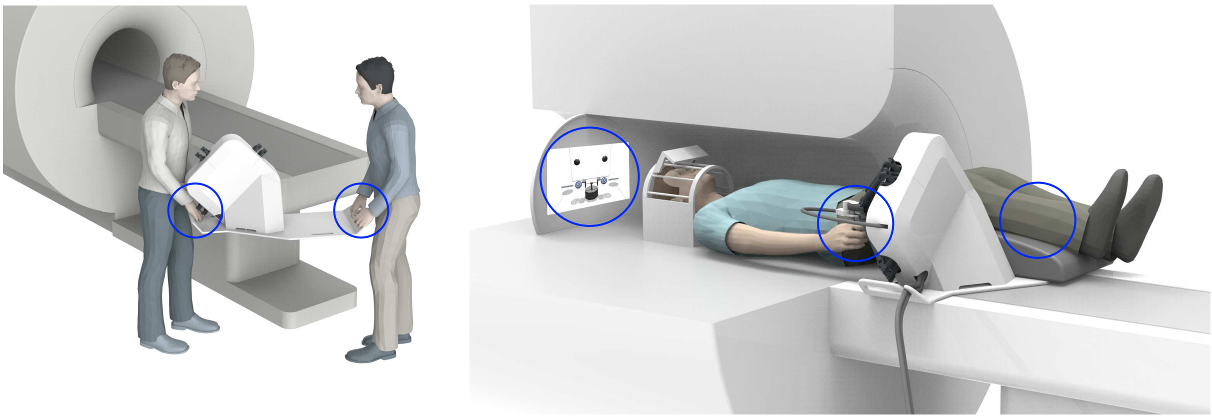

Figure 4.7: Main user interfaces of the MR-Octo for scientists (left) and subjects (right).

end effector will be held while the device is off. Moreover, the subject can turn the MR-Octo off in any situation using the switch at the gripper.

Analysis of hazards and risks associated with use of the device

We classify hazards and risks according to the ISO 10218-2. Hazards resulting from a general fMRI scan without the MR-Octo are only listed if there is a relation to the haptic interface.

Mechanical hazards

- *Movement of the end effector and gripper may lead to crushing the hand between haptic interface and MR scanner.* Countermeasures are a limited workspace, force/torque and velocity production, implemented in software, in order to reduce likeliness and severity of an impact.

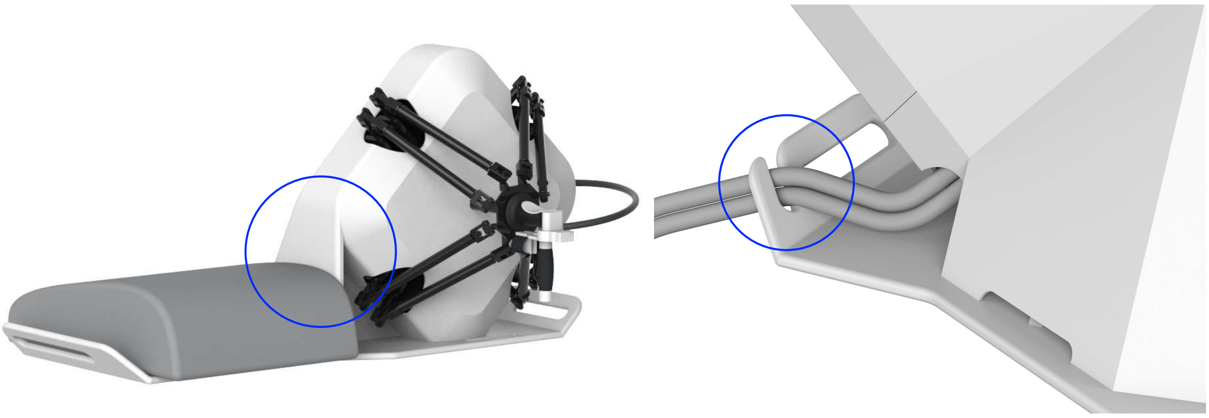

Figure 4.8: Protection that separates user legs from robot legs (left) and secure clamping of cables (right).

- *Movement of the robot legs might lead to an impact on the subjects' legs.* As a countermeasure, the support frame is designed in such a way that subjects' and robot's legs remain separated by a small wall. This is shown on the left in Figure 4.8.

- *Repeated plugging and unplugging of the nine motors and encoders might lead to mixed cables or cable breaks, and consequently to an uncontrolled motion of the end effector due to faulty signals.* As a countermeasure, two main cables bundle all motor as well as encoder signals and plugs are from non-magnetic metal and thus, robust.

- *The movement of the MR scanner bed might unplug the two cables for motors and encoders and either switch off the system unintentionally or lead to an uncontrolled motion of the end effector.* As countermeasures, the connectors are secured via screws and cables are clamped on the support frame, as depicted on the right in Figure 4.8.

Electrical hazards

- *Contact with live parts, such as connectors, can result in electrocution.* As a countermeasure, a non-conducting chassis protects live parts and connections from contact with the environment.

- *During the installation of the system, the main cables for motors and encoders might be connected to the wrong slots at the MR-Octo and the filter box of the scanner room. This can result in damage to the encoders.* As a countermeasure, plugs for motors and encoders are different and either female or male, respectively. Hence, the cables cannot be confused.

Thermal hazards

- *Hot surfaces associated with the MR-Octo may occur due to the RF pulses of the MR scanner and lead to burns.* As a countermeasure, only non-magnetic components that do not heat up are used at the outside of the haptic interface. Furthermore, no cables of the device are located close to the subject.

- *Surfaces of the USMs might heat up after long operation times.* As a countermeasure, the chassis protects the motors from being touched from the outside.

Noise hazards

- *High noise levels during fMRI scans prevent hearing or understanding audible danger warning signals. This also includes the inability of persons to coordinate their actions through normal conversation.* As a countermeasure, the haptic interface can always be turned off by the subject using the gripper switch. This can be the case if the subject in the MR scanners detects a danger or wants to pause the study. Moreover, using the emergency squeeze ball inside the MR scanner, a loud noise can be heard in the control room, signaling a cancellation of the ongoing trial.

Ergonomic hazards

- *An inappropriate location or identification of controls, i.e. the haptic gripper, may lead to unhealthy postures or excessive effort of the subject.* As a countermeasure, the haptic interface can be adjusted on the scanner bed during training. To do so, the frame can be moved lengthwise and laterally. Hence, an ergonomic posture can be ensured, as depicted in Figure 4.9.
- *An inappropriate location of controls may lead to unhealthy postures or excessive effort of the scientists while carrying the frame.* As a countermeasure, handles that are easily accessible were added to the frame such that it can be carried with little effort. This is depicted on the left in Figure 4.7.

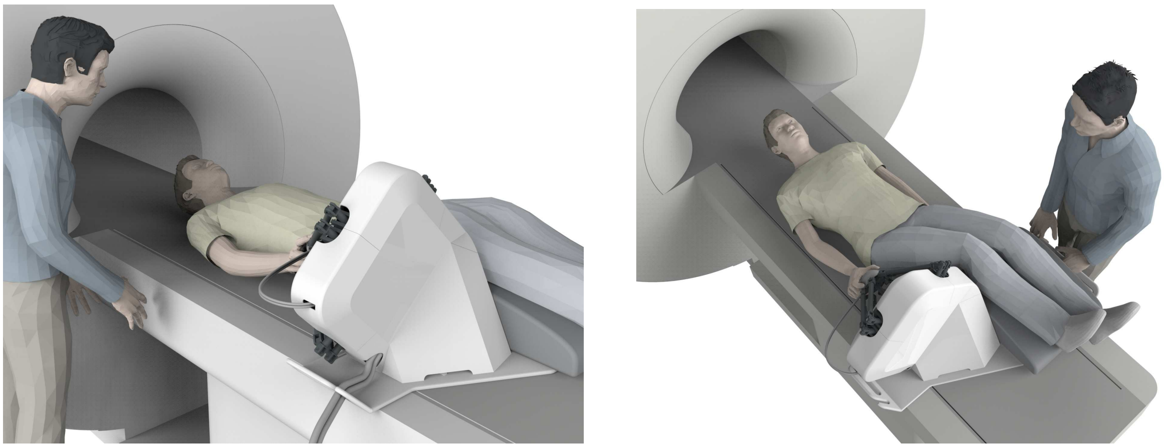

Figure 4.9: Guided training of the subject (left) and adjustment of the position of the haptic interface to reach an ergonomic position (right).

In conclusion, the remaining hazards and critical tasks in the scanner room, related to the MR-Octo system, were first of all identified via different methods. Then, they were addressed via countermeasures that ensure safety and an ergonomic handling of the system.

4.6 Experimental validation

Taking into account the countermeasures that ensure a safe and ergonomic design, a prototype of the MR-Octo could be realized. Photographs of the device are depicted in Figure 4.10.

With this prototype, the successful implementation of the design requirements, which were established earlier, are validated experimentally and quantified via performance indices.

4.6.1 Performance indices

Workspace

The dexterous workspace describes the maximum volume, in which rotations in a certain range around all axes can be achieved. This volume is quantified, along with the reachable workspace at zero rotations, as a comparison.

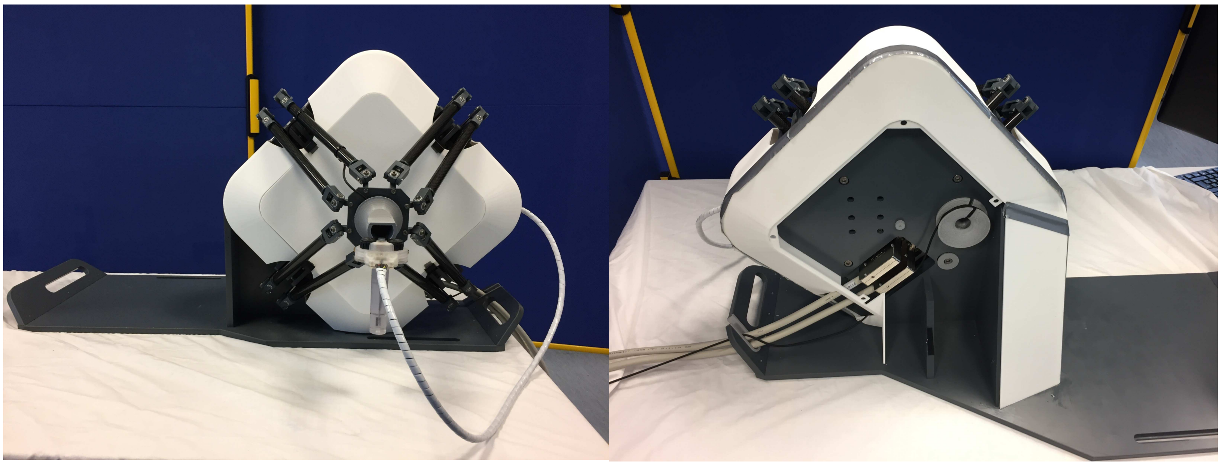

Figure 4.10: Photographs of the MR-Octo from front (left) and back (right). The backside can be closed entirely by the chassis, which is not depicted.

Worst-case output capabilities

In order to verify if our design criteria are met in terms of force, torque, velocity, and acceleration, the worst-case output capabilities are quantified. For actuation-redundant actuators the problem is over-constrained and thus, we employ the ‘polytope algorithm’ introduced in Chapter 3.

4.6.2 Results

Dexterous workspace

The size of the dexterous workspace of the MR-Octo is mainly determined by physical joint limits and link lengths. The maximum volume, where rotations of ±30° and ±20° can be achieved around all axes, is shown in Figure 4.11 as green and magenta volume, respectively. The reachable workspace at zero rotations is shown in blue. The dexterous workspace with ±30° rotations around all axes is approximated with a sphere (S30), centered at $z = 0.24$ m and with a diameter of 30 mm, which is also depicted in Figure 4.11. The dexterous workspace with ±20° rotations around all axes is also approximated with a sphere (S20) with a diameter of 50 mm (not shown).

Worst-case output capabilities

Via a theoretical and experimental evaluation of worst-case output capabilities, we verify if the design goals in terms of minimum force, velocity and acceleration are met. The spherical workspaces S20 and S30 are sampled with a translational step size of 2 mm and a rotational step size of 10° in a range of ±20° and ±30° around all axes, respectively. The USMs produce a nominal torque of $\tau_{i,max,n} = \pm 0.5$ Nm, a stall torque of $\tau_{i,max,st} = \pm 1.0$ Nm, and a nominal velocity of $v_{i,max,n} = \pm 10$ rad/s. The Cartesian mass matrix is approximated with the help of CAD data as $\hat{\mathbf{M}} = diag[m_{OC} \quad m_{OC} \quad m_{OC} \quad I_x \quad I_y \quad I_z]$ with $m_{OC} = 0.05$ kg, $I_{x,y,z} = 3 \times 10^{-4}$ kgm^2, and the similarity transformation to joint coordinates $\mathbf{M}_q(q) = \mathbf{J(q)}^T \hat{\mathbf{M}} \mathbf{J(q)}$.

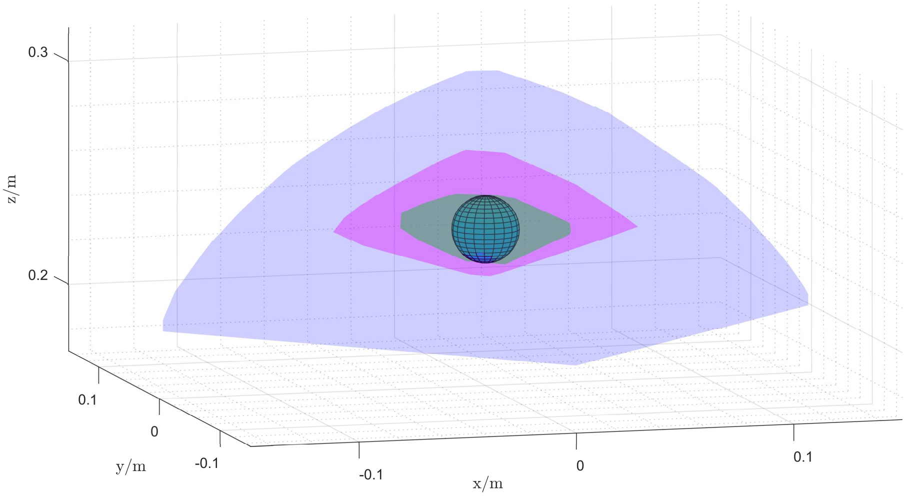

Figure 4.11: Reachable workspace with only translational displacements of the Octopod kinematics, depicted in blue and dexterous workspace volumes, where ±30° and ±20° rotations around all axes are achievable shown in green and magenta, respectively.

The resulting worst-case output capabilities of the kinematics within the workspaces and considering allowed rotations around all axes, are listed in Table 4.3.

Tabular 4.3: Worst-case output capabilities of the MR-Octo in its dexterous workspace.

Output capability	Simulation		Experiment	
	S20	S30	S20	S30
Continuous force/N	7.83	7.45	7.51	6.87
Continuous torque/Nm	0.49	0.43	0.46	0.41
Velocity/(m/s)	0.34	0.16	0.44	0.42
Angular velocity/(rad/s)	8.53	6.78	14.09	13.82
Acceleration/(m/s^2)	239.33	227.79	515.69	378.47
Angular Acc./(rad/s^2)	3302.30	2891.64	5726.61	4301.62

Additionally, the worst-case output capabilities of the gripper were evaluated and results are listed in Table 4.4.

Tabular 4.4: Worst-case output capabilities of the gripper.

Output capability	Simulation	Experiment
Continuous force/N	7.14	5.04
Velocity/(m/s)	0.11	0.21

4.7 MR-compatibility validation

Finally, the MR-compatibility of the entire system was validated in order to ensure its applicability for fMRI analyses.

4.7.1 Validation methods

The bi-directional MR-compatibility was validated in a 3T MRI scanner (Prisma, Siemens Healthcare, Erlangen, Germany) equipped with a 20-ch Siemens head coil and a phantom filled with a saline water solution. The procedure was carried out in three major steps: In the first step, we used a double-echo gradient echo sequence to create a B_0 map without any device present. Then, with the device placed at the entry of the scanner bore and powered off, another B_0 map was recorded. This allowed verifying that the device does not lead to distortions in the B_0 field that cannot be corrected by shimming. Then, in a second step and after shimming, radio frequency (RF) noise was measured with the device powered on and moving. In the third and last step, we ran an echo planar imaging (EPI) sequence while the device altered between moving and holding its position, in an ON/OFF block design. The signal-to-fluctuation-noise ratio (SFNR) that was calculated from EPI images and the RF noise spectrum and the signals recorded from the device were then used to determine the MR-compatibility.

Titanium six DoF force/torque sensor

Using this procedure, the six DoF force/torque sensor was validated individually, prior to an evaluation of the entire system. The Mini27 Titanium six DoF force/torque sensor relies on a strain gauge based measurement principle that outputs an analogue signal. Hence, it is particularly susceptible to the magnetic field, in contrast to an optical measurement principle or a digital signal. Noise levels were determined to indicate whether filters, and thus delays, needed to be introduced or force dead zones had to be respected. The test setup at the entry of the MR scanner bore is depicted in Figure 4.12.

The ATI was placed on a support such that it was in a comparable position to its later point of operation in the isocenter of the magnetic field. Since the sensor was not actuated, it was oriented and moved by hand in ranges that are comparable to the later workspace of the haptic interface. First, the sensor was in an upright position, as depicted in Figure 4.12. Then, the sensor was tilted about ±30° around its x and y axis. Signals were recorded for 30 s in every orientation. The sensor was also placed in four different locations, each 10 cm away from the central position along the x and z axis.

Haptic Interface

The MR-compatibility of the entire haptic interface was determined in a second step. The respective setup is depicted in Figure 4.13. During the ON-blocks, the device moved sinusoidally along its z-axis with an amplitude of 2 cm and at 2 Hz. During the OFF blocks, the haptic interface held its last position and motors were switched off.

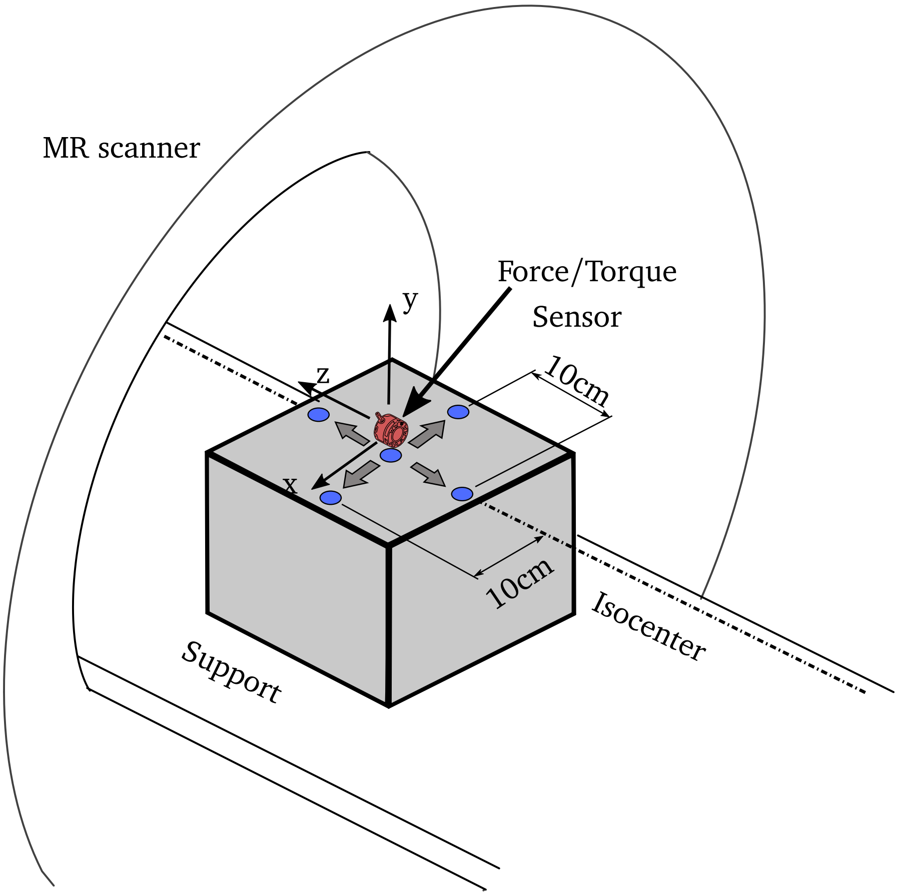

Figure 4.12: Setup for MR-compatibility test of force/torque sensor.

4.7.2 Results

Titanium six DoF force/torque sensor

RF noise measurement and EPI quality: The RF noise measurements show that the there is no RF interference from the sensor leading to image artifacts. Mean and signal-to-fluctuation-noise ratio (SFNR) for the EPIs were also acquired when the sensor was turned off and on. The difference of two states OFF and ON was calculated and no systematic variation or pattern could be found.

Impact of MRI on sensor signal quality: The data was acquired at 1 kHz and noise from the scanner was found at 220 Hz and 800 Hz. This finding is consistent over all tested positions and orientations. The width of the noise envelope is about 0.05 N in the center position and doubles when the sensor is moved 10 cm along the z axis into the scanner. Finally, a dead zone of ±0.1 N was introduced for force measurements and ±0.05 Nm for torque measurements.

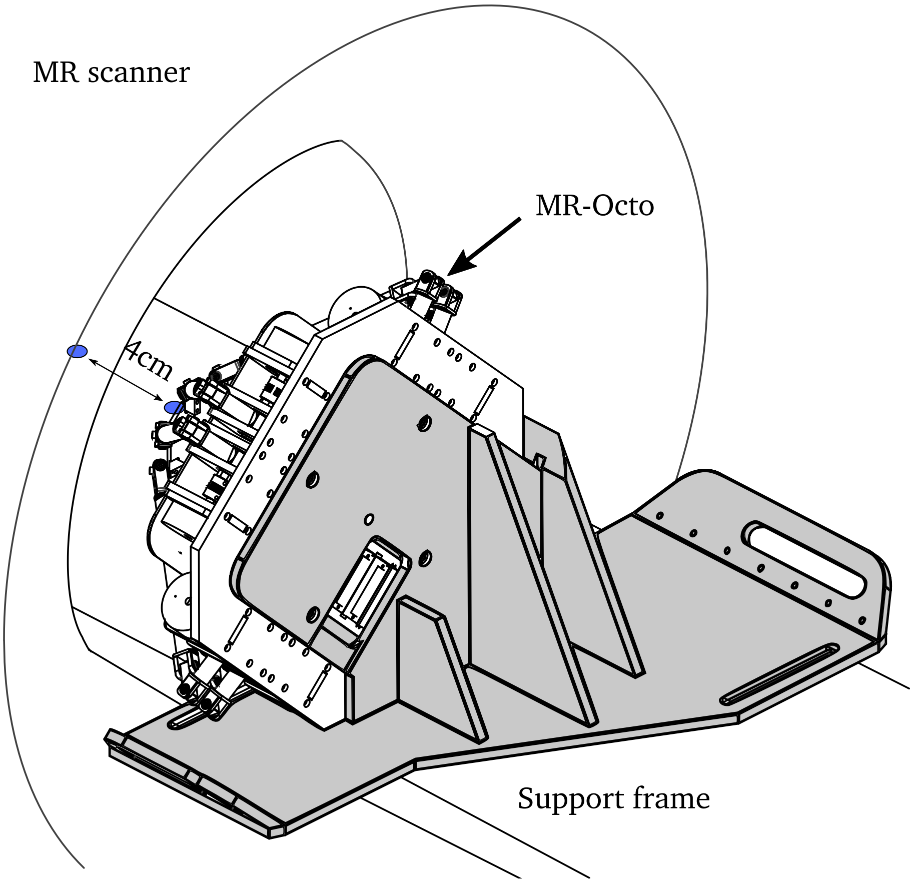

Figure 4.13: Setup for MR-compatibility test of the MR-Octo.

Haptic Interface

RF noise measurement, impact on B0 homogeneity and fMRI quality: The difference maps for the B_0 measurements, reveal a general offset between the case when the device was present in the bore versus the case without the device. However, these changes can be corrected by re-applying the shimming procedure of the scanner. The analysis of the RF noise spectrum for the device powered off versus the device performing a sinusoidal motion do not show any increase of undesired frequencies in the noise spectrum.

The fMRI analysis was based on the General Linear Model (GLM) and was done with FSL 5.0 (FMRIB, Oxford University, UK). A high pass cut-off of 120 s was chosen for the 30 s ON/OFF block design. In order to see voxel-level activation as well as an uncorrected z-map without spatial smoothing, thresholded statistical data with $p > 0.05$ was analyzed. Figure 4.14 depicts the recorded data for the two conditions, device alternating between switched off for 30 s and the device switched on and performing a sinusoidal motion for 30 s. The random distribution across the volume, the absence of clustering, and the amount of false positives indicates no change of the pattern due to the presence of the moving device. Additionally, an independent component analysis (ICA) was performed on the data which did not show any components correlated to the ON/OFF pattern or the sinusoidal movement of the device.

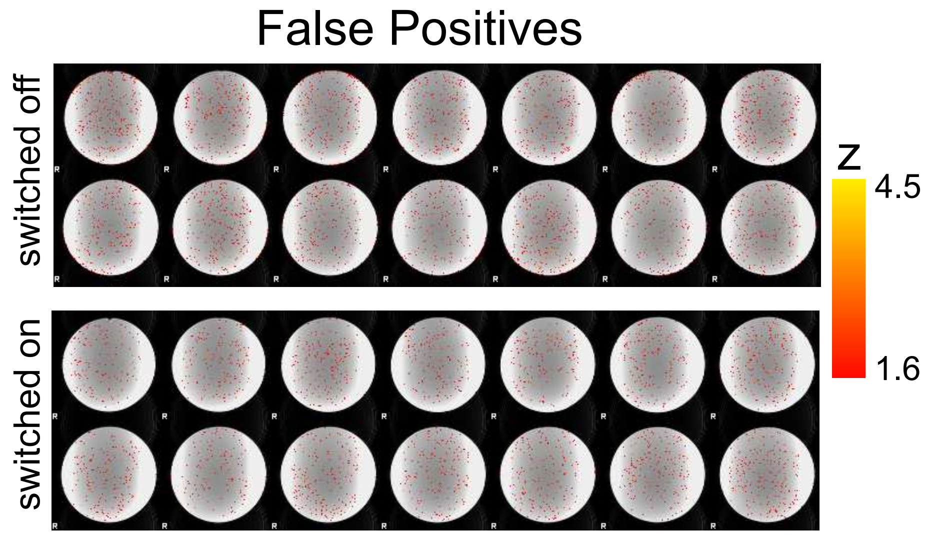

Figure 4.14: The results of the GLM analysis for the device switched off (top) and switched on as well as moving (bottom). The absence of false positives in the background is due to an automatic masking procedure during the analysis.

Impact of MRI on the tracking capability: The tracking capability of the sinusoidal trajectory by the haptic interface is not impaired by the MRI. Performances during the scanning and outside the scanning room are indistinguishable and mean tracking errors are both times 0.04 mm.

4.8 Discussion

Our design requirements in terms of actuated DoF are met and rotations of ±30° can be achieved in the dexterous workspace with a volume of 14137 mm^3. Moreover, the evaluation of safety and ergonomics allows us to conclude that the system can be applied for human motor control studies. No danger for subjects or scientist remains. The desired minimum output capabilities in terms of force and acceleration are also achieved. The worst-case grip force is at 61% of the desired value. Worst-case torque and velocity in the dexterous workspace S30 are at 94% and 15% of their desired values, respectively. This reflects the typical compromise between force/torque and velocity capabilities that has to be made given a certain set of actuators. We reduced the worst-case velocity capability for the sake of force and torque production during the design process, since we expect force production tasks to be more frequent than tasks with very rapid movements. Moreover and as shown by the experimental results, the USMs can produce higher velocities than simulated for short amounts of time. Besides, with rotations of ±20°, a 360% larger workspace can be covered and worst-case output capabilities increase to the values given in Table 4.3. If required, the design of the haptic interface also allows to easily change the link lengths and thus to adapt the haptic interface to velocity-focused tasks, if necessary.

Since USMs have been employed in a broad variety of MR-compatible devices [18,19], the MR-compatibility of our device is not surprising. However, our device contains the largest number of USMs, nine in total, ever tested to the best of our knowledge. Individual structural components or sensors that may have also interfered with the MR environment have been shown to have no significant impact at the test position in the Siemens 3T scanner. Hence, MR-compatibility can be concluded for this case.

4.9 Conclusion

In this work, we presented the first universal haptic interface with seven DoF for fMRI studies in the field of human motor control. It endows neuroscientists with a tool that can be reprogrammed and does not have to be redesigned, when moving on to a new research question. The presented analysis shows the MR compatibility of the developed system in a 3T scanner. In terms of desired output capabilities, a compromise has been made in favor of a higher force/torque output and taking into account smaller worst-case velocities.

Future work should address this compromise by a task-specific optimization of the kinematic's parameters. Furthermore, it should be directed towards conducting human motor control studies with the MR-Octo. In this work, we set up a benchmark study for a first validation of the device, as presented in the following chapter, but human motor control studies are left for the future.

5 Towards a Benchmark fMRI Study for Versatile Haptic Interfaces

Summary. *Methods for evaluating magnetic resonance (MR)-compatibility of novel haptic interfaces for functional magnetic resonance imaging (fMRI) studies are well established. However, in order to obtain fMRI data that corresponds to natural human motions, the haptic interface has to allow these natural motions of the subject. This might be hindered by the number of degrees of freedom (DoF), joint limits or other technical constraints of the haptic interface. Moreover, the quality of the rendered haptic and virtual environment has to be sufficiently realistic such that cerebral activations are similar to the ones obtained in a real-world scenario. Up to now, there is no benchmark fMRI study for further validation of MR-compatible haptic interfaces that allows to clarify these dubieties. In this chapter, we present and carry out such a benchmark study with a grasp-and-lift scenario of virtual and real-world objects. The study exploits the capabilities of versatile haptic interfaces to a large extent, but can already be employed for a haptic interface featuring only two DoF. Using the obtained fMRI data as well as objective measures, the suitability of versatile MR-compatible haptic interfaces for fMRI studies is quantified on a common ground.*

5.1 Introduction

MR-compatible haptic interfaces [6, 11, 18, 19] create the opportunity to control the experimental conditions of human motor control studies using fMRI. Moreover, they allow recording data such as velocities or applied forces with great level of detail. There are interfaces for translational movements [19], interfaces for rotary movements [6, 18] as well as pinch-grasp interfaces [11]. The MR-Octo combines these capabilities and thus, has the ability to render a broad variety of experimental conditions in human motor control studies. This includes grasp-and-lift as well as reach-and-grasp tasks. More such versatile MR-compatible haptic interfaces, using different actuation technologies and kinematics, are likely to come up in the future [94].

The methods for MR-compatibility validation of the devices are well established [6,11,18]. They cover the measurement of radio frequency (RF) noise, the verification of the absence of field distortions in the static magnetic field, and the scan for artifacts in the echo planar images (EPIs) in ON and OFF mode of the devices. Moreover, sensor and actuator signal distortions are quantified to ensure that the devices can operate during fMRI.

However, in order to obtain data during an fMRI study that corresponds to natural human motions, MR-compatibility of the haptic interface is a necessary but not sufficient requirement. The quality of results can be impaired by an unnatural motion of the subjects during the use of a haptic interface. This might be provoked by restrictions in terms of DoF, by unnatural hand or arm postures, or by the quality of the rendered impedance of the device.

Until now, there is no standard fMRI procedure that allows verifying to which extent brain activations that are recorded while using a haptic interface to manipulate virtual objects differ from activations when manipulating corresponding real objects. Other research groups e.g. validated their MR-compatible haptic interface by showing the reproducibility of brain activations during its use [94]. To do so, comparable motions were repeated several times using the haptic interface. These motions included planning, reaching, and visually guided trajectory tracking in three DoF. Another attempt to show the validity of an fMRI study with a haptic gripper was to reproduce results from literature [11]. The study revealed two correlations, consistent with literature on grasping studies: First, a linear correlation of grip force with activations in the contralateral primary motor and somatosensory cortices (M1, S1), and bilaterally in the secondary somatosensory cortex (S2) as well as the supplementary and cingulate motor areas (SMA, CMA). Second, another linear correlation between the grip stiffness and the activations in the contralateral inferior parietal cortex (IPC), the intraparietal sulcus (IPS) and the dorsal premotor cortex (PMd), as well as the bilateral frontal gyrus (FG) was found.

However, we argue that results obtained while using a haptic interface could be repeatable but not natural and that results from literature can only be used as a comparison to a certain extent. Brain activations may differ depending on physiological differences between subjects, properties of the MR scanner, and other setup and task-specific parameters. We strive to establish a benchmark fMRI study that allows comparing results obtained when using a haptic interface to manipulate rendered objects to results when manipulating real-world objects. This study should be applicable to a broad range of haptic interfaces, such that performance comparisons and improvements are possible. We choose the study of grasping and lifting, since the opportunities are threefold: First, the study of grasp-and-lift tasks allows simulating a natural motion in seven DoF, but can already be used to benchmark haptic interfaces featuring only two DoF. Second, a real-world object in the study gives us the opportunity to adjust parameters such as load forces and measure the resulting grip force via attached sensors. Hence, not only fMRI data but also behavioral data, i.e. grip forces, can be used to evaluate the correlation between the two scenarios. Third, grasp-and-lift tasks in fMRI have already been investigated without haptic interfaces and thus, their study is well established. This means we do not venture into unknown territory in the field of motor neuroscience.

In literature, numerous studies have already documented regions that are participating in grasp-and-lift tasks [95–98]. Ehrsson et al. [95], as well as Kuhtz-Buschbeck et al. [96] found that activation of motor areas increases with the demand of a task and not merely with the force that has to be applied. As an example, they used an object of 200 g equipped with MR-compatible force sensors that had to be lifted with different grip strengths. Lifting the object and holding it with just enough force such that it does not slip, led to most activation in the M1, the left ventral premotor cortices (PMv), the left inferior parietal cortex and the cortex on the medial surface of the frontal lobe. Kawato et al. [97] was interested in neural mechanisms that reveal the location of internal models in the human brain. These models mimic input-output or output-input relations of motor tasks and forward models predict sensory information, resulting from motor activity. Kawato et al. used the grip force-load force coupling as an example, since the grip force modulation is anticipatory and is adapted, before changes in load force occur. Chouinard et al. [98] used a set of objects of different size, weight and density that needed to be lifted. The goal was to detect areas in the human brain that code for these properties. He found that the M1 adapted to the weight of the objects, whereas the left PMv adapted to the density of the objects, and the parietal and temporal cortex adapted to the size of the objects. The studies have already revealed a range of mechanisms and regions related to human motor control during grasp-and-lift tasks. Thus, the results of a comparable study can not only be used for quantitative verification of a novel haptic interface, but can also be discussed qualitatively.

In this work, we propose a study, where an object with different weight levels is grasped with a two finger pinch grip and lifted along its vertical axis. The study is carried out both with a haptic interface and with a corresponding benchmark real-world object. The correlation of the brain activations between the two experiments along with behavioral measures, i.e. grip forces, gives us a means to quantify how well results obtained with MR-compatible haptic interfaces can be generalized to real object manipulation.

The remainder of this chapter is organized as follows: In Section 5.2, we establish the study hypotheses. In Section 5.3, the experimental setup is explained. Section 5.4 details the study design and experimental procedures, whereas Section 5.5 presents the results of behavioral and fMRI data. Finally, the results are discussed in Section 5.6 and a conclusion is drawn in Section 5.7.

5.2 Study hypotheses

We hypothesize that the better the visual and haptic rendering, the stronger the correlation of both cerebral activations and behavioral measures, i.e. grip forces, between the two cases of virtual grasp-and-lift (virtual G&L) with a haptic interface and benchmark grasp-and-lift (benchmark G&L) with a real-world object. The correlation of cerebral activation can be quantified by measuring the overlap of voxels in the fMRI data, whereas the correlation of behavioral measures can be determined from force sensor measurements.

Moreover and in order to raise the robustness of the benchmark, the weight of the objects is varied. The weight of the objects correlates with the applied grip force. We hypothesize that the correlation of cerebral activations as well as behavioral measures, i.e. grip forces, between the two cases of benchmark G&L and virtual G&L holds under such a change of variable. Any correlation between cerebral activations and object weight should be apparent both in virtual G&L and benchmark G&L.

5.3 Experimental Setup

The fMRI study consists of two experimental setups in the MR scanner: The first one is the benchmark scenario that allows conducting the experiment with a real-world object. The second one allows conducting the same experiment with a haptic interface, i.e. the MR-Octo.

5.3.1 Benchmark grasp and lift scenario

The benchmark scenario is shown in Figure 5.1. A subject is lying supine position in the MR scanner, the head is inside a head coil and the right hand is holding an object, using thumb and index finger. The forearm is supported by cushions such that the rest position can be held without any effort. Via a mirror mounted on the head coil, the subject can see the benchmark object that is depicted in detail in Figure 5.2.

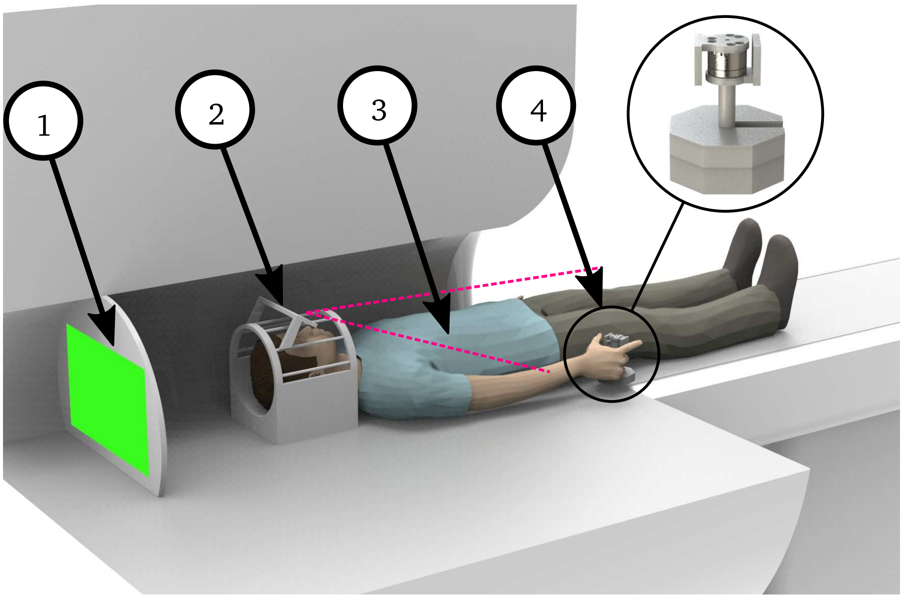

Figure 5.1: Experimental setup, shown in a sliced MR scanner: (1) screen that illuminates the scanner bore in red or green, (2) head coil with mounted mirror, (3) subject lying in supine position, (4) benchmark object.

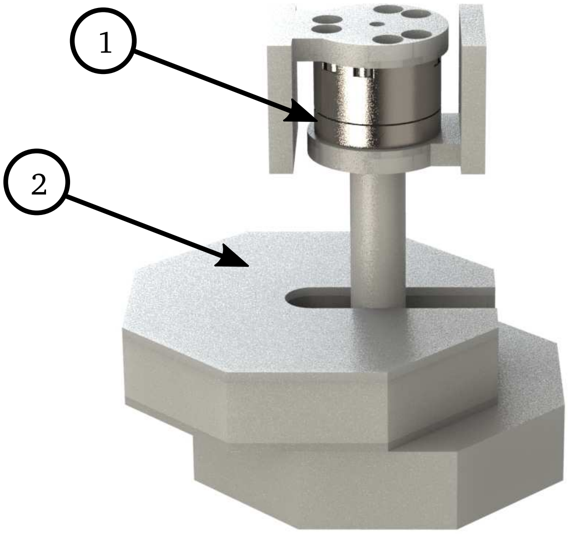

Figure 5.2: CAD rendering of the benchmark object with (1) force sensor at the top and (2) exchangeable weights that can be pulled off.

The subject grasps the object with thumb and index finger at two vertical plates at the upper part. This ensures that grip width and grip position are the same for all objects. The benchmark object is equipped with a force sensor, a Mini27 Titanium from ATI IA, that allows recording the grip forces during lifting. A screen in the back of the scanner is illuminated green, when the subject should carry out the movement and red, when the subject should rest. This screen illuminates the entire scanner bore such that it is easily perceivable when to start and end each trial.

An assistant sets the weight of the object to one of the four different levels for every new trial. The weight level is indicated by the number of octagonal plates at the bottom of the object. We encode the objects with $1-4$. Object 1 features one plate and is the lightest with 100 g. Each further level adds another 100 g.

5.3.2 Haptic interface MR-Octo

The experimental setup with the MR-Octo is depicted in Figure 5.3. For the presented setup, all axes of the MR-Octo, except for vertical motions and grasping, are blocked. This allows a higher controllability of the study. It is triggered by the fact that subjects are not able to perceive the depth in the virtual environment as they would in the real world. Thus, finding the correct position for a grasp is more challenging than in the real-world scenario. In order to simplify the task, the DoFs are limited. Consequently, the number of successful trials rises, compared to using all seven DoF.

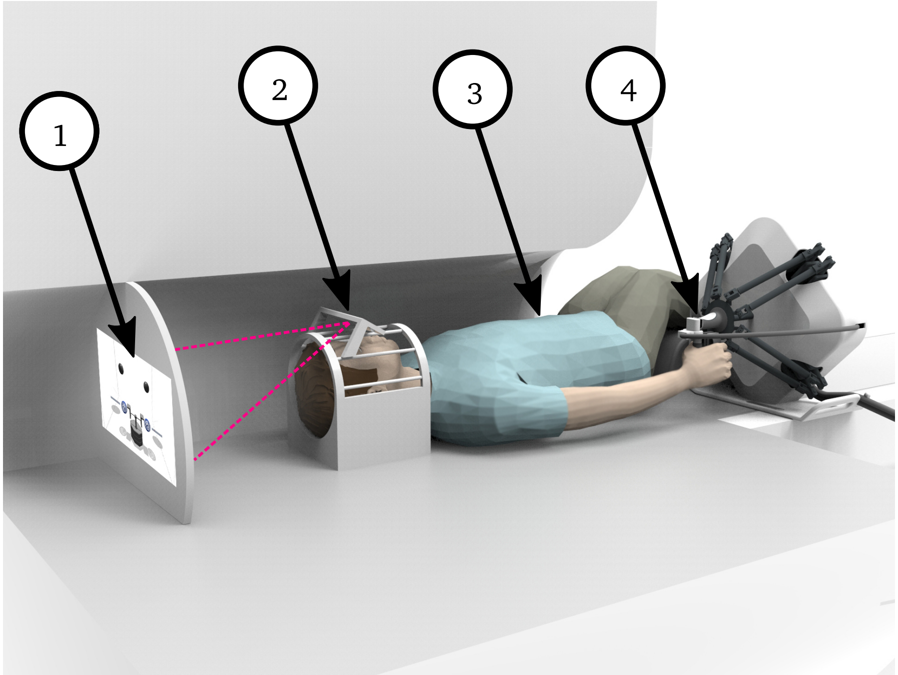

Figure 5.3: Experimental setup, shown in a sliced MR scanner: (1) screen with projected virtual reality, (2) head coil with mounted mirror, (3) subject lying in supine position, (4) haptic interface MR-Octo.

In this setup, the subject is again lying in supine position in the MR scanner with the head inside a head coil and the forearm as well as the legs supported by cushions. The right hand of the subject holds the gripper of the haptic interface with thumb and index finger. A projector, located outside the MR scanner room, projects a virtual environment onto the screen inside the scanner. Via the mirrors mounted on the head coil, the subject can see this virtual environment.

The virtual environment itself is shown in Figure 5.4. Like in the real-world scenario, virtual objects of four different weight levels are rendered. The level is again indicated by the number of octagonal plates at the bottom of each object. Grip width and weight are the same as for the benchmark object.

During manual control, the haptic interface can be switched on by the subject, using a switch at the gripper. The color of the rest positions indicates if the haptic interface is running: Green means it is turned on, red means it is turned off. During automatic control and during the experiments, the haptic interface is turned on and off without user intervention. Thus, comparable to the setup with the benchmark object, the color signals the start and end of each trial to the subject.

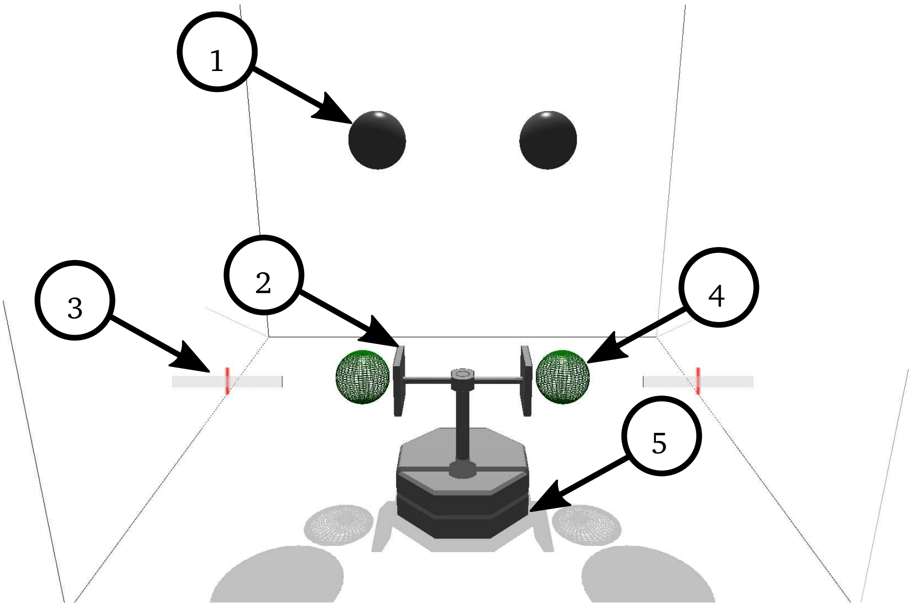

Figure 5.4: Virtual Environment showing (1) finger tip representations, (2) virtual object, (3) grasp force level bars, (4) rest positions, and (5) weight level indicated by the number of octagonal plates.

By moving the haptic interface, the subject guides an avatar, i.e. two representations of his fingertips, through the virtual environment. First, the subject moves to the rest position and then grasps the virtual object. But shear forces at the fingertips cannot be rendered by the MR-Octo and the grasp force level has to be controlled visually via two level bars. This is a main difference to benchmark G&L, where the subject can feel the object slip. Again similar to benchmark G&L, the heavier the object, the more force has to be applied such that the object does not slip. In order to avoid that the subject grasps each object with maximum force, due to the missing shear force sensation, a maximum grasp force level has to be set for each object. The maximum force that can be applied per object, is indicated by a vertical red line in the level bars. If the force exceeds the maximum level, the object disappears and the contact force is set to zero. This behavior is comparable to a fragile object that is crushed under excessive force. Consequently, there is a force range for each object such that it can be lifted off the ground.

5.4 Study design and experimental procedure

The study features a 2 × 4 within-subject design: Each subject carries out virtual G&L with the haptic interface as well as benchmark G&L with a real-world object. Four levels of weight are employed in both scenarios. The weights appear in a pseudorandomized order and their relative occurrence is counterbalanced.

The experimental procedure is as follows: Thumb and index finger of the subject start from a rest position close to the benchmark or virtual object. From there, the object is grasped and lifted off the ground along a vertical axis. During training with the virtual object, a reference movement is shown with a wire-frame model of the object, i.e. a transparent copy of the virtual object where only the edges are visible. It indicates optimal lifting height and velocity and ensures that comparable speeds and heights are achieved for each object and by each subject. The object is then lifted accordingly and placed on the ground again. To finish a trial, the operator moves back to the rest position. After training and during the actual execution of the trials, no feedback of lifting height and velocity is shown. The sequence of the experiment in the virtual environment is depicted in Figure 5.5.

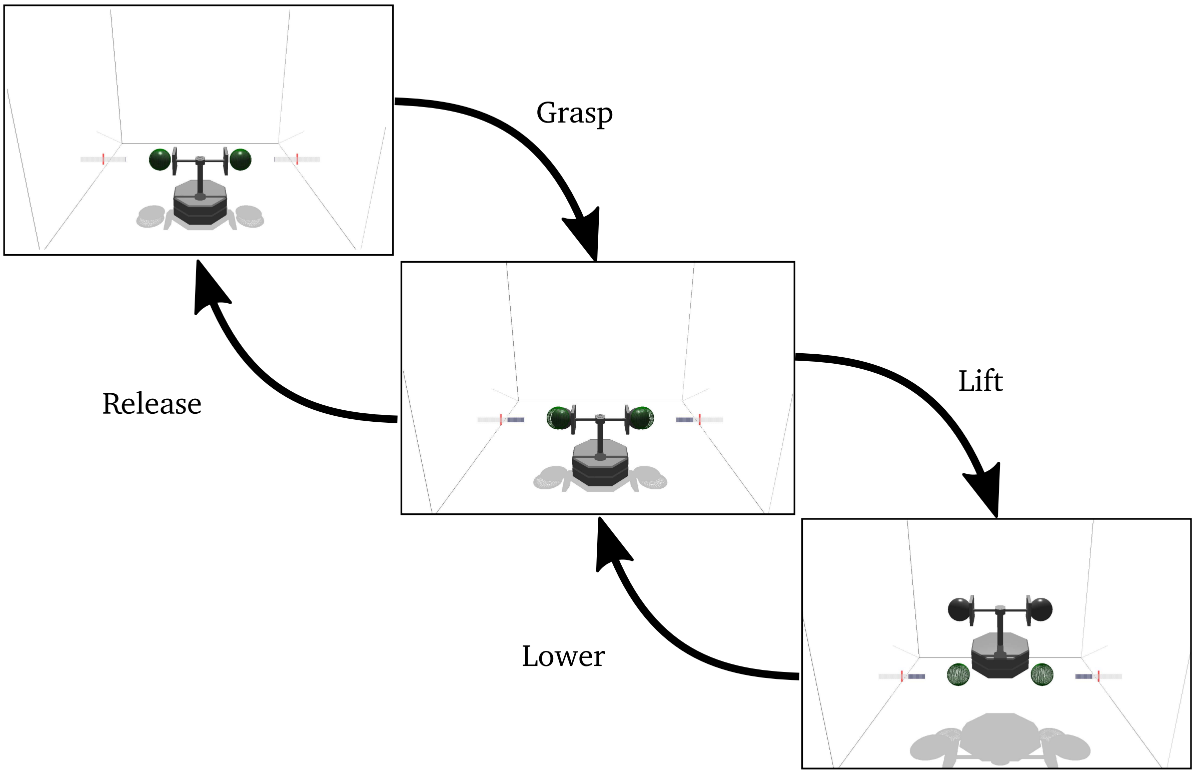

Figure 5.5: Sequence of the grip-and-lift experiment.

The subject trains grasping and lifting objects in supine position outside the MR scanner until it is comfortable using the haptic interface and the benchmark object. This ensures that motor learning has already reached a steady state before starting the actual study. On a separate day, about one hour of trials is carried out inside the MR scanner. Each trial then has a duration of 18 s, whereas the grasp-and-lift movement takes only 2 s, which is the duration of one TR. In order to facilitate the start at t=0 s of each trial as well as adapting the object weight of the real object by the assistant, the objects are presented 4 s before and the start signal is given 300 ms before. The haptic interface is turned on automatically for 4 s, which gives the subjects enough time to go back to the rest position, even in the case of a failure of any kind. The subject then carries out 32 trials and the object weights are pseudo-randomized. After these 9.6 min of trials, the subject can rest for another 1.5 min before the next run starts. At least three runs and as many runs as comfortable for the subject are repeated, before the experiment finishes. If an object is grasped too firmly, or the subject slips off, the trial is discarded.

5.5 Results

The study was approved by the ethics committee of the Eberhard-Karls University as well as the university hospital Tübingen and the two subjects gave their informed consent. Subject one was left-handed, but highly trained on the MR-Octo.

5.5.1 MRI preprocessing and analysis

All imaging tests were performed on a 3 T MRI system (Prisma, Siemens; Erlangen, Germany) equipped with a 20-channel head coil. For the functional imaging we employed gradient echo (GRE) echo-planar sequences (EPI) with the following parameters: TR = 2 s, TE = 30 ms, FOV = 210 × 210 mm^3, flip angle = 74 deg, voxel size = 2.5 × 2.5 × 2.5 mm^3 and 50 slices to achieve whole brain coverage.

Subject one carried out eight runs of virtual G&L and six runs of benchmark G&L. Subject two conducted three runs of virtual G&L and six runs of benchmark G&L. Each run consisted of 300 EPI BOLD volumes and contained 32 trials.

Preprocessing and analysis of the fMRI data has been done with SPM12 implemented in Matlab R2014b. We realigned all functional data with a two-pass procedure for each participant and calculated a mean EPI scan for each participant. The respective T1 scan has been coregistered to the mean functional scan. We normalized the coregistered T1 scan to MNI space using the unified segmentation and normalization approach as implemented in SPM12. Deformation fields calculated for the normalization of the individual T1 scans have then been applied to all functional scans, reconstructing images with an isotropic resolution of 2 × 2 × 2 mm^2. Finally, all functional scans have been smoothed with a full width at half maximum of 4 mm. For a voxel-wise whole-brain analysis, we fitted a general linear model (GLM) to the measured data with arm and hand movement as first regressor of interest. Measured peak grip forces for each trial were used to create a second regressor of interest capturing linear signal modulations of the mean arm movement signal, which is estimated by the first regressor. Trials with movement errors were modeled separately, creating a regressor of no interest. We also included six motion parameters from realignment to control for residual movement artifacts. Finally, a stick function indicating the periods of movement execution was used to capture any systematic noise signals caused by the mass of the arm moving through the field. Session-specific signal offsets have been modeled with constant regressors for each session. We explored the data of the participants using linear contrasts to combine regressor weights after estimation and calculated voxel-wise t-maps within each participant. Please note that we used different type-1 error probability thresholds and cluster extent thresholds to inspect the topography of signal changes for each participant, experimental conditions and behavioral parameters.

5.5.2 Behavioral data

The results of the behavioral data cover grip forces, recorded with the benchmark object, as well as grip and lift forces generated with the haptic interface. Since the vertical plates, where the benchmark object is grasped, are located above and below the force/torque sensor, as can be seen in Figure 5.2, no lift forces could be recorded. However, they can be expected to be comparable to the ones recorded with the haptic interface. Only results of one subject are reported, but the differences to the results of the second subject are detailed.

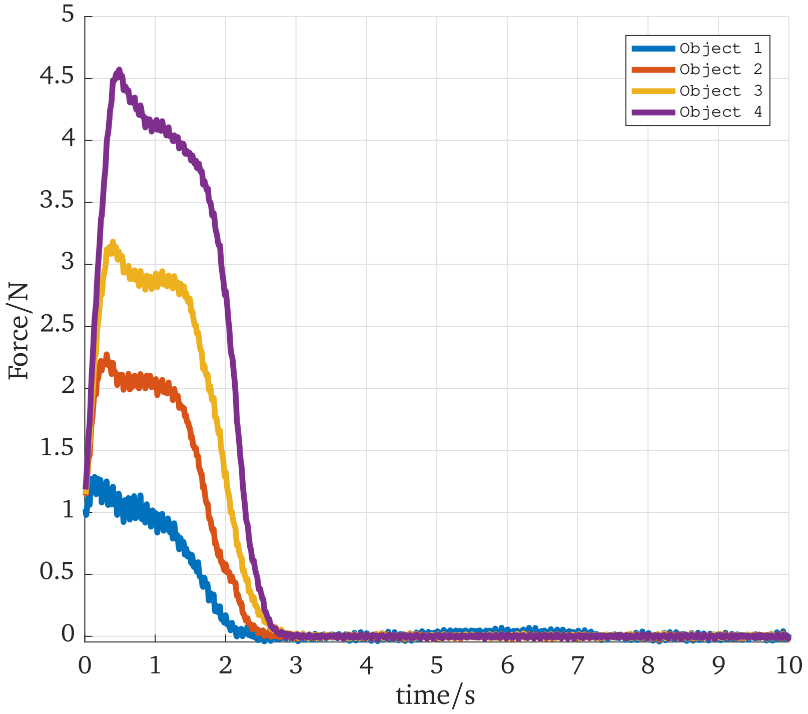

Figure 5.6: Mean of the grip forces with the benchmark object over time for all objects and one subject.

Benchmark grasp-and-lift

The mean values of the grip forces, recorded with the benchmark object, for all objects and of the first subject are depicted in Figure 5.6. The correlation between grip force and weight level is clearly visible. This correlation also holds for the second subject, even though grip forces are about three times larger at all weight levels.

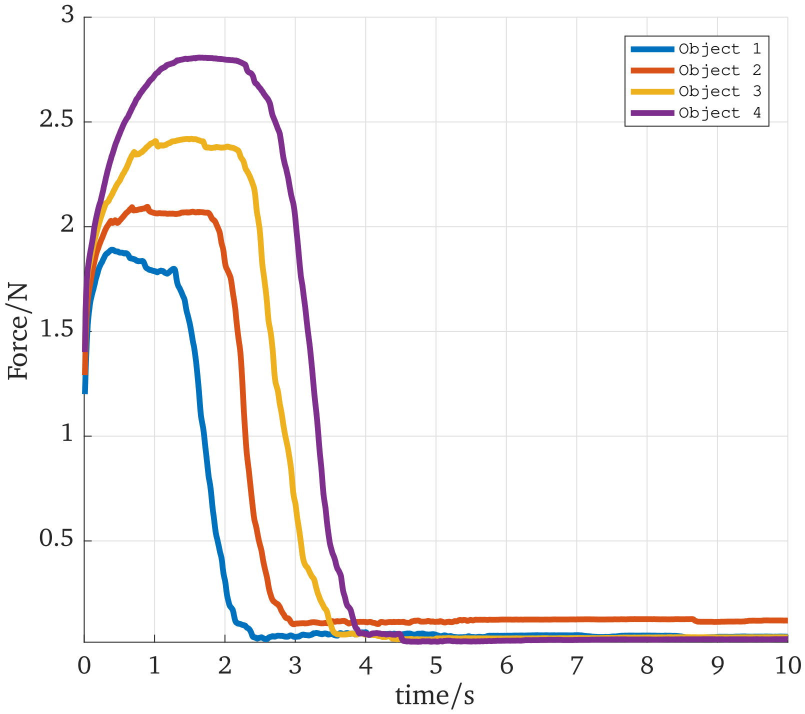

Figure 5.7: Mean of the grip forces with the haptic interface over time for all objects and one subject.

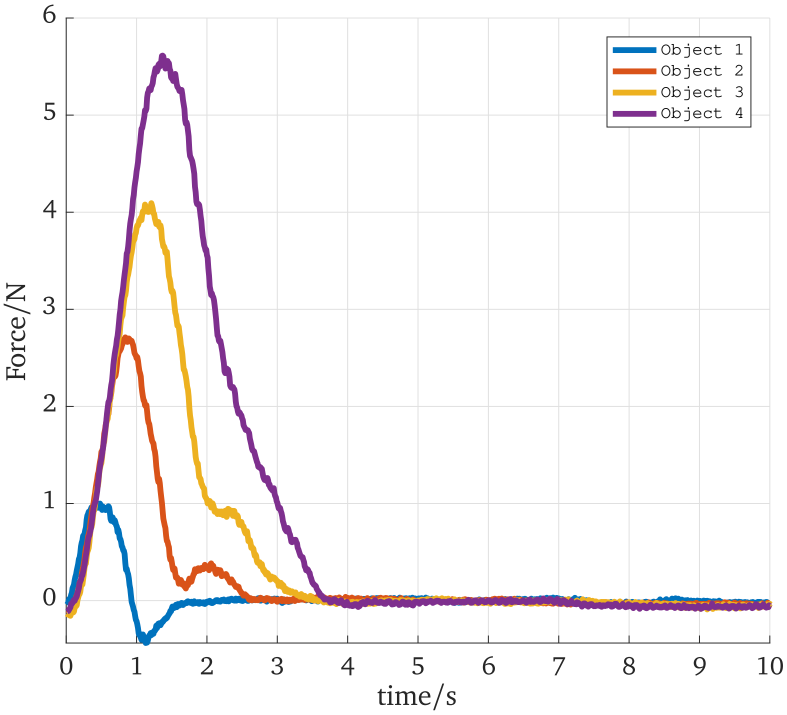

Figure 5.8: Mean of the lift forces with the haptic interface over time for all objects and one subject.

Virtual grasp-and-lift

The mean values of the grip forces recorded with the MR-Octo, for all objects and of the first subject are depicted in Figure 5.7. The correlation between grip force and weight level is again clearly visible, even though the overall levels are smaller.

The haptic interface also recorded the lift forces. The mean values of the lift forces with the haptic interface, for all objects and of the first subject are depicted in Figure 5.8. The levels of grip and lift forces, recorded while using the haptic interface, are similar for both subjects.

5.5.3 fMRI analysis

We report results of the fMRI analysis for one subject. Again, differences to the results of the other subject are detailed.

Overlap of virtual and benchmark grasp-and-lift

Figure 5.9 shows the activations of the first subject during virtual G&L in red, the activations of benchmark G&L in blue, and the overlap of the voxels in magenta. The sensomotoric areas are activated in both cases and a large overlap in terms of voxels can be identified.

Results obtained from the second subject also show a large overlap, but more extended clusters for the case of benchmark G&L.

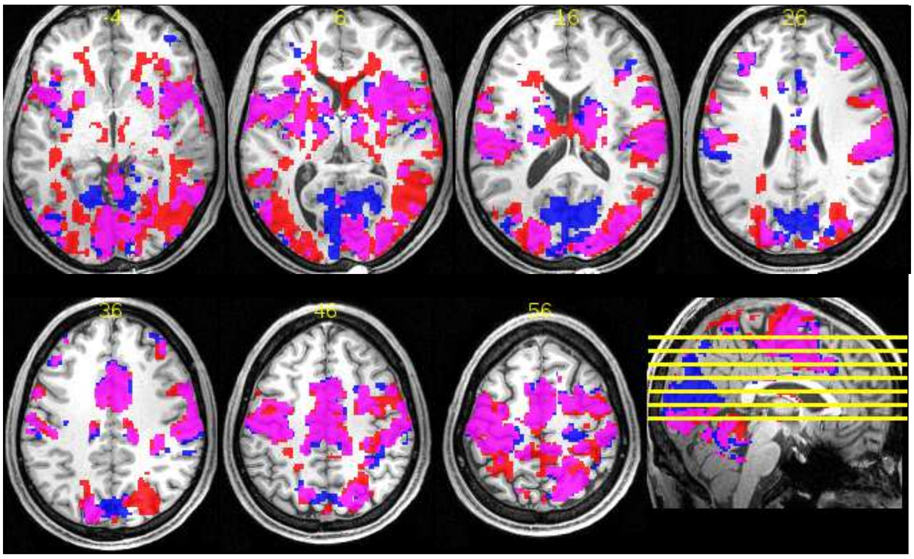

Figure 5.9: Activations related to virtual G&L (red), activations related benchmark G&L (blue), and the overlap of both cases (magenta).

Differences between virtual and benchmark grasp-and-lift

Figure 5.10 depicts the differences between virtual and benchmark G&L. Red areas are regions where activations of virtual G&L are stronger than of benchmark G&L. Blue areas are regions where activations of virtual G&L are weaker than of benchmark G&L. The M1 in both hemispheres as well as the medial visual cortex show stronger activations in the case of benchmark objects. The lateral visual cortex on the other hand is more active in the case of virtual G&L.

The same findings apply to the second subject, whereas there are less differences in the visual system.

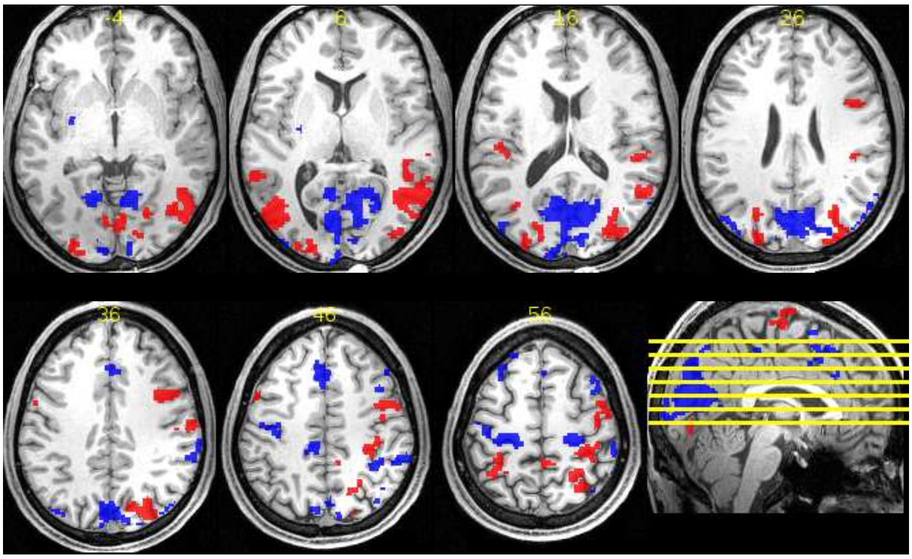

Figure 5.10: Differences between virtual and real G&L for two cases: Activations of virtual G&L are stronger than of benchmark G&L (red). Activations of virtual G&L are weaker than of benchmark G&L (blue).

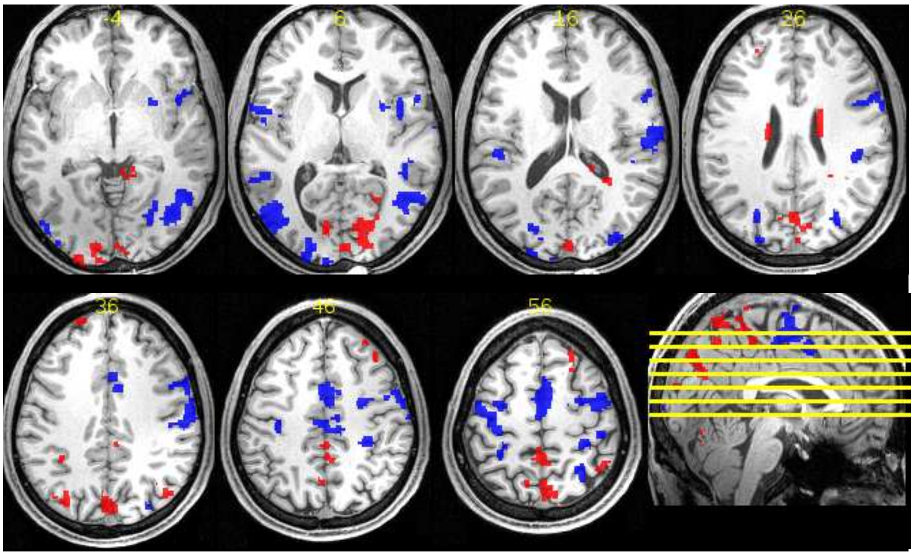

Figure 5.11: Linear modulation of activation with the grip force during virtual G&L: Regions with a higher activation in the case of higher grip force are shown in red, regions with a weaker activation in the case of increasing grip force are shown in blue.

Linear modulation of activation with grip force in the case of virtual grasp-and-lift

Figure 5.11 depicts regions that show a linear modulation of their activation with the grip force in the case of virtual G&L. Regions with an increasing activation in the case of higher grip force are shown in red. Regions with a decreasing activation in the case of stronger grip force are shown in blue. Decreasing activation for higher grip forces can be found in the M1 and the medial SMA.

However, this finding does not apply to the second subject, where no significant linear correlations were found. Moreover, no significant correlations could be found in the case of benchmark G&L for both subjects.

5.6 Discussion

The presented study is designed to quantify in how far an MR-compatible haptic interface can render a visual and haptic environment that leads to similar cerebral activations as a real-world scenario. This gives us a means to quantify how well results obtained with an MR-compatible haptic interface can be generalized to real object manipulation. Thus, we built two setups with a haptic interface and with a benchmark real-world object.

The behavioral data show the expected outcome for both subjects: The heavier the objects, the more grip force is applied during virtual G&L as well as benchmark G&L. The load force of the benchmark object is not measured online, but is expected to be comparable to the one measured by the haptic interface. Interestingly, the overall time of one trial is longer during virtual G&L and the peak of maximum grip force appears later than during benchmark G&L. Most likely, the mostly visual adjustment of the grip force in the virtual environment, using the level bars, is more challenging and thus, takes longer than tactile force adjustment.

The correlation of the activations in the sensorimotor system for the case of virtual G&L as well as benchmark G&L, as shown in Figure 5.9, indicates that both tasks activate the same areas in the sensorimotor system. This is in support of our first hypothesis that postulates that the better the visual and haptic rendering, the more overlap in terms of voxels should be apparent in the fMRI data. The large overlap is in favor of the quality of the rendered virtual environment, but in order to prove the hypothesis, different levels of quality of visual and haptic environment would have to be rendered. This should then lead to different levels of overlap in the fMRI data.

However, quantitative differences remain for the case of virtual and benchmark G&L with stronger signals in the motor cortex for benchmark G&L. Interestingly and for both subjects, this provides some indication that coordination is more challenging in the case of benchmark G&L. Conversely it means that virtual G&L is simpler. It might result from the limited DoF of the haptic interface that restrict the possible motions, which makes it easier for the motor cortex to manipulate objects during virtual G&L.

On the other hand, the visual cortex is more active in the case of virtual G&L, as depicted in Figure 5.10. Hence, grasping and lifting virtual objects demands more visual data processing. This results most likely from the fact that force is mainly controlled visually using the level bars in the virtual environment. Visual force control is necessary to set the grip force to the right level such that the object does not slip. As reported before, shear forces cannot be rendered by the haptic interface, which makes it impossible to feel an object slip.

The linear modulation of cerebral activation with grip force in the case of virtual G&L, as depicted in Figure 5.11, and its absence during benchmark G&L contradicts our second hypothesis. This hypothesis postulates that any correlation of cerebral activation with grip force should hold for the two cases of benchmark G&L and virtual G&L. On the other hand, this effect did not occur in case of the second subject which is in favor of our hypothesis. Hence, data from more subjects should be collected in order to further clarify this issue.

5.7 Conclusion

We presented a design for a benchmark fMRI study for versatile MR-compatible haptic interfaces. The study is designed for devices that allow at least grasp and lift motions in an MR scanner. It was carried out with the MR-Octo that has seven DoF and of which two DoF were used. Behavioral results show a similar trend for the two scenarios of virtual and benchmark G&L. But especially fMRI data, while still showing large overlaps, they also indicate some differences in the activations of visual and motor cortex. These differences on the one hand leave room for technological improvements of the MR-Octo, but on the other hand show that results obtained with MR-compatible haptic interfaces need to be interpreted with care when aiming for a generalization to natural grasp and lift movements. The introduced and presented procedure can be used to quantify technological improvements and help interpreting obtained results in the context of primary effects aimed to be studied and secondary effects introduced by the employed haptic interface and setup.

Future work should address extending the number of subjects and tasks, in order to provide statistical significance. Further tasks could e.g. be in a cascaded setup that allows determining an overall performance measure. Moreover, objective measures should be introduced for an evaluation of the fMRI data, including an objective definition of the sensorimotor areas.

6 Conclusions and Future Directions

6.1 Concluding remarks

In this work, a novel MR-compatible haptic interface with seven DoF was presented. It constitutes a landmark in the design of MR-compatible haptic interfaces, since complex tasks involving natural, unconstrained pick-and-place motions can finally be targeted for investigation. This extends the types of questions in the field of visuomotor control that can be asked by neuroimaging. Moreover, the presented haptic interface allows shifting the paradigm when moving on to a new research question from redesigning new devices to reprogramming a single device.

In Chapter 2, we focused on the control strategy for rotary traveling wave ultrasonic motors (USMs) that actuate the haptic interface. These friction-based actuators are MR-compatible, compact, and generate high torques. However, they usually cannot realize low velocities and dead zones appear under load. Both issues are relevant, since low velocities occur frequently during haptic applications and the operator as well as the rendered impedance generate a varying load. As a first step in the development, a second-order model that reproduces dead zone effects was established and identified using experimental data from a testbed. The model incorporates the possibility of altering the velocity via an adjustment of the frequency of the traveling wave as well as by varying the phase difference of the underlying standing waves. The control of the phase difference is not possible for commercial USMs and required a customization of the motor drivers. Using this phase difference control, low velocities could be realized. Based on the model and using the customized motor drivers, a hybrid sliding mode controller (SMC) was developed that generates low velocities and copes with dead zones. It leads to two control domains of frequency control and phase difference control. A key aspect of the controller is that it does not require a digital implementation of a signum function that usually leads to chattering effects of SMCs. These effects could be avoided by identifying the signum function as a part of the motor model. Moreover, we showed that the controller provides global uniform asymptotic stability (GUAS) for bounded disturbances in both domains and that switching in between the control domains is smooth and thus, cannot be felt by the operator of a haptic interface. Finally based on a series of performance indices, we showed that the controller performs better than a hybrid SMC/P or a dual $H\infty$ controller that have been proposed in literature.

In Chapter 3, we systematically developed a novel Octopod kinematics that determines the robotic structure of our MR-compatible haptic interface. We compared existing parallel kinematics with rotary actuators and six legs within a selection process and using a range of dynamic as well as kinematic performance criteria. The best-performing solution was determined, but it still suffered from a typical issue of parallel kinematics, the so-called direct kinematic singularities. These singularities lead to uncontrollable DoF at the end effector and thus, restrict the dexterous workspace. We overcame this issue by presenting a redundant extension to the best-performing solution – the Octopod kinematics. Additionally, we proposed a comprehensive algorithm that allows determining the output capabilities of actuation-redundant parallel kinematics and showed that the Octopod outperforms other kinematics with six legs in terms of worst-case force, torque, and acceleration. Finally, the kinematics was realized as a non-MR-compatible prototype and its worst-case output capabilities and stiffness were determined experimentally.

In Chapter 4, the results from the previous chapters, namely control and kinematics were combined. This resulted in the first MR-compatible haptic interface with seven DoF for fMRI studies in the field of human motor control – the MR-Octo. The system endows neuroscientists with a tool that can be reprogrammed and does not have to be redesigned when moving on to a new research question. In order to ensure that the system is both safe as well as ergonomic and can be applied for fMRI studies, a human factors analysis was carried out. Then, a prototype of the haptic interface was realized and the MR-compatibility was verified. To this end, the MR-Octo was introduced into an MR scanner and field distortions, RF noise, and impacts of the magnetic field on sensors as well as actuators were quantified. From the results, we confirmed the MR-compatibility of the MR-Octo at the entry of the scanner bore of a 3 T MRI system (Prisma, Siemens; Erlangen, Germany).

In Chapter 5, we presented a benchmark fMRI study for MR-compatible haptic interfaces. Since the quality of results obtained during an fMRI study and the use of a haptic interface can be impaired by an unnatural motion of the subjects, the suitability of such haptic devices needs to be quantified. To this end, we designed a study with a grasp-and-lift scenario. The study allows comparing the fMRI data obtained using a haptic interface to manipulate virtual objects to the data obtained when manipulating real objects. The validation is designed for devices that allow at least grasp and lift motions in an MR scanner. In this work, it was carried out with the MR-Octo that features seven DoF and of which two DoF were used. A benchmark object with different levels of weight and a force sensor allowed to set up a benchmark scenario. The results from the behavioral data as well as fMRI data indicate that the haptic interface can render a virtual environment comparable to the use of a benchmark object. However, quantitative differences remain in the activation of the sensorimotor system and hence, leave room for technological improvements on the MR-Octo. In the future, the improvements can again be quantified using the presented study.

6.2 Outlook

Based on the topics in this thesis, several future research questions arise. They concern the model validity and life-time prolongation of USMs as well as a performance improvement in Octopod kinematics. Moreover, the MR-Octo endows neuroscientists with a new tool for research in the field of human motor control. Research questions regarding complex reach-and-grasp movements can now be targeted. The possibilities for future work are detailed in the following sections.

Life-time prolongation of USMs

The presented low-level position controller solves most of the challenges that arise when using USMs for a haptic interface, which are non-linearities, load-dependent dead zones, and realizing low velocities. However, the short life-time of USMs compared to DC motors remains a challenge. This is mainly due to an abrasion of the friction layer in the USMs. On one hand, this can be seen as a control challenge. Via a controller that exploits the non-backdriveablility of the USMs, they could be switched off at certain times. This would even produce a higher torque since the stall torque is higher than the continuous torque. Such a strategy could protect the friction layer from abrasion, because no traveling wave is produced during stalling. On the other hand, mechanical ways could be found to protect the friction layer or restore it. However, this probably lies within the field of material science, but would be worthwhile investigating, considering the high cost of USMs.

USM model validity under temperature changes

The presented model for USMs does not take into account temperature changes. The reason being that the operating conditions in haptic devices require only high load conditions for a short time when rendering contact. The motors run at low velocities and at minimal load conditions for most of the time when rendering free space. Hence, heating plays a much smaller role in haptic devices, compared to other applications where the motor drives at full speed and high load for most of the time. In the future and in order to make the model valid for other applications, it should be extended to reflect the temperature dependency.

Performance improvement of the Octopod via optimization

The length of the links of the Octopod kinematics were chosen in an iterative process that guaranteed the achievement of both workspace coverage and minimum output capabilities. Typically, a compromise between force/torque and velocity capabilities has to be made given a certain set of actuators. For the first prototype of the MR-Octo, no formal optimization was carried out and the link lengths were determined by the designer. In the future, precise tasks to be carried out in the MR scanner should be defined, including required output capabilities and workspace for every DoF. Then, a formal optimization could be carried out in order to further improve the performance of the MR-Octo for these specific tasks.

Performance improvement of the Octopod via control

The Octopod kinematics avoids direct kinematic singularities by design. However, it comes at the cost of an over-constrained end effector. More advanced control schemes that reduce parasitic forces will most likely improve the performance of a device with this kind of kinematics.

Benchmark fMRI studies with the MR-Octo

The benchmark fMRI study that was presented in this work should be expanded in order to cover more tasks and subjects. Then, statistical significant results can be obtained to quantify how well results obtained with MR-compatible haptic interfaces generalize to real object manipulation. Moreover, technological improvements for the MR-Octo can be identified in order to further improve the quality of the haptic and visual rendering.

Human motor control studies with the MR-Octo

Clearly, human motor control studies using fMRI and the MR-Octo are a novel research topic, worth investigating. Since the system is versatile but also comes with limitations in terms of output capabilities, tactile feedback, and workspace volume, studies have to be designed accordingly.

Bibliography

[1] N. Ward, M. Brown, A. Thompson, and R. Frackowiak, “Neural correlates of motor recovery after stroke: a longitudinal fmri study,” *Brain*, vol. 126, no. 11, pp. 2476–2496, 2003.

[2] D. D. Cox and R. L. Savoy, “Functional magnetic resonance imaging (fmri) brain reading: detecting and classifying distributed patterns of fmri activity in human visual cortex,” *Neuroimage*, vol. 19, no. 2, pp. 261–270, 2003.

[3] J. C. Culham, C. Cavina-Pratesi, and A. Singhal, “The role of parietal cortex in visuomotor control: what have we learned from neuroimaging?,” *Neuropsychologia*, vol. 44, no. 13, pp. 2668–84, 2006.

[4] R. Gassert, E. Burdet, and K. Chinzei, “MRI-Compatible Robotics.,” *IEEE engineering in medicine and biology magazine : the quarterly magazine of the Engineering in Medicine & Biology Society*, vol. 27, no. 3, pp. 12–4, 2008.

[5] M. Flueckiger, M. Bullo, D. Chapuis, R. Gassert, and Y. Perriard, “fMRI compatible haptic interface actuated with traveling wave ultrasonic motor,” in *Fourtieth IAS Annual Meeting. Conference Record of the 2005 Industry Applications Conference, 2005.*, pp. 2075–2082, 2005.

[6] I. Farkhatdinov, A. Garnier, and E. Burdet, “Development and evaluation of a portable MR compatible haptic interface for human motor control,” *2015 IEEE World Haptics Conference (WHC)*, pp. 196–201, 2015.

[7] R. Riener, T. Villgrattner, R. Kleiser, T. Nef, and S. Kollias, “fMRI-Compatible Electromagnetic Haptic Interface.,” in *IEEE Engineering in Medicine and Biology Society Conference*, 2005.

[8] A. Khanicheh, A. Muto, C. Triantafyllou, B. Weinberg, L. Astrakas, A. Tzika, and C. Mavroidis, “fMRI-compatible rehabilitation hand device.,” *Journal of neuroengineering and rehabilitation*, vol. 3, p. 24, 2006.

[9] S. J. Kim and J. Kim, “MR-compatible hand exoskeleton for monitoring brain activity during active assistance,” *Proceedings of the Annual International Conference of the IEEE Engineering in Medicine and Biology Society, EMBS*, pp. 5752–5755, 2015.

[10] N. Yu, C. Hollnagel, A. Blickenstorfer, S. Kollias, and R. Riener, “fmri-compatible robotic interfaces with fluidic actuation,” *Robotics: Science and Systems IV, Zurich, Switzerland, June*, pp. 25–28, 2008.

[11] B. Vigaru, J. Sulzer, and R. Gassert, “Design and Evaluation of a Cable-Driven fMRI-Compatible Haptic Interface to Investigate Precision Grip Control,” *IEEE Transactions on Haptics*, vol. 1412, 2015.

[12] J. Diedrichsen, Y. Hashambhoy, T. Rane, and R. Shadmehr, “Neural correlates of reach errors.,” *The Journal of Neuroscience*, vol. 25, no. 43, pp. 9919–31, 2005.

[13] L. Dovat, R. Gassert, D. Chapuis, G. Ganesh, E. Burdet, and H. Bleuler, “A Haptic Interface Based on Potential Mechanical Energy to Investigate Human Motor Control using fMRI.,” *International Conference of the IEEE Engineering in Medicine and Biology Society*, vol. 5, pp. 5021–4, 2005.

[14] R. Gassert, L. Dovat, O. Lambercy, Y. Ruffieux, D. Chapuis, G. Ganesh, E. Burdet, and H. Bleuler, “A 2-DOF fMRI compatible haptic interface to investigate the neural control of arm movements,” in *IEEE International Conference on Robotics and Automation*, pp. 3825–3831, 2006.

[15] J. Izawa, T. Shimizu, H. Gomi, S. Toyama, and K. Ito, “MR compatible manipulandum with ultrasonic motor for fMRI studies,” in *IEEE International Conference on Robotics and Automation*, no. May, pp. 3850–3854, 2006.

[16] M. Hara, G. Matthey, A. Yamamoto, D. Chapuis, R. Gassert, H. Bleuler, and T. Higuchi, “Development of a 2-DOF electrostatic haptic joystick for MRI/fMRI applications,” in *IEEE International Conference on Robotics and Automation*, pp. 1479–1484, 2009.

[17] F. Kimura, a. Yamamoto, M. Hara, J. Ryu, H. Bleuler, and T. Higuchi, “System development of an admittance-controlled 2-dof haptic device using electrostatic motors,” *2011 IEEE World Haptics Conference*, pp. 263–268, 2011.

[18] F. Sergi, A. C. Erwin, and M. K. Omalley, “Interaction control capabilities of an MR-compatible compliant actuator for wrist sensorimotor protocols during fMRI,” *IEEE/ASME Transactions on Mechatronics*, vol. 20, no. 6, pp. 2678–2690, 2015.

[19] S. Klare, A. Peer, and M. Buss, “Development of a 3 DoF MR-Compatible Haptic Interface for Pointing and Reaching Movements,” in *Haptics: Generating and Perceiving Tangible Sensations*, pp. 211–218, 2010.

[20] S. Menon, H. Ganti, and O. Khatib, “Using Haptic fMRI to Enable Interactive Motor Neuroimaging Experiments,” in *Springer Tracts in Advanced Robotics: Experimental Robotics*, Springer Netherlands, 2014.

[21] S. Menon, A. Soviche, J. Mithrakumar, A. Subbarao, H. Ganti, and O. Khatib, “Haptic fmri: A novel five dof haptic interface for multi-axis motor neuroscience experiments,” in *World Haptics Conference (WHC), 2017 IEEE*, pp. 13–18, IEEE, 2017.

[22] A. Khanichehl, D. M. B. W. A. A. Tzika, and C. Mavroidisl, “MR_CHIROD v.2: A fMRI Compatible Mechatronic Hand Rehabilitation Device,” in *10th IEEEE International Conference on Rehabilitation Robotics*, 2007.

[23] M. A. Ergin, M. Kühne, A. Thielscher, and A. Peer, "Design of a New MR-compatible Haptic Interface with Six Actuated Degrees of Freedom," in *IEEE International Conference on Biomedical Robotics and Biomechatronics (BioRob)*, pp. 1–6, 2014.

[24] P. Fischer and R. Daniel, "Specification and Design of Input Devices for Teleoperation," in *IEEE International Conference on Robotics and Automation*, pp. 540–545, 1990.

[25] K. H. Hunt, *Kinematic geometry of mechanisms*. Clarendon Press Oxford, 1978.

[26] E. Fichter and E. McDowell, "A novel design for a robot arm," *Advances in computer technology*, 1980.

[27] J.-P. Merlet, *Parallel Robots*. Springer Science & Business Media, 2006.

[28] G. Schaefers, "Testing mr safety and compatibility," *IEEE Engineering in medicine and biology magazine*, vol. 27, no. 3, pp. 23–27, 2008.

[29] C. Zhao, *Ultrasonic Motors*. Springer, 2011.

[30] Y. Liu, W. Chen, J. Liu, and X. Yang, "A high-power linear ultrasonic motor using bending vibration transducer," *IEEE Transactions on Industrial Electronics*, vol. 60, no. 11, pp. 5160–5166, 2013.

[31] X. Zhou, W. Chen, and J. Liu, "Novel 2-DOF Planar Ultrasonic Motor with Characteristic of Variable Mode Excitation," *IEEE Transactions on Industrial Electronics*, vol. 63, no. 11, pp. 6941–6948, 2016.

[32] F. Sergi, V. Chawda, and M. K. OMalley, "Interaction control of a non-backdriveable MR-compatible actuator through series elasticity," in *ASME 2013 Dynamic Systems and Control Conference*, American Society of Mechanical Engineers, 2013.

[33] M. A. Tavallaei, P. M. Johnson, J. Liu, and M. Drangova, "Design and evaluation of an MRI-compatible linear motion stage," *Medical physics*, vol. 43, no. 1, pp. 62–71, 2016.

[34] M. Tavallaei, S. F. Atashzar, and M. Drangova, "Robust Motion Control of Ultrasonic Motors Under Temperature Disturbance," *IEEE Transactions on Industrial Electronics*, vol. 46, 2015.

[35] N. W. Hagood and A. J. McFarland, "Modeling of a Piezoelectric Rotary Ultrasonic Motor," *IEEE Transactions on Ultrasonics, Ferroelectrics and Frequency Control*, vol. 42, no. 2, pp. 210–224, 1995.

[36] M. T. El Hagry, A. A. Mahfouz, and H. S. Ahmed, "Experimental investigation of a mathematical model for traveling wave ultrasonic motors," in *th International Conference on Applied Mathematics and Computer Science*, 2005.

[37] T. Senjyu, S. Yokoda, and K. Uezato, "Position Control of Ultrasonic Motors Using Sliding Mode Control with Multiple Control Inputs," in *APEC '98 Thirteenth Annual Applied Power Electronics Conference and Exposition*, pp. 597–602, 1998.

[38] T. Senjyu, T. Kashiwagi, and K. Uezato, “Position Control of Ultrasonic Motors Using MRAC with Dead-Zone Compensation,” *Transactions on Industrial Electronics*, vol. 48, no. 6, 2001.

[39] T. Senjyu, M. Nakamura, N. Urasaki, H. Sekine, and T. Funabashi, “Mathematical Model of Ultrasonic Motors for Speed Control,” in *Electric Power Components and Systems*, vol. 36, pp. 637–648, 2008.

[40] J. Zhang, T. Zhan, Z. Xie, and W. Wu, “Multivariable Nonlinear Model of Ultrasonic Motor based on Hammerstein Model and Uniform Design,” in *8th World Congress on Intelligent Control and Automation*, pp. 5794–5799, 2010.

[41] H. Yoshino and K. Tanaka, “Finite-Time Stabilization of Ultrasonic Motor With Stochastic Compensator for Chattering Phenomena,” in *Industrial Electronics Society , IECON 2016 - 42nd Annual Conference of the IEEE*, 2016.

[42] C. Canudas-de Wit, “Control design for ultrasonic motors with dynamic friction interface,” in *14th World Congress of IFAC*, 1999.

[43] R. García-Rochín, M. Kühne, R. Santiesteban-Cos, G. J. Rubio-Astorga, and A. Peer, “Second-Order Model for Rotary Traveling Wave Ultrasonic Motors,” in *Humanoids*, 2015.

[44] T. Senjyu, H. Miyazato, and K. Uezato, “Quick and precise position control of an ultrasonic motor with dual mode control,” *Electrical Engineering in Japan*, vol. 116, no. 3, pp. 1333–1340, 1996.

[45] T. Senjyu, T. Yoshida, N. Urasaki, K. Uezato, T. Funabashi, H. Sekine, and S. K. Panda, “Position Control of Ultrasonic Motors using Two-control Inputs Hm Controller,” in *Power Electronics and Drive Systems*, pp. 269–274, 2003.

[46] T. Senjyu, T. Yoshida, K. Uezato, and T. Funabashi, “Ultrasonic Motors Using Adaptive Backstepping Control and Dead-Zone Compensation with Fuzzy Inference,” in *IEEE International Conference on Industrial Technology*, pp. 560–565, 2002.

[47] T. Senjyu, S. Yokoda, Y. Gushiken, and K. Uezato, “Position control of ultrasonic motors with adaptive dead-zone compensation,” in *IEEE Industry Applications Conference*, pp. 506–512, 1998.

[48] T. Senjyu, H. Miyazato, S. Yokoda, and K. Uezato, “Position Control of Ultrasonic Motors Using Neural Network,” in *IEEE International Symposium on Industrial Electronics*, pp. 368–373, 1996.

[49] C. Bartzis, K. Zarkadis, K. Zaoskoufis, A. Tzes, and E. C. Tatakis, “Experimental studies on a fuzzy-logic control scheme for an ultrasonic motor,” in *2016 IEEE Conference on Control Applications (CCA)*, 2016.

[50] C. Canudas-de Wit, H. Olsson, K. J. Aström, and P. Lischinsky, “A New Model for Control of Systems with Friction,” *IEEE Transactions on Automatic Control*, vol. 40, no. 3, pp. 419–425, 1995.

[51] Y. V. Orlov, *Discontinuous Systems*. Springer, 2009.

[52] A. F. Filippov, *Differential equations with discontinuous right-hand side*. Kluwer Academic Publishers Group, 1988.

[53] F. Giraud, B. Lemaire-Semail, J. Aragones, J. P. Robineau, and J. T. Audren, "Precise position control of a traveling-wave ultrasonic motor," *IEEE Transactions on Industry Applications*, vol. 43, no. 4, pp. 934–941, 2007.

[54] F. Giraud, P. Sandulescu, M. Amberg, B. Lemaire-Semail, and F. Ionescu, "Modeling and Compensation of the Internal Friction Torque of a Travelling Wave Ultrasonic Motor," *IEEE Transaction on Haptics*, 2011.

[55] V. Utkin, *Sliding Modes in Control Optimization*. Springer, 1992.

[56] V. Utkin, J. Guldner, and J. Shi, *Sliding Mode Control in Electro-Mechanical Systems*. Taylor & Francis Group, LLC, 2009.

[57] R. I. Leine and H. Nijmeijer, *Dynamics and Bifurcations of Non-Smooth Mechanical Systems*, vol. 18. 2004.

[58] A. Ferreira and P. Minotti, "High-performance load-adaptive speed control for ultrasonic motors," *Control Engineering Practice*, vol. 6, 1998.

[59] F. Sergi, A. C. Erwin, and M. K. OMalley, "Interaction Control Capabilities of an MR-Compatible Compliant Actuator for Wrist Sensorimotor Protocols During fMRI," *IEEE/ASME Transactions on Mechatronics*, vol. PP, no. 99, 2015.

[60] F. Pierrot, A. Fournier, and P. Dauchez, "Towards a fully-parallel 6 dof robot for high-speed applications.," in *IEEE International Conference on Robotics and Automation*, 1991.

[61] Y. Yang, Y. Zhang, Y. Zhang, and Y. Cao, "Design and Analysis of a New Six-DoF Parallel Haptic Device with Singularity-Free Task Workspace," in *Proceedings of the ASME 2008 International Design Engineering Technical Conference & Computers and Information in Engineering Conference*, (Brooklyn, New York), pp. 1–9, 2008.

[62] M. A. Ergin and A. Peer, "Development of a new 6 DOF parallel haptic interface for the rendering of elements and interior equipment in a car," in *2013 IEEE Ro-Man*, pp. 238–244, IEEE, 2013.

[63] J. H. Lee, H. W. Kim, B.-j. Yi, and I. H. Suh, "Singularity-free algorithms and design scheme for a new 6-DOF parallel haptic device," in *Proceedings 2002 IEEE International Conference on Robotics and Automation*, IEEE, 2002.

[64] E. de Vlugt, A. C. Schouten, F. C. T. van der Helm, P. C. Teerhuis, and G. G. Brouwn, "A force-controlled planar haptic device for movement control analysis of the human arm," *Journal of neuroscience methods*, vol. 129, no. 2, pp. 151–168, 2003.

[65] L. Stocco, S. E. Salcudean, and F. Sassani, "Fast Constrained Global Minimax Optimization of Robot Parameters," *Robotica*, 1998.

[66] V. M. Hung and U. J. Na, “Optimal Design of a New 6-DOF Haptic Device,” in *11th International Conference on Control, Automation and Systems*, pp. 849–852, 2011.

[67] A. Ahmad, K. Andersson, and U. Sellgren, “An Optimization Approach Toward a Robust Design of Six Degrees of Freedom Haptic Devices,” *Journal of Mechanical Design*, 2015.

[68] V. Hayward and O. R. Astley, “Performance Measures for Haptic Interfaces,” *International Symposium In Robotics Research*, pp. 195–207, 1996.

[69] P. Bande, M. Seibt, E. Uhlmann, S. K. Saha, and P. V. M. Rao, “Kinematics analyses of Dodekapod,” *Mechanism and Machine Theory*, vol. 40, no. 6, pp. 740–756, 2005.

[70] P. A. Voglewede and I. Ebert-Uphoff, “Measuring Closeness to Singularities for Parallel Manipulators,” in *Proceedings of the 2004 IEEE International Conderence on Robotics & Automation*, pp. 4539–4544, 2004.

[71] M.-W. Ueberle, *Design , Control , and Evaluation of a Family of Kinesthetic Haptic Interfaces*. PhD thesis, Technische Universität München, 2006.

[72] J.-P. Merlet, “Singular Configurations of Parallel Manipulators and Grassmann Geometry,” *The International Journal of Robotics Research*, vol. 8, no. 5, pp. 45–56, 1989.

[73] M. Gouttefarde, D. Daney, and J. P. Merlet, “Interval-analysis-based determination of the wrench-feasible workspace of parallel cable-driven robots,” *IEEE Transactions on Robotics*, 2011.

[74] J. M. Porta, L. Ros, O. Bohigas, M. Manubens, C. Rosales, and L. Jaillet, “The CUIK Suite,” *IEEE Robotics & Automation Magazine*, no. September, pp. 105–114, 2014.

[75] L. J. Stocco, S. E. Salcudean, and F. Sassani, “On the Use of Scaling Matrices for Task-Specific Robot Design,” *IEEE Transactions on Robotics and Automation*, 1999.

[76] S. Krut, O. Comany, and F. Pierrot, “Force Performance Indexes for Parallel Mechanisms with Actuation Redundancy,” 2006.

[77] P. Cardou, S. Bouchard, and C. Gosselin, “Kinematic-sensitivity indices for dimensionally nonhomogeneous jacobian matrices,” *IEEE Transactions on Robotics*, vol. 26, no. 1, pp. 166–173, 2010.

[78] K. H. Hunt, “Structural Kinematics of In-Parallel-Actuated Robot-Arms,” *Journal of Mechanical Design*, vol. 105, pp. 705–712, 1983.

[79] A. Wolf and M. Shoham, “Investigation of Parallel Manipulators Using Linear Complex Approximation,” *Journal of Mechanical Design*, vol. 125, no. 3, p. 564, 2003.

[80] T. Hufnagel and A. Müller, “A Projection Method for the Elimination of Contradicting Decentralized Control Forces in Redundantly Actuated PKM,” *IEEE Transactions on Robotics*, vol. 28, no. 3, pp. 723–728, 2012.

[81] A. Mueller, “Problems in the Control of Redundantly Actuated Parallel Manipulators caused by Geometric Imperfections,” *Meccanica*, no. 46, pp. 41–49, 2011.

[82] W. Shang, S. Cong, and Y. Ge, “Coordination Motion Control in the Task Space for Parallel Manipulators With Actuation Redundancy,” *IEEE Transactions on Automation Science and Engineering*, vol. 10, no. 3, 2013.

[83] “Phantom premium.” `http://www.geomagic.com/en/products/phantom-premium-6dof/overview/`.

[84] “Maglev 200.” `http://butterflyhaptics.com/products/productspec.pdf`.

[85] “Virtuose 6D Desktop.” `https://www.haption.com/site/pdf/Datasheet_Virtuose_6DDesktop.pdf`.

[86] “Delta.6.” `http://www.forcedimension.com/downloads/specs/specsheet-delta.6.pdf`.

[87] “Sigma.7.” `http://www.forcedimension.com/downloads/specs/specsheet-sigma.7.pdf`.

[88] Waldemar Karwowski, *International Encyclopedia of Ergonomics and Human Factors*. FL, USA: CRC Press, Inc. Boca Raton,, 2006.

[89] G. Westling and R. S. Johansson, “Factors influencing the force control during precision grip.,” *Experimental brain research. Experimentelle Hirnforschung. Experimentation cerebrale*, vol. 53, pp. 277–284, 1984.

[90] G. Cadoret and a. M. Smith, “Friction, not texture, dictates grip forces used during object manipulation.,” *Journal of neurophysiology*, vol. 75, no. 5, pp. 1963–1969, 1996.

[91] S. Tomlinson, R. Lewis, and M. Carre, “Review of the frictional properties of finger-object contact when gripping,” *Proceedings of the Institution of Mechanical Engineers, Part J: Journal of Engineering Tribology*, vol. 221, pp. 841–850, 2007.

[92] Z. Najdovski, S. Nahavandi, S. Member, and T. Fukuda, “Design , Development , and Evaluation of a Pinch-Grasp Haptic Interface,” *IEEE Transactions on Mechatronics*, 2014.

[93] F. Conti, F. Barbagli, R. Balaniuk, M. Halg, C. Lu, D. Morris, L. Sentis, E. Vileshin, J. Warren, O. Khatib, and K. Salisbury, “The CHAI libraries,” *EuroHaptics 2003*, pp. 496–500, 2003.

[94] S. Menon, M. Yu, K. Kay, and O. Khatib, “Haptic fMRI: accurately estimating neural responses in motor, pre-motor, and somatosensory cortex during complex motor tasks,” *International Conference of the IEEE Engineering in Medicine and Biology Society*, pp. 2040–2045, 2014.

[95] H. H. Ehrsson, A. Fagergren, H. Forssberg, H. Henrik, E. Fagergren, H. Forssberg, A. Fagergren, H. Forssberg, and H. Henrik, “Differential fronto-parietal activation depending on force used in a precision grip task: an fMRI study.,” *Journal of neurophysiology*, vol. 85, no. 6, pp. 2613–23, 2001.

[96] J. P. Kuhtz-Buschbeck, H. H. Ehrsson, and H. Forssberg, “Human brain activity in the control of fine static precision grip forces: An fMRI study,” *European Journal of Neuroscience*, vol. 14, no. 2, pp. 382–390, 2001.

[97] M. Kawato, T. Kuroda, H. Imamizu, E. Nakano, S. Miyauchi, and T. Yoshioka, “Internal forward models in the cerebellum: fMRI study on grip force and load force coupling,” *Progress in Brain Research*, vol. 142, pp. 171–188, 2003.

[98] P. A. Chouinard, M. E. Large, E. C. Chang, and M. A. Goodale, “Dissociable neural mechanisms for determining the perceived heaviness of objects and the predicted weight of objects during lifting: An fMRI investigation of the size-weight illusion,” *NeuroImage*, 2009.